INTERACTIONS BETWEEN CLIMATE VARIABILITY AND AIR POLLUTION —A STUDY OF SEVERE HAZE AND LARGE WILDFIRES

A Dissertation
Presented to
The Academic Faculty

by

Yufei Zou

In Partial Fulfillment
of the Requirements for the Degree
DOCTOR OF PHILOSOPHY in the
SCHOOL OF EARTH AND ATMOSPHERIC SCIENCES

Georgia Institute of Technology
DECEMBER 2017

INTERACTIONS BETWEEN CLIMATE VARIABILITY AND AIR POLLUTION —A STUDY OF SEVERE HAZE AND LARGE WILDFIRES

Approved by:

Dr. Yuhang Wang, Advisor
School of Earth and Atmospheric Sciences
Georgia Institute of Technology

Dr. Rodney Weber
School of Earth and Atmospheric Sciences
Georgia Institute of Technology

Dr. Armistead G. Russell
School of Civil and Environmental Engineering
Georgia Institute of Technology

Dr. Yi Deng
School of Earth and Atmospheric Sciences
Georgia Institute of Technology

Dr. Athanasios Nenes
School of Earth and Atmospheric Sciences & Chemical and Biomolecular Engineering
Georgia Institute of Technology

Dr. Robert Black
School of Earth and Atmospheric Sciences
Georgia Institute of Technology

Date Approved: September 25, 2017

To my parents and beloved family,

and all those who supported me in my PhD study

ACKNOWLEDGEMENTS

Firstly, I would like to thank my advisor, Dr. Yuhang Wang, for his in-depth guidance and long-last support for my PhD study. I still remember the excitement when I first received the admission from Dr. Wang to this program at Georgia Tech. Dr. Wang provided me a great opportunity to get close to the cutting edge of atmospheric research. I benefitted from his insights and passions and enjoyed my graduation study at Georgia Tech with unforgettable memories and experiences. I am also grateful to my dissertation committee members, Dr. Armistead Russell, Dr. Athanasios Nenes, Dr. Rodney Weber, Dr. Yi Deng, and Dr. Robert Black for their careful review and constructive suggestions to consummate this dissertation. Without their help and mentoring, this work would not be nearly as good as it could get.

Next, I would like to thank all members and alumni of Dr. Wang's group for their good company. I have gained a lot by working with Dr. Yuzhong Zhang, Dr. Ja-Ho Koo, Dr. Dasa Gu, Dr. Yongjia Song, Dr. Tao Zeng, Dr. Zhen Liu, Tom Loadholt, Charles Smeltzer, Ziming Ke, Ruixiong Zhang, Hang Qu, Jianfeng Li, Ye Cheng, Aoxing Zhang, and Qiyang Yan. I am thankful for all my coauthors and research collaborators, especially Dr. Zuowei Xie, Dr. Yongtao Hu, Dr. Hanqin Tian, Dr. Yongqiang Liu, Dr. Xiaohong Liu, Dr. Yun Qian, Dr. Jia Yang, and Dr. Huizhong Shen, for inspiring discussions with me.

Lastly, I would like to express my deepest gratitude to my parents and beloved family members, Xinxin and Dobby, for their consistent support as the backbone of my graduate study and my entire life. I cannot sustain the pressure in the past years and carry on till now without their supportive encouragement and sacrifices.

TABLE OF CONTENTS

LIST OF TABLES

LIST OF FIGURES

LIST OF SYMBOLS AND ABBREVIATIONS

AC	Anthropogenic Constraint
AERONET	the Aerosol Robotic Network
ALI	Aleutian Low Index
AO	Arctic Oscillation
AOD	Aerosol Optical Depth
API	Air Pollution Index
AR	total autotrophic respiration
AS	Anthropogenic Scaling factor
ATGI	Air Temperature Gradient Index
BA	Burned Area
BLND	Bare land
BTREE	Broadleaf tree
CAM5	the Community Atmosphere Model version 5
CDF	Cumulative Density Function
CESM	the Community Earth System Model
CFI	Cryosphere Forcing Index
CGD	the Climate and Global Dynamics Laboratory
CI	Confidence Interval
CLM4.5	the Community Land Model version 4.5
CMIP5	the fifth phase of the Coupled Model Inter-comparison Project
CRU	the Climatic Research Unit
CTRL	the control experiment

CWDC	coarse woody debris carbon
DGVM	Dynamic Global Vegetation Model
E	the Extended Eliassen-Palm vector
EA	the East Atlantic pattern
EAWM	East Asia Winter Monsoon
ECMWF	the European Centre for Medium-Range Weather Forecasts
ECP	the Eastern China Plains
ENSO	El Niño/Southern Oscillation
ER	total ecosystem respiration
EURA	Eurasia excluding Middle East and South Asia
FireMIP	the Fire Model Inter-comparison Project
FRP	Fire Radiative Power
FWET	Fraction of wet canopy
GDP	Gross Domestic Production
GEV	the Generalized Extreme Value theory
GFED	the Global Fire Emissions Database
GHG	Greenhouse Gas
GPP	Gross Primary Production
GSOD	the Global Surface Summary of Day database
HadISST	the Hadley Centre Sea Ice and Sea Surface Temperature data set
HR	total heterotrophic respiration
ILAMB	the International Land Model Benchmarking project
LAI	Leaf Area Index
LULCC	Land Use and Land Cover Change
MAM3	the 3-mode modal aerosol scheme

MCA	Maximum Covariance Analysis
MEI	Multivariate ENSO Index
MENA	Middle East and North Africa
MODIS	the Moderate Resolution Imaging Spectroradiometer
MP	the fire induced mortality potential pool
MR	the fire induced mortality rates
NC	Natural Constraint
NCAR	the National Centre for Atmospheric Research
NCDC	the National Climatic Data Center
NCEP	the National Centers for Environmental Prediction
NEE	Net Ecosystem Exchange
NEP	Net Ecosystem Production
NHAF	Northern Hemisphere Africa
NOAA	the National Oceanic and Atmospheric Administration
NPP	Net Primary Production
NS	Natural Scaling factor
NTHA	North America
NTREE	Needleleaf tree
OCEA	Oceania
PREC10	10-day running mean of total precipitation
PCA	Principal Component Analysis
PCR	Principal Component Regression
PFT	Plant Functional Type
PM	Particulate Matter
PPI	Pollution Potential Index

PV	Potential Vorticity
RCP	Representative Concentration Pathway
RESFire	the REgion-Specific ecosystem feedback Fire model
RMSE	Root Mean Square Error
SAT	Surface Air Temperature
SCE	Snow Cover Extent
SENS	the sensitivity experiment
SHAF	Southern Hemisphere Africa
SHI	Siberian High Index
SIC	Sea Ice Concentration
SSEA	South and Southeast Asia
SST	Sea Surface Temperature
STHA	South America
SW	Surface soil wetness factor
SWE	Snow Water Equivalent
T10	10-day running mean of 2-m temperature
TBOT	Surface air temperature
TEM	Terrestrial Ecosystem Model
TOTCOLC	total column carbon
TOTLITC	total litter carbon
TOTVEGC	total vegetation carbon
ViI	Visibility Inverse
WACCM	the Whole Atmosphere Community Climate Model
WAF	Wave Activity Flux
WF	Soil water fraction for top 0.05m layers

WSI Wind Speed Index

SUMMARY

The drastically changing climate system plays a critical role in modulating emission and distribution conditions of air pollutants including greenhouse gases, aerosols, and tracer gases, while these air pollutants exert significant feedback to the climate system through multiple biogeophysical, biogeochemical, and hydrological pathways. These interactions occur at different spatial and temporal scales that increase the difficulty for a clear and comprehensive understanding. To shed light on complex interactions between climate variability and air pollution, I used statistical and numerical modeling approaches to investigate the interactive relationship between climate variability and air pollution in the context of severe haze pollution in China and large wildfires worldwide. I identified the key climatic and meteorological forcing factors for the spatial and temporal variations of the two typical air pollution events including severe haze in winter over eastern China and biomass burning in fire-prone regions using statistical detection and attribution methods. Then I improved and employed the state-of-the-art Community Earth System Model (CESM) to investigate the underlying mechanisms driving their variability as well as to understand interactive feedback pathways. Based on comprehensive statistical analysis, dynamic diagnosis, and numerical sensitivity simulations, I found a close connection between deteriorating winter atmosphere ventilation in China and rapidly changing boreal cryosphere in preceding months. I proposed a physical mechanism to explain the teleconnection relationship for the China's winter haze pollution problem. I also developed a region-specific fire model with climate and ecosystem feedback in CESM

and utilized this new fire model to evaluate complex climate-fire-ecosystem interactions as well as to predict decadal climate variability with fully interactive fire disturbances.

In the first part of this research, I analyzed series of extreme haze pollution events over eastern China in recent winters and found an increasing trend in regional air stagnation conditions throughout the past three decades. I examined the influence of multiple climate forcing factors and identified the key synoptic circulation patterns contributing to these unfavorable ventilation conditions. I quantified the climate impacts on regional circulation and ventilation by principal component analysis and regression methods as well as numerical sensitivity experiments using multiple climate models. It was found that unprecedented air stagnation accompanied by the weakening winter monsoon over eastern China was one of the main causes of extreme haze pollution in recent years in addition to high intensity of anthropogenic emissions over this region. Such weakening ventilation capability was attributed to winter circulation changes with disturbed winter monsoon activities. The latter was further related with boreal cryosphere changes including Arctic sea ice declining in preceding autumn and Eurasian snow expansion in early winter. Multi-decadal changes in sea surface temperature (SST) might also play important roles in modulating regional circulation. I investigated the physical processes involved in these teleconnection relationships and proposed that the external climate forcing changes such as Arctic sea ice and Eurasian snow contributed to inter-decadal to intra-seasonal variations of prominent atmosphere modes in the Northern Hemisphere, which further modulated winter circulation as well as air pollution ventilation over eastern China and resulted in severe haze pollution due to increasing occurrence probabilities of extreme air stagnation. Such increasing trends were also considerable in future projections following

Representative Concentration Pathway 8.5 (RCP8.5) based on 11 climate model ensembles from the fifth phase of the Coupled Model Inter-comparison Project (CMIP5), in which extreme air stagnation probability in winter over eastern China increased by 100% by the end of the 21st century due to global warming and declining Arctic sea ice.

In the second part, I looked into global wildfires, which are another example of climate-air pollution interactive systems with profound climate, ecosystem, and socioeconomic impacts, by using the state-of-the-art Community Earth System Model (CESM). I developed a REgion-Specific ecosystem feedback Fire model (RESFire) in CESM that provides modelling capability to understand the complex climate-fire-ecosystem interactions. Compared to the default fire model in CESM, the new RESFire model prevailed by better simulation performance of fire dynamics due to process-based heterogeneous natural and anthropogenic constraints, online plume rise parameterization, and fire weather modelling bias corrections. Driven by either offline observation-reanalysis combined meteorological inputs or online Community Atmosphere Model version 5 (CAM5) simulation data, the RESFire model properly reproduced burned area of the latest version of Global Fire Emissions Database (GFED4.1s) and the observed distributions of fire radiative power by the Moderate Resolution Imaging Spectroradiometer (MODIS). Evaluation results based on the International Land Model Benchmarking (ILAMBv2) package showed significant improvements in fire simulation performance relative to previous fire models. The overall modelling score of burned area increased from 0.50 of the default Community Land Model version 4.5 fire model (CLM4.5-fire) to 0.61 of offline RESFire (RESFire driven by observation-reanalysis atmosphere data) and 0.60 of online RESFire (RESFire driven by the CAM5 atmosphere model), respectively, with improved

spatial and temporal variability. The model also includes an integrated fire impact module to estimate direct fire emissions as well as disturbances on ecosystems and surface radiation budget with land cover changes. The RESFire model enables future climate projections with interactive climate-fire-ecosystem processes using CESM. I conducted decadal predictions following Representative Concentration Pathway 4.5 (RCP4.5) with both active and inactive fire disturbances in the model and found roughly 19% and 100% increases in global burned area and fire carbon emissions, respectively, from the present day to the middle of the 21st century. By comparing different prediction experiments, I isolated multiple climate-fire-ecosystem interactions in terms of climate feedback associated with fire emissions and ecosystem feedback associated with fire induced land use and land cover change (LULCC). It is concluded that fire aerosol emissions generally show positive feedback to fire activities through perturbations on precipitation and hydrological cycles while fire induced LULCC shows negative feedback through perturbations on fuel load supply. These results demonstrated the latest progress of global fire modelling development and applications in climate model studies and improved our understanding of the role of fires in the climate system.

To sum up, I investigated the two-way interactions between climate change and typical air pollution cases such as extreme haze and large wildfires and revealed the underlying mechanisms for observational variations as well as future predictions. These studies represent the advanced efforts to answer the intriguing question of the interactive relationship between climate variability and air pollution, and the knowledge obtained through these efforts would benefit both the regulation practice of regional air pollution control and the design of mitigation strategies for future climate change risks.

CHAPTER 1. INTRODUCTION

1.1 Statement of the Problem

Air pollution and climate change are closely related with each other. Figure 1 illustrates the interactions between climate change and air pollution through simplified pathways [1]. On the one hand, climate change can affect air pollution severity by changing meteorological conditions for primary emission sources, secondary chemical formation, and physical accumulation and deposition of air pollutants and their precursors. On the other hand, several air pollutants can modulate regional to global climate by perturbing radiation budget, hydrological cycles, and ecosystem functionality. These interactions are complex and not well understood given numerous synergistic and competing feedback processes in and between each side. A practical way to understand their interactions is to concentrate on a specific air pollution category and go through all relevant characteristics and interactive processes. These efforts would provide mutual benefits for both air pollution and climate change research communities with a more well-rounded perspective. They also lay the foundation for more effective air pollution and climate change mitigation strategies with higher socioeconomic benefit-cost ratios. Therefore, I specifically looked into two types of air pollution cases—severe haze pollution in China and large wildfires worldwide—to improve the knowledge of their interactive relations with climate change in this work.

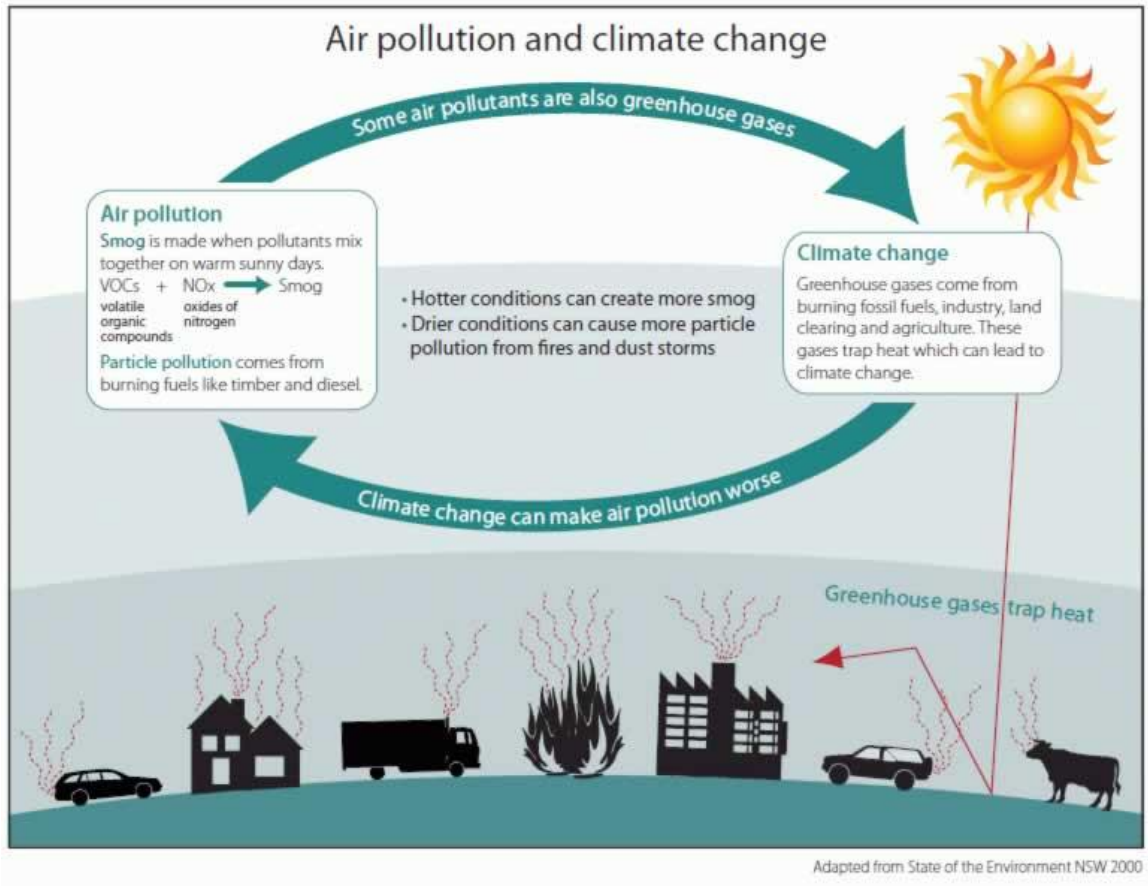

Figure 1 – A schematic diagram describing the interactive relations between air pollution and climate change. Adopted from State of the Environment NSW 2000 [1].

1.1.1 The Impact of Climate Change on Winter Haze Pollution in China

A consequence of rapid economic growth in China is a deterioration of air quality. Series of heavy haze pollution events have occurred over eastern China in recent winters, which drew broad domestic and international attention given their profound public health [2, 3], socioeconomic [4], and climatic impacts [5]. Though the historical air quality observation data are very limited in this region due to insufficient monitoring capability and network before 2014, the current available air pollutant measurements in Beijing and surrounding cities (Figure 2) still shed some light on the temporal evolution of regional air

quality and its relationship with fossil fuel consumption. It is interesting to note that the time series of air pollutants and coal consumption as one of their primary sources are not always coupled with consistent variations throughout the period. The PM concentrations in Beijing also show divergent changes in winter seasonal mean and annual mean values in the last decade, with a decreasing rate of 3.36μg/m^3 in the annual mean $PM_{2.5}$ but an increasing rate of 1.3μg/m^3 in the winter seasonal mean $PM_{2.5}$ of Beijing over the last 10 years [6]. These divergences suggest another invisible hand that is modulating interdecadal to intra-seasonal variations of regional air quality besides natural and anthropogenic emissions. Previous studies have indicated strong dependence of air quality on weather and climate change, though the effect of climate change on the particulate matter (PM) pollution is more complicated and uncertain than other species [7]. Such complexity is partly derived from diversified interactions between climate variability and PM pollutants. Both long-term climate and short-term meteorological conditions could influence primary aerosol emissions like dust and wildfires, secondary formation rates with perturbed atmospheric chemistry, and aerosol sink through transport, deposition, and ventilation. In return, different aerosol species could modulate regional to global climate by changing direct and indirect radiative forcing and consequent meteorological and hydrological responses. It has been found that China contributes 10%±4% of the current global radiative forcing with 12%±2% relative contribution to the positive (warming) component by well-mixed greenhouse gases and black carbon aerosols and 15%±6% relative contribution to the negative (cooling) component by sulfate and nitrate aerosols [5]. The severe haze pollution induced by high PM concentrations in China is also linked to 959,338 premature

deaths in China and more than 64,800 premature deaths in other regions due to transboundary pollution transport in 2007 [8].

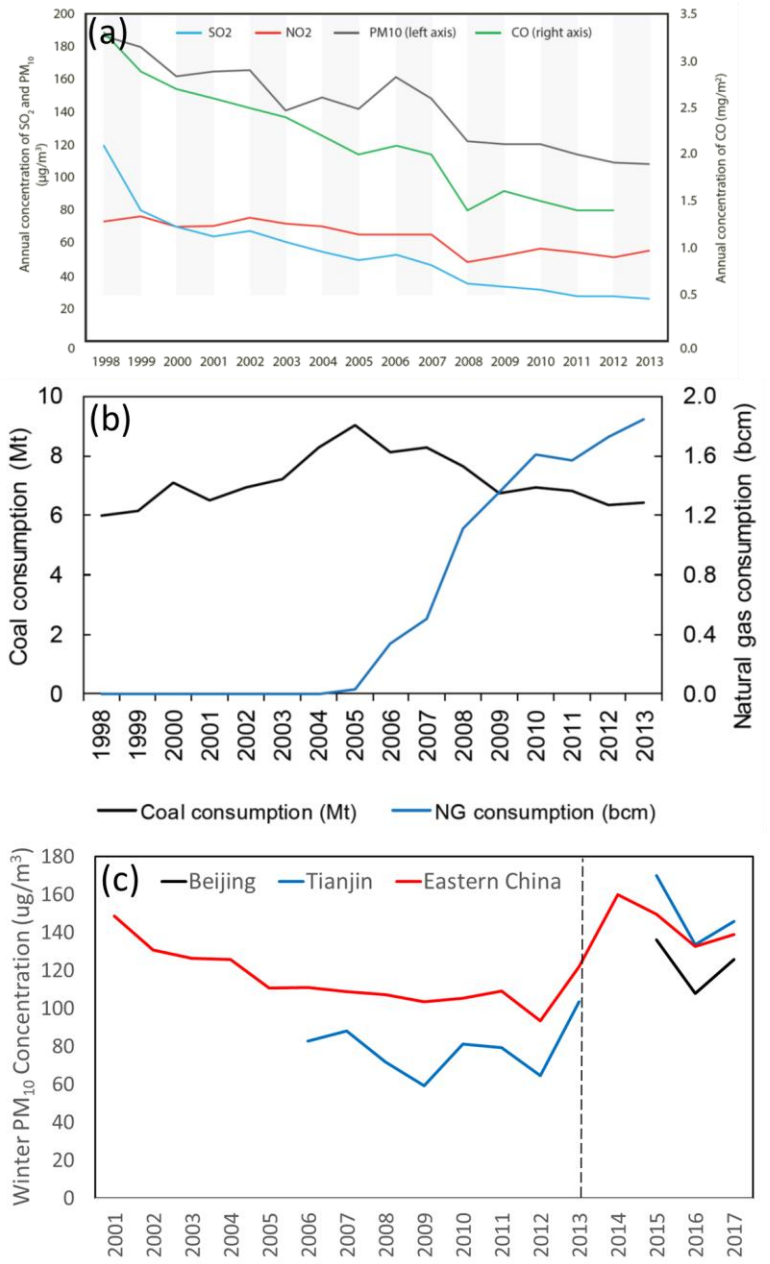

Figure 2 – Time series of air pollutant concentrations and fossil fuel consumption in Beijing. (a) annual concentrations of air pollutants in Beijing from 1998 to 2013. (b) annual fossil fuel consumption in Beijing from 1998 to 2013. (c) winter (December-

January-February, DJF) seasonal mean concentrations of PM_{10} in Beijing from 2001 to 2017. (a) and (b) are adopted from the UNEP 2016 report [9]. (c) are produced based on daily air pollution index (before 2013) and air quality monitoring data (2014-2017) for 11 eastern China cities collected from the Chinese Ministry of Environmental Protection.

To unveil the mist of severe air pollution problems in China for advanced air quality management, numerous studies investigated the haze formation mechanism from various perspectives such as primary emissions, secondary formation, and regional circulation changes. Though most air pollution studies in China emphasized large contributions from heavy regional anthropogenic emissions [10-13] and rapid chemical formation [10, 14, 15], it is reported that climate change might also play an important role in providing conducive meteorological conditions with deteriorated regional ventilation for severe air pollution [16-20]. Since emission changes in a specific region are relatively slow with stable intra-seasonal fluctuations and long-term inter-decadal variations, stagnant meteorological conditions favoring high aerosol formation and accumulation appear to be a major factor affecting both the long-term trend and the short-term fluctuation of haze pollution episodes [7]. Recent studies indicated a decadal weakening trend of the East Asian Winter Monsoon (EAWM) [21] and consequently decreasing wind speed [22] and increasing aerosol concentrations [16], but the underlying mechanism of internal variability and external climate factors modulating air stagnation related circulation changes are still not well understood. Other studies examined the future projections of air stagnation conditions using the CMIP5 high emission scenario (RCP8.5) data [23] but ended up with contradictory conclusions over the eastern China region. In 2014, Horton et al. [24] firstly

used an air stagnation index based on an ensemble of bias-corrected climate model simulations to quantify the response of stagnation occurrence and persistence to global warming. They found increased air stagnation occurrence that covered 55% of the current global population with major increasing areas over the tropics and subtropics but nonappreciable or even decreasing changes in extreme stagnation event duration and exposure in China based on the CMIP5 RCP8.5 projections [24]. To the contrary, Cai et al. [19] also used the RCP8.5 ensemble projections and suggested a 50% increase in the frequency and an 80% increase in the persistence of extreme stagnation events in Beijing. Their results were estimated from three air quality related meteorological indices including vertical temperature difference between the lower (850hPa) and upper (250hPa) troposphere, near surface (850hPa) southerly anomalies around Beijing, and a latitudinal difference in 500hPa zonal winds between north of Beijing and south of Beijing. Though the projected changes in the synthesis haze weather index were quite prominent, the increases in the haze weather index were mainly driven by increasing temperature gradient due to strong warming in the RCP8.5 scenario rather than near surface anomalous southerly winds. The latter wind factor that directly affects pollution transport and ventilation showed nonappreciable changes. Given drastic changes of global and regional climate (especially strong warming over the high latitude regions as so called Arctic amplification [25, 26]) and its pervasive influence on middle latitude circulation and weather extremes [27], it is imperative to identify the specific driving force of conducive circulation changes for severe air pollution and to understand detailed physical mechanisms of these teleconnection relationships for a better interpretation of future predictions.

In the first part of this study, I specifically investigated the China's severe haze pollution problem in winter in terms of the following three aspects:

1.1.1.1 The Long-term Variations of Regional Air Stagnation in China

I first examined the long-term variations of air stagnation conditions in winter over eastern China to tackle the haze pollution problem from the meteorological perspective. The scientific question I'd like to answer is how the regional ventilation is changing and contributing to extreme haze pollution in the past few years.

1.1.1.2 The Key Climate Driving Factors

After an examination of temporal variations of regional ventilation, I further investigated its covariant relations with multiple internal and external climate forcing factors including Arctic Oscillation (AO), El Niño/Southern Oscillation (ENSO), Arctic sea ice concentration (SIC), and Eurasian snow cover extent (SCE), etc., in order to identify the key forcing factors driving these changes.

1.1.1.3 A Dynamic Mechanism for the Teleconnection Relation

At last, I conducted comprehensive statistical analysis and dynamic diagnosis based on observational and reanalysis data as well as numerical sensitivity experiment results to understand how the remote climate changes affect regional air ventilation in eastern China during winter. I proposed a physical mechanism to explain the observed and simulated relations between climate forcing and regional responses in this section.

1.1.2 Interactive Relations of Climate Change and Wildfires

In the second part, I focused on another example of interactive systems involving climate change and air pollution—wildfires. Wildfires are widespread phenomena around the world with a long history of interactions with climate, ecosystems, and human society [28]. Global fire activities are strongly influenced by four key factors: fuel availability, fire weather, ignition agents and human activities [29], and fire exerts profound feedbacks to earth systems through direct emissions of mass and energy fluxes as well as disturbances on biogeochemical and hydrological cycles [28]. These interactions occur at multiple spatial and temporal scales that increase the difficulty to simulate fires in climate models. At short term and regional scales, local weather changes modulate burning frequency and intensity through lightning ignition, drought enhancement, and rainfall suppression, while vegetation distributions determine fuel availability and combustibility. In a recent study, *Veraverbeke et al.* [30] identified lightning as a major drive of large fires in North American boreal forest and found increasing trends of lightning ignitions in the past four decades and future projections. In Africa, opposite burning trends over southern and northern Africa were attributed to precipitation changes driven by the transition from El Niño to La Niña over the study period [31]. Such meteorological and hydrological influence on fires was also found in other fire-prone regions including Southeast Asia [32] and South America [33]. Meanwhile, fire concurrently gives feedback to both weather and ecosystems by releasing large amounts of gaseous, particulate, and energy emissions, perturbing atmospheric chemical and thermodynamic processes and radiative forcing, and reshaping vegetation structures, composition, and distributions [34, 35]. For instance, fire aerosols have been found to have significant impacts on clouds and precipitation in a nonlinear manner [36]. Fires also reshape local ecosystems by vegetation mortality and restoration [37, 38] and further disturb regional to global carbon balance [39]. In fire seasons, large wildfires often induce severe air pollution and pose a high risk to public health and human society in many regions [40-42].

At longer term and larger spatial scales, these fire-climate interactions are manifested as shifts of fire regimes in response to changes in the climate system and ecosystems as well as consequent fire feedback changes in biogeochemical cycles, land cover, and hydrological cycles [35]. Paleoclimate records suggested clear links between fire activities and abrupt climate change in North America during the last glacial-interglacial transition period [43]. Another fire history study suggested driving forces of the global fire regime shifted from precipitation-driven during the preindustrial period to anthropogenic-driven after the Industrial Revolution, and then to a temperature-driven global fire regime in future projections [44]. Several observational and modeling studies also showed the occurrence of shifting fire regimes in many regions such as increasing large wildfires over the contiguous U.S. due to the changing climate in the past centuries [45, 46]. Besides climatic driving forces, fire is also affected by human activities in terms of fire ignition and suppression [47, 48]. The declining trend of global burned area in the last century was attributed to human activities such as agricultural expansion and intensification, especially in tropical savanna regions [49, 50]. In return, fire not only contributes directly to global warming through large amount of greenhouse gas and carbonaceous aerosol emissions but also disturbs radiative forcing by changing surface albedo with aerosol deposition and postfire regeneration. Currently several global fire emission datasets have been developed using different methods based on satellite retrievals [51-55]. Though the differences among these emission estimations are large due to uncertainties in emission factors and the lack of satellite sensitivity to small fires [53], biomass burning is still considered as one of the largest source sectors contributing to global warming over both short (20-year) and long (100-year) time scales [56]. It is also reported that the net effect of all agents would reverse with increasing radiative forcing in the burring year but decreasing radiative forcing over a long-term (80-year) fire cycle due to multidecadal increases in surface albedo [57].

To understand these complex climate-fire-ecosystem interactions and better evaluate fire impacts on human society, multiple fire models have been developed in the past few decades. The modeling complexity increases from simple statistical models with empirical algorithms to advanced process-based parameterizations coupled with terrestrial ecosystem models (TEMs) and dynamic global vegetation models (DGVMs). Statistical models are developed based on empirical relationship between contemporary climate and fuel conditions and fire characteristics to investigate the climatic driving forces of fires [33] and to examine future fire projections [58]. Process-based models are usually implemented in TEMs and DGVMs to explicitly simulate fire related processes including ignition, spread, and impacts with complex interactions between fire and ecosystems. Detailed global fire modeling history and development status were summarized in *Hantson et al.* [59]. In the Fire Model Intercomparison Project (FireMIP) initialized in 2014, multiple process-based fire models were reviewed in the context of fire occurrence, fire spread, and fire impact parameterizations [59]. One problem with the current generation of fire models found in that study is the ill-represented fire disturbances on ecosystem dynamics and land-use changes [60]. The LPX-Mv1 model [61], which simulates resprouting after fires, is the only fire model in the FireMIP study with some explicit fire-triggered ecosystem regeneration modeling capability. While fire ignition and spread are relatively better represented, the fire models have limited modeling capacity to simulate diversified fire regime characteristics at regional scales [59] . Such limitations are due in part to using homogenous fire parameterizations at coarse spatial and temporal scales that do not account for the regional distinctions of fire behavior and impacts [62]. Moreover, most fire models mainly consider one-way perturbations from weather to fire with incomplete feedback mechanisms from fire to weather and climate systems, while fire assessment studies usually use prescribed fire emissions without the consideration of fire weather interactions [63]. The two-way interactions between climate and fire are indispensable in fire related research and merit more attention in advancing fire model

development. Therefore, I came up with the following three questions and conducted series of analytical and numerical studies to answer them sequentially in this part.

1.1.2.1 The Key Meteorological, Ecological, and Demographic Variables Driving Fire Activities

The first problem I need to resolve is to identify the key driving factors that determine fire intensity and severity in each fire-prone region and biome. By screening out the critical natural and anthropogenic variables, I can implement these region-specific constraint relations into a new fire model to improve fire simulation performance.

1.1.2.2 The Interactive Climate-Fire-Ecosystem Feedback Pathways

The second question I need to consider is how do different components in the system interact with each other and how to simulate these interactive feedback processes in the new fire model. Specifically, I highlighted the underrepresented fire feedback pathways in current fire models and incorporated them into the new fire model to improve fire modeling capability.

1.1.2.3 Decadal Climate Variability with Fully Interactive Fire Disturbances

The last question I am going to answer is how does the whole system is likely to change with fully interactive fire disturbances. With the help of the newly developed fire model, I am capable to design and conduct multiple sensitivity experiments to predict future changes of the climate system and fire activities with quantitative feedback contributions.

1.2 The Research Framework

As introduced in the previous section, the entire research is separated into two major parts and organized accordingly following the specific research questions.

Chapter 2. “Winter Haze Pollution in China and Its Relationship with Decadal Climate Variability” analyzes the temporal variations and covariant relations of regional air stagnation and severe haze pollution in winter over eastern China plains. It is found the recent haze extremes in winter are closely related to unfavorable atmosphere ventilation conditions, which are unprecedented in the past few decades with deteriorating tendencies in extremes. These changes are linked to boreal cryosphere changes such as melting Arctic sea ice and heavy Eurasian snow in preceding months. The conducive synoptic patterns for severe air stagnation are also identified and evaluated through advanced statistical analysis.

Chapter 3. “Numerical Modeling Studies of the Impact of Boreal Cryosphere Changes on Regional Air Stagnation” evaluates the hypothetic statistical connections among climate forcing factors, synoptic circulation changes, and regional air ventilation responses with comprehensive dynamic diagnosis and numerical sensitivity simulations. A physical mechanism is proposed to explain the statistical relations in both observation and reanalysis data as well as numerical modeling results. Future projections based on multiple climate models are also examined throughout the teleconnection linkage, which proves out its robustness in both historical diagnosis and future predictions.

Chapter 4. “Development of a REgion-Specific ecosystem feedback Fire model (RESFire) in the Community Earth System Model” introduces the development of major

components including fire occurrence, fire spread, and fire impact modules in the RESFire model. The model performance is also evaluated from various perspectives such as simulations of burned area, fire emissions, and ecosystem disturbances. The new features like online bias corrections in the model are highlighted given their critical impacts on the following prediction studies.

Chapter 5. "Understanding Climate-Fire-Ecosystem Interactions using RESFire and Implications for Decadal Climate Variability" demonstrates the application potential of the new RESFire model in the climate modeling research. Series of sensitivity experiments are conducted to quantify the impact of complex interactions among each component as well as to predict future changes in the climate system and fire activities. Modeling results show significant increases in global burned area and fire emissions with enhanced climatic and ecological impacts in future.

Chapter 6. "Conclusions and Implications" summarizes the research findings of previous chapters and concludes with implications and suggestions for the future work.

CHAPTER 2. WINTER HAZE POLLUTION IN CHINA AND ITS RELATIONSHIP WITH DECADAL CLIMATE VARIABILITY

To meet the increasing needs for clean air and blue sky from the public, the Chinese government has been lifting the priority of air pollution control in its regulation with strengthened governance capability [64]. Those efforts were accelerated after an extreme haze event in January 2013, which marked as a tipping point for the public awareness of severe air pollution as well as Chinese government's environmental regulation. In that month, a record of air pollution was set with unprecedented large-scale haze lasting almost an entire month. During this so-called 'airpocalypse' period, ~70% of the seventy-four major cities exceeded the daily $PM_{2.5}$ (particulate matter with size < 2.5μm) ambient air quality standard of China (75 $\mu g \cdot m^{-3}$), with the maximum daily $PM_{2.5}$ reaching 766 $\mu g \cdot m^{-3}$ and the monthly mean concentration as high as 130 $\mu g \cdot m^{-3}$ [65]. Exposure to such high particulate matter (PM) concentrations endangered public health with increasing risks of cardiovascular and respiratory morbidity, which might have caused 690 (95% confidence interval (CI): 490~890) premature deaths, 45,350 (95% CI: 21,640~57,860) acute bronchitis, 23,720 (95% CI: 17,090~29,710) asthma cases in Beijing as well as 253.8 (95% CI: 170.2~331.2) million US$ economic losses [66].

In this study, we placed the occurrence of recent winter haze extremes in China in the context of historical ventilation conditions in the last 35 years. The East China Plains (ECP, 112° E -122° E, 30° N - 41° N, Figure 3a) are the focus of this study. The region hosts a large portion of the Chinese population and suffers from severe air pollution problems. It resembles a horseshoe–shaped basin where the ventilation of air pollutants

relies on large-scale weather systems [67]. Pollutant ventilation can be either horizontal or vertical. We first computed normalized near-surface wind speed index (WSI) for horizontal ventilation and potential air temperature gradient index (ATGI) for vertical ventilation, respectively, and then constructed a synthetic meteorological index—Pollution Potential Index (PPI)—to better quantify the synergistic effect of ventilation on regional air pollution. We then explored the relationship between PPI and regional climate variability through comprehensive statistical approaches including Maximum Covariance Analysis (MCA) [68], Principal Component Analysis (PCA) [69], and wavelet coherence analysis [70]. Using these analysis as a guide, we identified the key synoptic circulation patterns that determined the pollution ventilation capability in the ECP region and investigated how these anomalous circulation patterns were related with drastically changing climate forcing factors including declining Arctic sea ice and anomalously heave Eurasian snow.

2.1 Materials and Methods

2.1.1 Observation and Reanalysis Datasets

The air pollution data for this study consist of four sources: ground *in situ* PM_{10} monthly concentrations (2005-2015) retrieved from the daily Air Pollution Index (API) of five major cities (Zibo, Jining, Kaifeng, Pingdingshan, and Jinzhou given the longest time series in these cities) in the ECP region collected from the Chinese Ministry of Environmental Protection (http://datacenter.mep.gov.cn/report/air_daily/air_dairy.jsp?&lang=), ground *in situ* $PM_{2.5}$ concentrations in Beijing (2009-2015) collected from the Mission China air quality monitoring program of the U.S. Department of State

(http://www.stateair.net/web/post/1/1.html), the RH-corrected meteorological visibility inverse (ViI, 1981-2013) [71] at the 45 plain ground sites (altitude < 300m) in the ECP region calculated from the Global Surface Summary of Day database (GSOD, version 8) provided by the National Climatic Data Center (NCDC), and the monthly Aerosol Optical Depth (AOD, 2001-2015) at 550nm derived from the Moderate Resolution Imaging Spectroradiometer (MODIS) onboard the Aqua and Terra satellites [72]. All these datasets, which are the currently available aerosol observations with the longest time series for the ECP region, have been widely used to study aerosol pollution in China [12, 73].

We examined two reanalysis datasets to evaluate ventilation conditions over the ECP region in January of the past three decades (Figure 4). The first one is the reanalysis data provided by the National Centers for Environmental Prediction and National Center of Atmospheric Research (NCEP/NCAR) [74], and the second one for cross-validation is the ERA-Interim data from the European Centre for Medium-Range Weather Forecasts (ECMWF) [75]. On the basis of 1981-2015 reanalysis data, we computed the horizontal ventilation index in Equation 1:

$$WSI_i^j = \left(WS_i^j - WS_{mean}^j\right)/WS_{std}^j \quad (1)$$

where WSI_i^j is the normalized wind speed index (unitless) for the j-th grid point of the ECP region in the i-th year, WS_i^j is the monthly mean wind speed (m/s) at 1000hPa for the j-th grid point in the i-th year derived from zonal and meridional winds of the reanalysis data, WS_{mean}^j is the climatological monthly wind speed (m/s) for the j-th grid point averaged from 1981 to 2010, and WS_{std}^j is the standard deviation of wind speed (m/s) for the j-th

grid point from 1981 to 2010. Gridded atmospheric temperature gradient anomalies as the vertical ventilation index were normalized in the same manner based on the monthly potential temperature gradient between the fields at 925hPa and 1000hPa. We then obtained WSI and ATGI for the ECP area by regional averaging. It is necessary to have one ventilation index for the ECP region to simplify the interpretation of the multivariate statistical analysis results, so we calculated PPI as a synthetic meteorological index for each grid point to obtain the spatial distribution and then averaged over the ECP region to obtain monthly time series, using a weighted average of WSI and ATGI in Equation 2:

$$PPI = \frac{r_1 \times WSI + r_2 \times ATGI}{|r_1| + |r_2|} \quad (2)$$

where r_1 and r_2 are the Person correlation coefficients of WSI (r_1 = -0.73) and ATGI (r_2 = 0.70) with *in situ* PM_{10} observations (Table 1). The diagnostic ventilation indices (WSI, ATGI, and PPI) derived from the two reanalysis datasets agree well with each other and the correlation between the two PPIs is 0.80 (Figure 4).

Table 1 – Correlations among ventilation indices, PM observations, and cryosphere forcing factors

Index	Data	WSI (1981-2015)		ATGI (1981-2015)		PPI (1981-2015)	
	Availability	r	p-value	r	p-value	r	p-value
PM_{10}–ECP	2005-2015	-0.73	<1E-2	0.70	<1E-2	0.92	<1E-3
$PM_{2.5}$–BJ	2010-2015	-0.80	0.01	0.58	0.09	0.79	0.07
ViI	1981-2013*	-0.63	<1E-3	0.36	0.17	0.62	<1E-3
Terra AOD	2001-2015	-0.43	0.08	0.33	0.26	0.44	0.08
Aqua AOD	2003-2015	-0.43	0.21	0.30	0.48	0.39	0.34
Arctic SIC	1980-2014	0.45	0.01	-0.26	0.29	-0.43	0.04
Asian SCE	1980-2014	-0.42	0.01	0.55	<1E-3	0.64	<1E-3
Boreal CFI	1980-2014	-0.51	<1E-2	0.49	0.01	0.65	<1E-3

To investigate the association of climate factors to the ventilation condition, we collected multiple climate variables for the past three decades (1980-2015) in Table 2. The first three meteorological indices were calculated based on the NCEP/NCAR reanalysis data [74] to describe characteristics of the EAWM system [76-78]. The next two climate indices, Arctic Oscillation (AO, internal atmospheric variability) [79] and El Niño/Southern Oscillation (ENSO) [80], were collected from the Climate Prediction Center (CPC) of the National Oceanic and Atmospheric Administration (NOAA). The last two cryosphere forcing factors are Arctic Sea Ice Concentration (SIC, Figure 3a) in the preceding autumn from the Met Office Hadley Centre (HadISST) [81], and boreal Eurasia Snow Cover Extent (SCE, Figure 3a) in early winter from the global snow lab at Rutgers University [82]. The cryosphere indices, SIC and SCE, were normalized in the same manner as WSI and ATGI. We first averaged the Arctic sea ice concentration within the

Arctic Circle (north of the 66.6° N, Figure 3a) in the preceding Autumn and early winter seasons (August-November) and Eurasian snow cover extent over the boreal region (60° E -150° E, 40° N - 75° N, Figure 3a) in early winter (October-November) for each year (1980-2014). We then normalized both variables with respect to their climatology (1981-2010) to obtain SIC and SCE in Equation 3,

$$Index_i = (X_i - X_{mean})/X_{std} \quad (3)$$

where X_i is the i-th year's cryosphere variable such as Arctic sea ice concentration or Eurasian snow cover extent, X_{mean} is the climatological average, X_{std} is the standard deviation for the same period, and $Index_i$ is the normalized index in the i-th year.

Table 2 – Climate and synoptic weather indices in the PCA analysis

Component	Index	Description	Equation/Data Source
Atmosphere	SHI	Normalized regional mean of the sea level pressure (SLP) in the center of the Siberian High in January	$\overline{P_{slp}}\,(40^\circ\ N - 60^\circ\ N, 70^\circ\ E - 120^\circ\ E)$ [74]
	ALI	Normalized regional mean of the SLP in the center of the Aleutian Low in January	$\overline{P_{slp}}\,(40^\circ\ N - 60^\circ\ N, 160^\circ\ E - 160^\circ\ W)$ [74]
	V850	Normalized regional mean meridional wind speed at 850hPa in January	$\overline{V_{850\text{hPa}}}\,(30^\circ\ N - 60^\circ\ N, 105^\circ\ E - 150^\circ\ E)$ [74]
	AO	Arctic oscillation index in January	NOAA CPC[79]
Ocean	MEI	Multivariate ENSO Index (MEI) in previous November-December	NOAA CPC[80]
Cryosphere	SIC	Arctic Sea Ice Concentration (SIC) index in previous August-November	HadISST[81]
	SCE	Eurasian Snow Cover Extent (SCE) index in previous October-November	GSL at Rutgers Univ.[82]

2.1.2 Statistical Analysis Approaches

We used multiple trend analysis approaches to examine the long-term trends in daily and monthly PPI time series. We first applied the quantile regression method [83] to daily PPI to obtain the trend information for each quantile of the variable with more

robustness against outliers. In comparison to the ordinary least square regression, the quantile regression enables a more comprehensive evaluation of the variability along the whole range of the variable distributions including extremes, which may have more sensitive responses to climate and meteorological drivers than mean values [84]. We then used the Matlab package for ℓ1 trend filtering provided by Kim *et al.* [85] (http://web.stanford.edu/~boyd/l1_tf/) to estimate long-term trends of monthly SIC and teleconnection time series. The ℓ1 trend filtering method produces piecewise linear trend estimation that is well suited to analyze abrupt changes in the underlying dynamics of the time series.

Statistical significance tests were used extensively throughout this study. We applied the moving-block bootstrap method [83] to examine if the January wind speed, temperature gradient, 850hPa geopotential height daily data of 2013 are statistically different from the 30-year (1981-2010) climatological January data in Figure 3. The moving-block bootstrap method removes biases introduced by autocorrelation of the data of time length L or shorter [83]. We collected the daily NCEP/NCAR reanalysis data [74] first and then regenerated the moving-block bootstrap samples for each grid point with the block length of L=5 days and a sampling size of 5000. The null hypothesis here was that the 2013 data and the 30-year data are statistically from the same probability distribution with equal means. For those grid points with p-values less than 0.01 (or 0.05), we rejected the null hypothesis and concluded that the values in 2013 over these areas were significantly different from the climatology at the 0.01 (or 0.05) significance level. We used the Student's t-test [83] to estimate the significance of correlation coefficients in Table

1, Table 3, Table 4 and composite differences in Figure 9 since all the data used here were the monthly mean values of each year.

We applied the Maximum Covariance Analysis (MCA) [68] to PPI and the geopotential height field at 850hPa (Z850) and 500hPa (Z500) to identify dominant circulation patterns affecting PPI over the ECP area. The MCA method performs a singular value decomposition of the covariance matrix of two variables to generate the coupled modes for the two variables separated in space and time dimensions. The temporal matrices are shown in Figure 6a and the spatial matrices are shown in Figure 6b and Figure 6c. The covariance of the two variables is maximized in the first mode. In our case, the first coupled MCA modes explain 33% of the covariance between Z850 and PPI fields, 23% of the Z850 variance, and 35% of the PPI variance. These MCA modes and results remain consistent in a sensitivity test, in which the 2013 data were excluded.

We examined the covariant relationship between PPI and all the climate indices for the last 35 years listed in Table 2 using the PCA analysis. PCA is a dimension reduction method [69] in order to identify the major factors contributing to the variation of the variable of interest, which is PPI in this study. All the climate data (Table 2) used in the PCA analysis were first detrended. We added these data into a 35×7 matrix and computed the PCs. For attribution analysis, we applied the Principal Component Regression (PCR) method [69] to regress the detrended PPI against the PCs and examined their regression coefficients in Equation 4,

$$\mathrm{Y}(t) = \sum_{j=1}^{7} \beta_j \, \mathrm{Z}_j(t) \tag{4}$$

where $Z_j(t)$ is the j^{th} PC as a function of time, $\beta_j (j = 1, \ldots, 7)$ is the corresponding regression coefficient, and $Y(t)$ is the regional ECP PPI as a function of time.

Lastly, we evaluated the phase relationship between two time series by using the wavelet coherence analysis package provided by Grinsted *et al.* (http://www.pol.ac.uk/home/research/waveletcoherence/) [70]. The wavelet analysis method is well suited to explore the linkage of two time series in time frequency space that is suggestive of causality between them [70]. To circumvent the influence of strong seasonality in SIC, we deseasonalized the monthly SIC data first and then analyzed its phase relationship with the teleconnection index from 1950 to 2016 in Figure 8.

2.2 Statistical Analysis Results

2.2.1 Temporal Variations of Winter Pollution Ventilation in China

In winter, horizontal ventilation of pollutants is through near surface wind advection, while the vertical dispersion is controlled by atmospheric stability, which is quantified by potential temperature gradient in the lower atmosphere. We examined the changes of horizontal and vertical ventilation from 1981 to 2015 using 1000hPa wind speed index (WSI) and the potential air temperature gradient index (ATGI) between 1000hPa and 925hPa, respectively, on the basis of the NCEP/NCAR [74] and ECMWF [75] reanalysis data. Both reanalysis data suggest decreasing WSI and increasing ATGI throughout the past three decades in Figure 4, indicating deteriorating ventilation conditions over the ECP

area in winter. As expected, the two ventilation indices (WSI and ATGI) are well correlated with historical haze observations including PM_{10} over the ECP region, $PM_{2.5}$ in Beijing, Visibility Inverse (ViI) [71], and satellite column Aerosol Optical Depth (AOD) data [72] (Table 1). Although precipitation is also an important factor removing PM through wet scavenging, previous studies indicated less significant dependence of PM concentrations on precipitation in winter [86], which was corroborated in our analysis. Therefore, we constructed a synthetic meteorological index, Pollution Potential Index (PPI), as a correlation weighted average of WSI and ATGI to simplify the multivariate statistical analysis (see Methods for details). The PM_{10} data suggest roughly equal weighting of horizontal ventilation (WSI) and vertical ventilation (ATGI) indices in PPI. The new proxy (PPI) correlates better with ground observations such as PM_{10} (r = 0.92), $PM_{2.5}$ (r = 0.79) and ViI (r = 0.62) than satellite AOD data (r = 0.39~0.44, Table 1 and Figure 3b), indicating that PPI is more representative for near-surface air quality than column aerosol loading. In general, we found an increasing trend in monthly PPI that is consistent with the weakening ventilation conditions. Such increasing trends are more significant at high quantiles of daily PPI (Figure 3b), suggesting more severe stagnant conditions favorable for extreme haze episodes in recent winters.

Since 2013 stands out clearly as an extreme case in terms of both strongly suppressed horizontal and vertical ventilation, we examined the air stagnation condition in that month specifically. In January 2013, the ECP region was characterized by large negative WSI (weakened horizontal ventilation, Figure 3c) and positive ATGI (stable atmosphere and weakened vertical dispersion, Figure 3d). In fact, the January ECP regional WSI < -2 and ATGI > 2 only occurred in 2013 in the past three decades (Figure 4). Those

unfavorable horizontal and vertical conditions contributed to a sharp peak of PPI in January 2013 that coincided well with haze observation peaks (Figure 3b). To reveal the underlying climate forcing factors, we applied the principal component analysis (PCA) to multiple climate indices in Table 2 including the EAWM intensity, the Arctic Oscillation, El Niño–Southern Oscillation, Eurasian snow cover extent (SCE), and Arctic sea ice concentration (SIC), for the past three decades (1980-2015) and then regressed PPI onto the key principal components. It is noted that the construction of PPI is not directly related to any atmospheric variable or forcing factor used here. By connecting PPI with critical climate factors through the key principal components, we are capable to decompose the PPI inter-annual variability into contributions from major climate variables and to identify dominant climate factors affecting PPI in the ECP area.

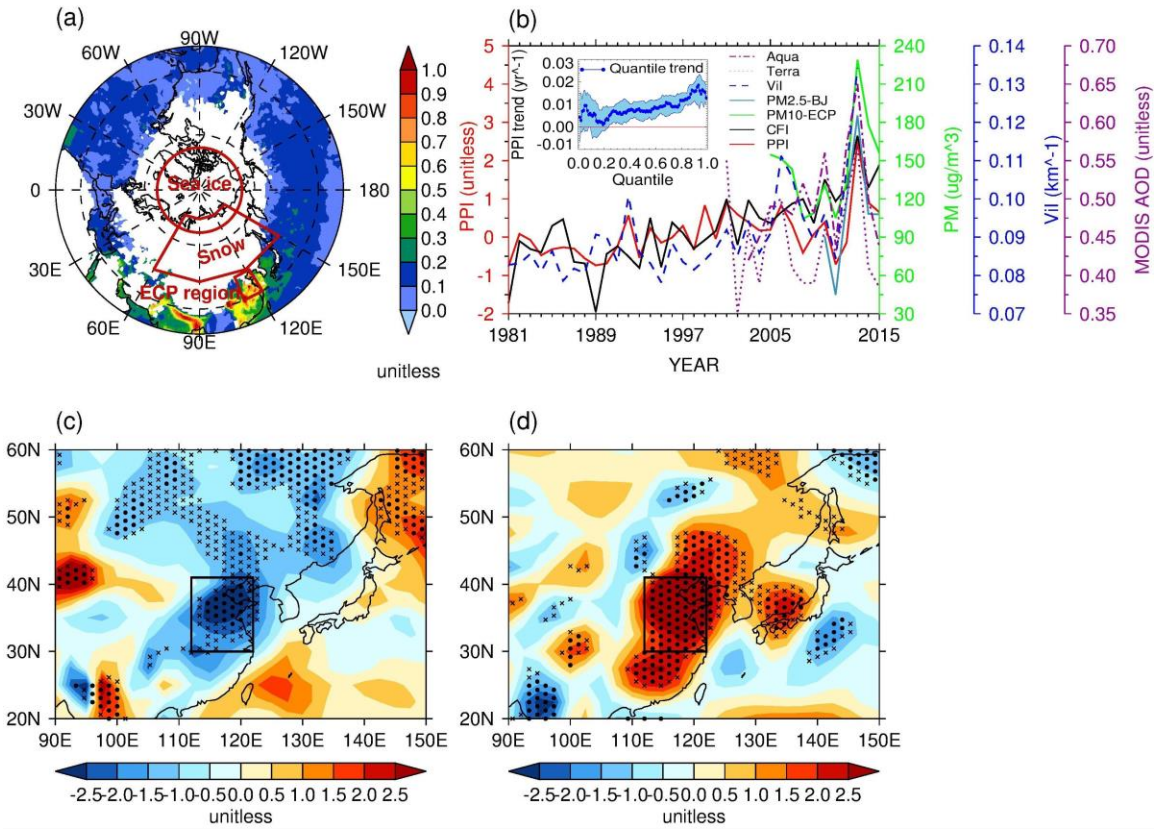

Figure 3 – Winter haze pollution and ventilation conditions over East Asia. (a) 2013 monthly Aqua satellite AOD (unitless) at 550nm; (b) time series of aerosol observations, PPI, and cryosphere forcing index; The long-term quantile trend in daily PPI is shown in the inlet; (c) 2013 distributions of normalized surface wind speed index (unitless); (d) 2013 distributions of normalized air temperature gradient index (unitless). In (c) and (d), black dots (crosses) denote the 0.01 (0.05) significance level. The red rectangular box in (a) and the black box in (c) and (d) show the ECP region. All results are for January.

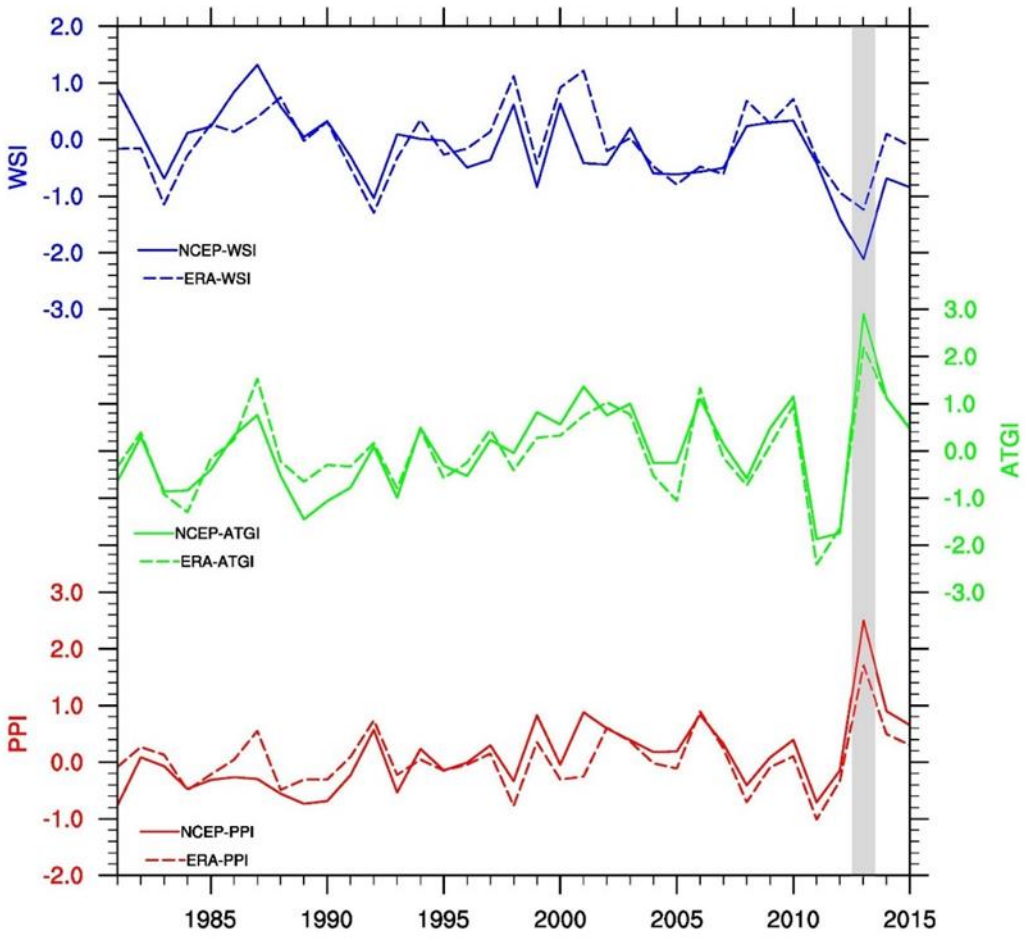

Figure 4 – Time series of monthly WSI, ATGI, and PPI over the ECP region for January.

2.2.2 Climate Driving Force Attribution

Table 3 shows the PCR regression coefficients and their p-values. We followed the principal component selection rule by Fekedulegn *et al.* [87] and found 3 major PCs (PC2, PC5, and PC6) that contributed to the ECP PPI significantly. Using the results from the PCR analysis, we found that these 3 PCs accounted for 53% of the ECP PPI variance while the inclusion of all PCs accounted for 57% of the variance.

Table 3 – PCR regression coefficients of detrended PPI onto PCs

PCR	PC1	PC2	PC3	PC4	PC5	PC6	PC7
Reg. coef.	0.03	-0.23	-0.05	-0.10	0.21	-0.44	-0.03
p-value	0.42	<1E-3	0.51	0.24	0.05	0.01	0.88

The correlation coefficients of PCs with detrended PPI in Table 4 show similar results that PC2, PC5, and PC6 are most significant. Also shown are the correlation coefficients of PCs with climate indices. Of particular interest to this study are the high correlations of SCE with PC5 (r = 0.83) and of SIC with PC6 (r = -0.80). Note that the PCA analysis is applied to climate indices only. The relationship between climate PCs and detrended ECP PPI is established using the PCR analysis. Therefore, the PCs explaining a large portion of the variance of climate indices are not necessarily correlated with PPI. For example, PC1 contributes most to the total variance of the matrix of climate indices, but it does not make significant contribution to the variance of detrended PPI.

Table 4 – Correlation statistics among PCs and climate indices

r	PPI	SHI	ALI	V850	AO	SIC	SCE	MEI
PC1	0.10	-0.50*	0.71*	0.75*	0.84*	0.45*	-0.22	-0.03
PC2	0.53*	-0.74*	-0.41*	0.43*	-0.39*	0.30	0.26	0.60*
PC3	0.08	0.02	0.37*	0.42*	-0.35*	-0.19	0.15	-0.62*
PC4	0.15	-0.32	-0.35*	-0.18	0.05	-0.04	-0.45	-0.50*
PC5	0.58*	-0.59*	-0.22	0.07	-0.16	0.18	0.83*	0.20
PC6	0.34*	-0.07	0.08	-0.03	0.01	-0.80*	-0.04	0.07
PC7	0.02	0.09	-0.24	0.16	0.07	-0.18	0.11	-0.05

* denotes the 0.05 significance level.

We highlighted the PCA results in Figure 5. PC6, related to Arctic sea ice forcing, is the most important, contributing 29% to the 2013 ECP PPI extreme and explains 12% of the total variance in detrended PPI. PC5, related with Eurasian snow forcing and the Siberia High variability, is the second most important, contributing 13% to the 2013 extreme as well as 34% to the total variance. PC2, related to El Niño/Southern Oscillation, is the third most important, contributing 8% to the 2013 extreme and 28% of the total variance. We added the PPI linear trend back to the contributions in Figure 5b. The PCR reconstructed PPI explained most of the variation of the original regional ECP PPI time series as well as the extreme in 2013, thereby placing the 2013 extreme in the context of the changes in the last 35 years. From 1981 to 2015, it was only in 2013 that the contributions of all three PCs are relatively large and more importantly all positive.

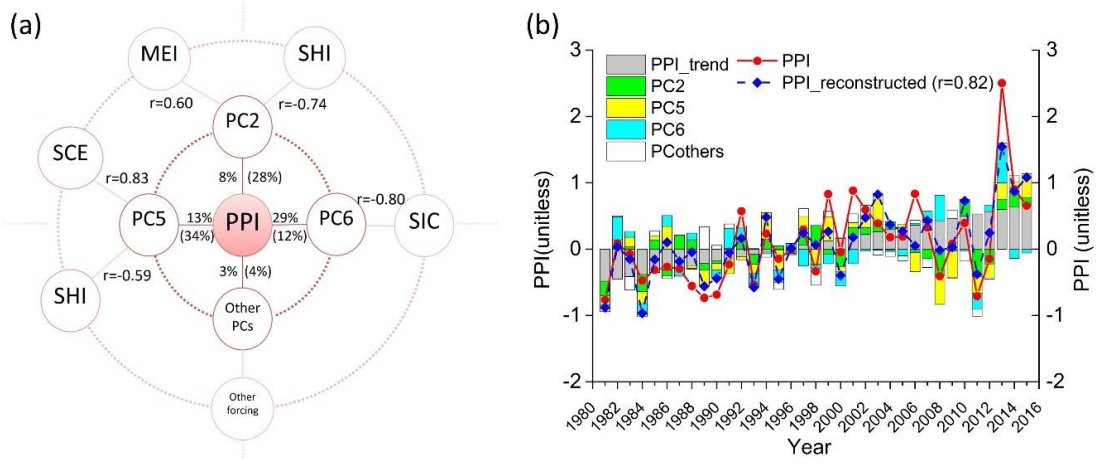

Figure 5 – PCA decomposition and reconstruction of PPI. (a) attributions of detrended PPI to PCs; percentages in the inner ring are contributions to the extreme PPI in January 2013 (without parentheses) and the total variance (with parentheses) by each PC; the climate indices most correlated with PC2, PC5, and PC6 are shown on the external ring; (b) comparison of original PPI and PCA reconstructed PPI; the PPI trend is added back to the reconstructed PPI. The correlation coefficient is shown in parenthesis.

The two cryosphere forcing factors correlate strongly with PC5 and PC6, which have larger contributions to the 2013 extreme than the other PCs. To facilitate the subsequent analyses, we combined the two forcing factors into a single normalized cryosphere forcing index, CFI, by weighted averaging SIC and SCE in a manner similar to the PPI formulation (Equation 5):

$$CFI = \frac{r_1 \times SIC + r_2 \times SCE}{|r_1| + |r_2|} \quad (5)$$

where r_1 and r_2 are the correlation coefficients of SIC (r_1 = -0.43) and SCE (r_2 = 0.64) with PPI, respectively, and the correlation between CFI and PPI is r =0.65 (Table 1). The CFI explains 45% of the PPI total variance, and the large CFI extreme corresponds well to the PPI extreme in 2013 (Figure 3b).

2.2.3 Synoptic Weather Patterns Conducive to Regional Air Stagnation

To examine the atmospheric processes linking cryosphere changes to PPI, we applied the Maximum Covariance Analysis (MCA) [68], totally independent from the PCA analysis, to analyze the association of mid- to high-latitude synoptic circulation (Z850/Z500) with PPI (see Methods for details). We note that the formulation of PPI is not directly related to the geopotential height field, that the region of interest for PPI (ECP) is of smaller domain than the height field, and that the MCA modes remain the same if 2013 data are excluded from the analysis. Since the EAWM system is mainly in the lower atmosphere, we first focused on Z850 to examine its relationship with PPI changes. The most dominant coupling modes of Z850 and PPI account for > 30% of the total covariance. The highest Z850 and PPI mode intensity also correspond to the extreme PPI value in 2013 (Figure 6a). The spatial pattern of the first MCA Z850 mode (Figure 6b) resembles the circulation anomaly in 2013 (Figure 6d). Similarly, the spatial pattern of the first MCA PPI mode resembles the PPI distribution in 2013 (Figure 6c). Furthermore, the time series of the intensity of the first MCA PPI mode is highly correlated with the average PPI over the ECP region (r = 0.93). Therefore, the extreme condition of 2013 can be understood using the more general MCA mode, i.e., the poor ECP ventilation condition represented by the first MCA PPI mode is driven by the regional circulation pattern represented by the first MCA Z850 mode. In contrast to the climatology characterized by large pressure gradients

between the continent and the oceans (Figure 6b), the first MCA Z850 mode shows a reversed northeast-southwest pressure gradient with anti-cyclonic anomalies in the Arctic and northeast Asia and a cyclonic anomaly over central Siberia, leading to weakened monsoon wind and increased PPI over the ECP region.

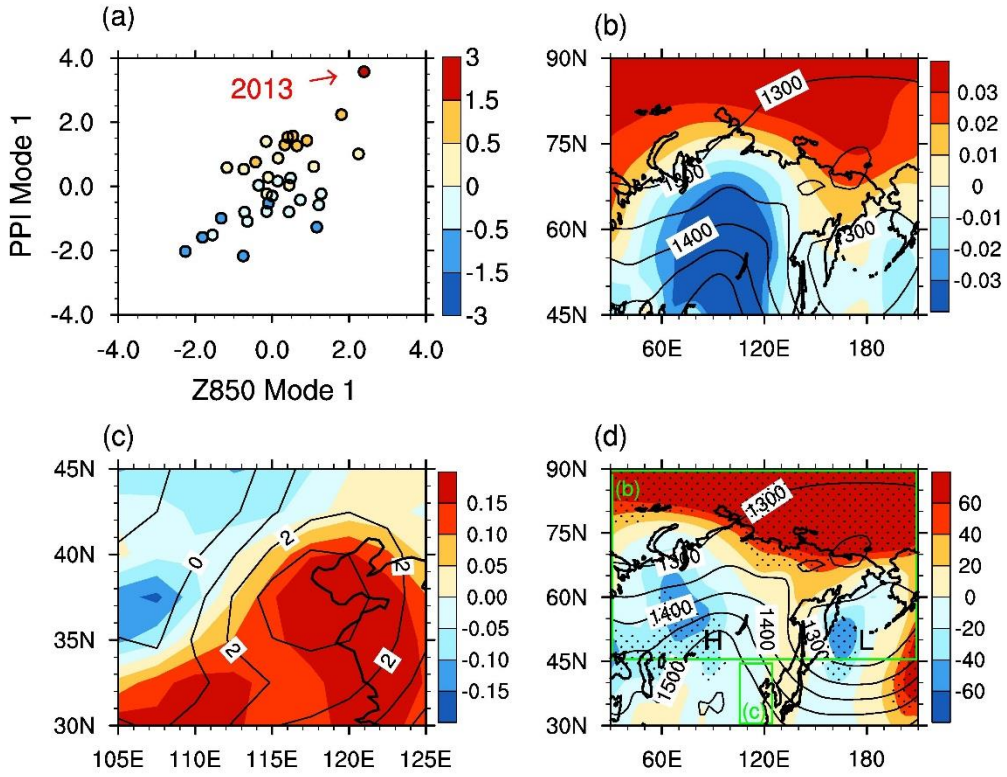

Figure 6 – Influence of the regional circulation on PPI. (a) The first MCA mode intensity (dots; unitless) of January PPI and Z850; color shading (unitless) denotes PPI values of 1981-2015; (b) the spatial pattern of the first Z850 MCA mode (color shading; unitless) and Z850 climatology (contour lines; units: m); (c) the spatial pattern of the first PPI MCA mode (color shading: unitless) and PPI (contour lines; unitless) over the ECP region in 2013; (d) the 2013 Z850 anomalies (color shading; unit: m) and Z850 climatology (contour lines; unit: m). In (d), black dots denote the

0.05 significance level; green rectangles denote the regions of subplots (b) and (c), respectively; H/L indicates the location of the Siberia High and the Aleutian Low, respectively. All results are for January.

We also applied MCA to Z500 and PPI to investigate the connection between the middle troposphere circulation and near surface ventilation. It turns out that the first MCA mode of Z500 resembles a regional manifestation of the East Atlantic (EA) teleconnection pattern [88]—the second prominent mode of atmospheric variability over the North Atlantic—with high spatial and temporal correlations (Figure 7). Therefore, we replaced the MCA mode with the EA pattern and reconfirmed its relationship with both Arctic sea ice forcing and PPI over the ECP region. We examined the phase relationship between time series of Arctic sea ice and EA from 1950 to 2016 using wavelet coherence analysis[70]. Figure 8 shows the continuous wavelet power spectrum of deseasonalized monthly Arctic sea ice concentration[81], monthly EA index [88], and cross wavelet transform of these two time series. There are clearly common features in the wavelet power spectrum of the two time series such as the significant peak around the 36-month (3-year) band after 2010. Both series also have high power in the 132- to 240-month (11- to 20-year) band in the last four decades, though parts of the time series are in the cone of influence (COI) region with possible distorted edge effects due to limited data length. We further examined the cross wavelet transform of SIC and EA and found significant common power mainly in the 32- to 64-month band from 1970 to 2000 and after 2005, the 96- to 128-month band between 1955 and 1980, and the 128- to 240-month band after 1990s. Since the decline of Arctic sea ice occurs significantly in the last three decades, we focused on the 128- to 240-month band and calculated the mean phase difference between the two time series based on data

within the 5% significance regions and outside the COI. In general, there is a 3- to 6-month lag in EA in response to SIC changes, which is consistent with the previous study [70].

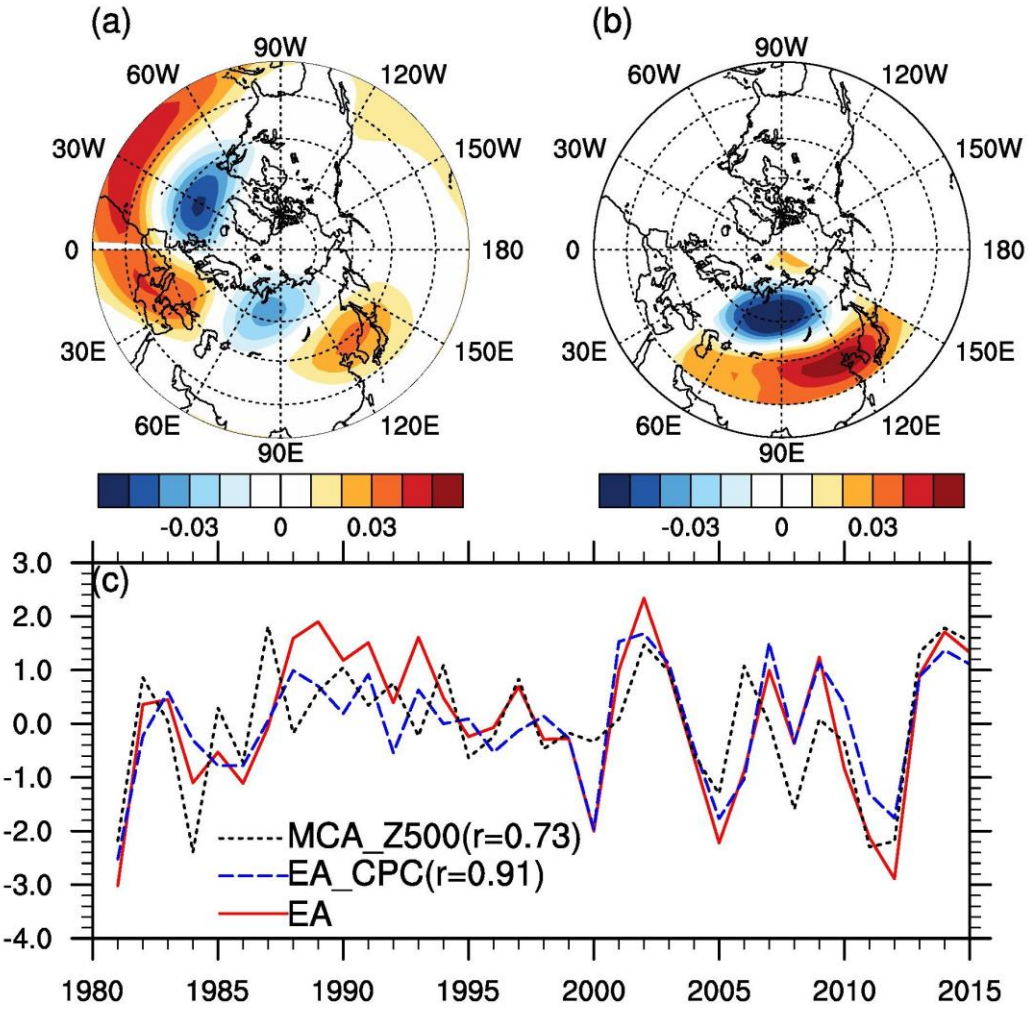

Figure 7 – Spatial and temporal comparisons of the EA teleconnection pattern and the MCA mode1 at 500hPa. (a) spatial distributions of the EA pattern identified in the NCEP reanalysis data; (b) spatial distributions of the MCA Z500 mode1; (d) time series of the MCA Z500 mode1 and the EA indices from the Climate Prediction

Center (CPC) and the identification of (a). r values in the parenthesis denote the correlation between each index and the EA index identified in (a).

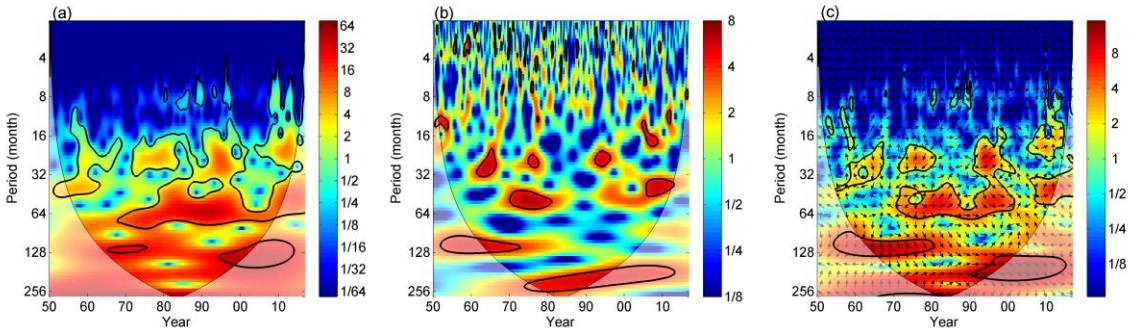

Figure 8 – Wavelet coherence analysis of the monthly SIC and EA indices. (a)continuous wavelet power spectrum of the monthly deseasonalized SIC index from 1950 to 2016; (b) same as (a) but of the monthly EA index; (c) cross wavelet transform of the deseasonalized SIC and EA time series. The black thick contour in (a)-(c) denote the 0.05 significance level. The arrows in (c) denote the relative phase relationship with in-phase pointing right, anti-phase pointing left, and SIC leading EA by 90° pointing straight down.

2.2.4 Hypothetical Connections from Climate Change to Air Stagnation

At last, we integrated the three climate forcing and regional stagnation datasets together in Figure 9 and compared their temporal variations and composite differences. In general, we have decreasing Arctic sea ice concentrations in autumn and early winter with accelerating decline rates after 2000 (Figure 9a). Meanwhile, EA shows a continuously increasing trend through the past three decades with more significantly positive shifts in the last ten years (Figure 9b). Considering different sea ice forcing intensity, we separated the whole winter time from 1981 to 2016 into two periods: before 2000 (P1, 1981-1999)

and after 2000 (P2, 2000-2016), and conducted composite analysis of ECP mean PPI and visibility inverse (ViI) [71] in terms of two periods and different EA phases (Figure 9c). Both PPI and ViI show consistent responses with increasing tendencies during the positive phase of EA and decreasing tendencies during the negative phase of EA. Such shifting tendencies are more significant in P2 with larger increases of PPI and ViI between positive and negative EA (regional mean ΔPPI=0.59 and ΔViI=0.02 km^{-1}, both significant at the 0.05 significance level), which are attributed to stronger Arctic sea ice forcing and more positive EA during this period. We also examined the temporal composite of PPI between P2 and P1 and found considerable enhancement of PPI over the East Asia coastal regions with ECP mean PPI increase by 0.37 in P2 (Figure 9d). Such PPI temporal variations are dominated by these P2 years in concurrence with positive EA since there is no significant change in winter PPI over the East Asia region between these P2 years with negative EA and P1 years (Figure 9e). When EA is in positive phase during the P2 period, the whole Eastern China region shows strong enhancement of PPI with drastically deteriorated ventilation conditions comparing to the P1 period as a benchmark (Figure 9f).

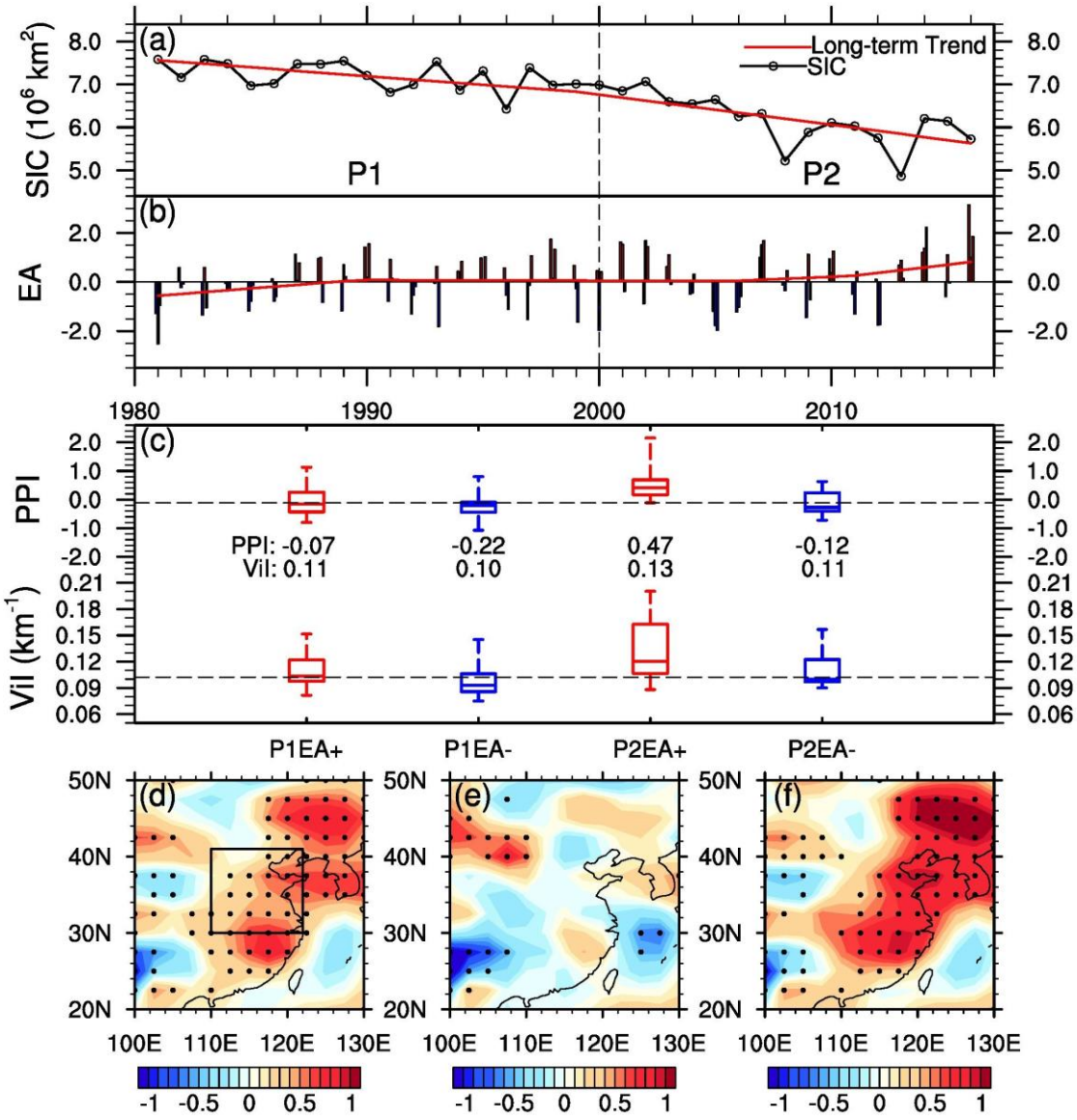

Figure 9 – Time series of observational Arctic sea ice concentrations and reanalysis-based EA index and their relationship with PPI and ViI over Eastern China. (a) Arctic sea ice concentrations in autumn and early winter (ASON) of 1980-2015 and their long-term trends; Note that the year axis in (a) shifts with 1 year lag for time alignment with (b); (b) monthly EA indices in winter (DJF) of 1981-2016 (year of January) and their long-term trends; (c) comparisons of ECP regional averaged PPI

and ViI in response to different phases of EA during two periods; The two periods are indicated by P1/P2 in (a); The numbers indicate the ensemble mean values; (d) spatial distributions of PPI differences between P2 and P1; the black box denotes the ECP region; (e) same as (d) but for PPI differences with concurrence of negative EA; (f) same as (d) but for PPI differences with concurrence of positive EA. In (d), (e), and (f), the black dots indicate the 0.05 significance level.

2.3 Conclusions

In this chapter, we applied multiple statistical analysis approaches to investigate the trend of regional air stagnation over the ECP area and its relationship with winter haze pollution and climate forcing variability. We revealed the increasing trend in air stagnation as suggested by the PPI time series and identified the key climate forcing factors driving PPI inter-annual variations. We found close relationship between deteriorating regional ventilation and preceding boreal cryosphere changes including declining Arctic sea ice and increasing Eurasian snow. We also analyzed the unfavorable synoptic circulation patterns that were conducive to deteriorated region ventilation and quantified their impacts on air stagnation and pollution in the ECP region. We concluded that more severe air stagnation and haze pollution over ECP in winter would occur during the positive phase of the East Atlantic pattern, which might be enhanced by the declining Arctic sea ice in autumn and early winter with a time lag of 3-6 months. We will conduct numerical modeling sensitivity experiments to evaluate these statistical relations and further reveal the underlying physical mechanisms with comprehensive dynamic diagnosis in the next chapter.

CHAPTER 3. NUMERICAL MODELING STUDIES OF THE IMPACT OF BOREAL CRYOSPHERE CHANGES ON REGIONAL AIR STAGNATION

The observational and reanalysis data suggested a potential linkage between Arctic sea ice forcing and regional PPI through the phase change of EA. We validated the hypothetical teleconnection pathway with ensemble numerical sensitivity experiments using the Community Earth System Model (CESM) [89] and the modeling dataset from the fifth phase of the Coupled Model Inter-comparison Project (CMIP5) under Representative Concentration Pathway 8.5 (RCP8.5) [23]. Following the analysis framework in the previous chapter, we extended our analysis to the entire boreal winter season (December-January-February, DJF) and calculated the monthly Pollution Potential Index (PPI) [18] over the ECP region (110-122° E, 30-41° N) based on surface wind speed and near surface vertical air temperature gradients of the NCEP/NCAR reanalysis data [74] and modeling results, respectively. We revisited the connection between China's air stagnation and boreal cryosphere changes and elucidated the teleconnection mechanism with comprehensive dynamic diagnosis. These dynamic analyses are imperative to identify the specific driving force of circulation changes and to understand detailed physical mechanisms for better interpretation of future predictions.

3.1 Sensitivity Simulation Experiments

We employed multiple climate models including the state-of-the-art Community Atmosphere Model version 5 (CAM5) [90] and the Whole Atmosphere Community Climate Model (WACCM) [91] under the modeling framework of CESM [89]. The Community Earth System Model (version 1.2.2) is a fully-coupled global climate model maintained by the Climate and Global Dynamics Laboratory (CGD) at the National Center

for Atmospheric Research (NCAR). It is composed of five major components of the earth system including atmosphere, land surface, ocean, sea ice and land ice, plus one central coupler component. As the atmosphere components of the CESM modeling system, CAM5 and WACCM provide low-top and high-top atmosphere simulation capabilities, respectively. The low-top CAM5 model has 30 vertical levels spanning the range of altitude from 1000hPa to 3.6hPa, while the high-top WACCM model has 70 vertical levels ranging from 1000hPa to 6×10^{-6}hPa. They are both coupled with an active Community Land Model version 4 (CLM4.0) at a horizontal resolution of 1.9°×2.5°. We compared different modeling outputs to better understand the impact of different modeling settings. We also examined the ensemble simulation results based on the 11 CMIP5 climate models (Table 5) to generate future predictions as well as to evaluate the modeling uncertainties more comprehensively.

3.1.1 Numerical Climate Models

1. CAM5

We designed four experiments to investigate impacts of the cryosphere forcing on PPI over the ECP region using the component set of the Community Atmospheric Model version 5 (CAM5) and the Community Land Model version 4.0 (CLM4.0) at a horizontal resolution of 1.9°×2.5°. In the control experiment (CTRL), we conducted a 30-year simulation (with another 1-year simulation as spin-up) with prescribed climatological (averaged from 1981 to 2010) Arctic sea ice concentrations (Figure 10a) and sea surface temperature from the Met Office Hadley Centre (HadISST) [81]. In sensitivity simulations, we used July of each modeling year from the CTRL simulation as initial conditions for the corresponding sensitivity ensemble member and conducted an 8-month simulation with different cryosphere forcing. In the first sensitivity experiment (SENS1), we replaced the

climatological SIC and SST data from August to November, which were used in the CTRL experiment, with observed cyclical (August 2012-November 2012) HadISST data [81] over the Arctic region (Figure 10b/c) following the method of Peings *et al*. [92]. In the second sensitivity experiment (SENS2), we introduced early winter snow forcing over boreal regions (60° E -150° E, 40° N -75° N, Figure 10d) by perturbing October to November snowing rates of each ensemble simulation based on the observed snow water equivalent (SWE) relative anomaly [93] in 2012 with the same climatological SIC/SST in the CTRL scenario. Therefore, we consider the snow forcing including the surface albedo effect and the insulation-related effect (e.g., thermal conductivity and latent heat flux due to snow depth changes) in SENS2, both of which can cause significant local temperature response [94]. The perturbation on modeling snow rates was performed using Equation 6,

$$Snow_1 = Snow_0 * (1.0 + swefrac) \quad (6)$$

where $Snow_0$ is the default modeling snow rate without perturbations, $Snow_1$ is the perturbed snow rate, and $swefrac$ is the observation-based SWE fractional anomaly by comparing 2012 anomalous SWE with the climatology (averaged from 1999 to 2010 due to limited dataset availability; $swefrac \geq -100\%$; Figure 10d). In the third sensitivity experiment (SENS3), we added both Arctic sea ice and boreal snow perturbations into the ensemble simulations to investigate their synergistic effects. Previous studies highlighted the importance of the tropical stratosphere representation in the model to capture the teleconnection between boreal cryosphere forcing and the subsequent winter circulation[95], therefore we designed the fourth sensitivity experiment (SENS4) with the same nudging method in Peings *et al.* [95] to account for the critical role of realistic

background flow in the tropical stratosphere. We implemented the nudging by adding an extra term to temperature (T) and horizontal wind components (u and v) in the equatorial stratosphere (top 11 levels above 150hPa within 20° S-20° N) at each time step in the model prognostic equations using Equation 8,

$$\frac{\partial X}{\partial t} = F(X) - \lambda(X - X_{ref}) \tag{7}$$

where X is the modeling state, X_{ref} is the reference field based on the temporal-interpolated NCEP/NCAR reanalysis data [74], and λ is the relaxation rate. The relaxation rates stay the maximum for the highest seven vertical levels (λ=1 above 80hPa) and decrease gradually to zero for the next four levels. The same smoothing process was also applied at the horizontal directions. Based on above sensitivity simulation settings, we analyzed the continuous December-January-February (DJF) data at the end of each sensitivity simulation to examine the seasonal impact of the cryosphere forcing.

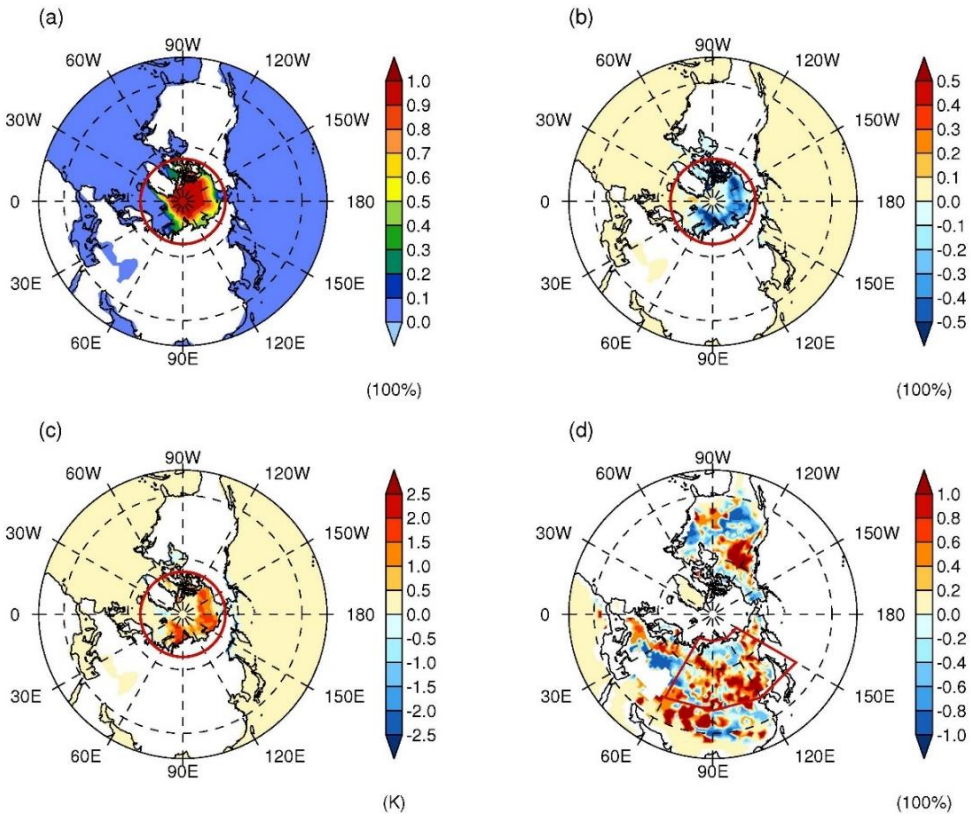

Figure 10 – Cryosphere forcing specifications used in the CESM numerical experiments. (a) Arctic SIC climatology (1981-2010) averaged from August to November (ASON); (b) Arctic SIC anomalies in autumn and early winter of 2012 (ASON averaged); (c) SST anomalies corresponding to SIC anomalies in (b); The red circles in (a), (b), and (c) denote the prescribed sea ice forcing region within the Arctic Circle (66.6 ° N); (d) Boreal SWE fractional anomalies averaged from October to November of 2012; the red polygon in (d) denotes the prescribed snow forcing region at mid- to high-latitudes (60° E-150° E, 40° N-75° N) in SENS2/3;

After numerical simulations, we calculated WSI, ATGI, and PPI over the ECP region for each scenario using the same method as those for reanalysis data. The CAM5 model uses a hybrid sigma-pressure vertical coordinate, so we extracted the modeling

outputs at the nearest pressure levels to the reanalysis data in the calculation. The 30-year CTRL results were used as the climatological condition against which sensitivity results were compared. To evaluate the seasonal impact of cryosphere forcing, we estimated the empirical Cumulative Density Function (CDF) based on N=90 ensemble members (December-January-February) for each sensitivity simulation.

To obtain the intensity of the dominant MCA modes in simulated Z850 and PPI fields, we projected the modeling fields onto the spatial patterns of the first MCA modes identified in the reanalysis data (Figure 6b/c) and estimated the MCA mode intensity of each ensemble member. The density distributions of the first pairwise MCA modes in Figure 11 were estimated by using the two-dimensional Kernel Density Estimation (kde2d) function included in the math package of R. By comparing density distributions of the sensitivity experiments to the control experiment, we evaluated the response sensitivities of both geopotential height and PPI fields to the specific cryosphere forcing.

2. WACCM

We used the same experiment settings with the CAM5 experiments in the WACCM sensitivity simulations under the common CESM numerical framework. We conducted 30-year simulations (with another 1-year simulation as spin-up) as the CTRL run with prescribed climatological (averaged from 1981 to 2010) Arctic sea ice concentrations and sea surface temperature from the Met Office Hadley Centre (HadISST) [81]. We then branched an 8-month simulation from each July of the CTRL run with observed Arctic SIC/SST data [81] in autumn and early winter of 2012 (August-November) as the SENS run. We chose 2012 since it has the lowest level of Arctic sea ice concentrations through

the satellite era of the last few decades and provides strong enough disturbances to climate systems in sensitivity experiments. We analyzed the continuous December-January-February (DJF) data at the end of each sensitivity simulation to examine the seasonal impacts of the Arctic sea ice forcing in comparison with observation and reanalysis results. The EA indices were estimated by projecting modeling differences (SENS-CTRL) onto the reanalysis-based EA pattern, and the PPI indices were calculated using the same method of the reanalysis ones. We also quantified the snow impact on regional air stagnation in Figure 12 by identifying those SENS members with anomalously large snow (SENS_EA+snow: SENS months with both positive EA and standardized snow amounts > 0.5 standard deviation) over the ECP region.

3. CMIP5

Table 5 lists the 11 CMIP5 models used to verify the sensitivity relationship among Arctic sea ice, the EA teleconnection pattern, and regional PPI in China. We collected historical simulations (1980-2005) and future projections (2006-2100) under a high greenhouse gas emission pathway (RCP8.5) [23] for each model to keep consistent with previous future prediction studies [19, 24]. We then calculated time series of regional averaged Arctic SIC, northern hemisphere EA based on geopotential height anomalies at 500hPa, and PPI over the ECP region for all 11 model to get ensemble means and standard deviations. It's worth noting that the trend of Northern Hemisphere mean 500hPa geopotential height fields were removed from the height anomalies before EA calculation for better comparisons among different climate periods. We then projected the detrended height anomalies onto the EA pattern identified in the reanalysis data to obtain its time series. PPI of each model was calculated following the same method of the reanalysis data.

Table 5 – the 11 CMIP5 models used in this study

Model Name	Modeling Center	Institute ID	Ensemble
CanESM2	Canadian Centre for Climate Modeling and Analysis	CCCMA	r1i1p1
CCSM4	National Center for Atmospheric Research	NCAR	r1i1p1
CMCC-CM	Centro Euro-Mediterraneo per I Cambiamenti Climatici	CMCC	r1i1p1
CNRM-CM5	Centre National de Recherches Meteorologiques / Centre Europeen de Recherche et Formation Avancees en Calcul Scientifique	CNRM-CERFACS	r1i1p1
GISS-E2-R	NASA Goddard Institute for Space Studies	NASA GISS	r1i1p1
HadGEM2-CC	Met Office Hadley Centre	MOHC	r1i1p1
INM-CM4	Institute for Numerical Mathematics	INM	r1i1p1
IPSL-CM5A-LR	Institut Pierre-Simon Laplace	IPSL	r1i1p1
MPI-ESM-MR	Max Planck Institute for Meteorology	MPI-M	r1i1p1
MPI-ESM-LR	Max Planck Institute for Meteorology	MPI-M	r1i1p1
NorESM1-M	Norwegian Climate Centre	NCC	r1i1p1

3.1.2 Statistical Analysis Methods

We used statistical functions in NCL (http://www.ncl.ucar.edu/Applications/extreme_value.shtml) to estimate the cumulative distribution functions (CDFs) of the Generalized Extreme Value (GEV) distributions [96] as well as the probability of extreme events based on reanalysis and modeling samples. We estimated the CDF parameters for the GEV distributions based on the reanalysis and modeling benchmark data to determine the threshold of positive extremes ($\geqslant 0.95$ percentile), and then calculated the probability of extreme events based on fitted GEV CDFs of corresponding scenarios. These extreme value analyses provide us another perspective from the traditional ensemble mean statistics to better understand the atmosphere response to climate disturbances. we employed the bootstrap method [83] to estimate the statistical significance of EA and PPI positive extreme value probabilities in P2 and SENS in Figure 14. We first used the GEV fitting [96] to estimate the CDFs of EA and PPI based on the P1 and CTRL data, which serve as the benchmark for the reanalysis and modeling results, respectively. We then determined the thresholds of positive extremes of EA and PPI as the 95th percentiles of P1 and CTRL (EA_{P1}^{95th},PPI_{P1}^{95th};EA_{CTRL}^{95th}, PPI_{CTRL}^{95th}) for the reanalysis and modeling data. We refitted the GEV distributions for both EA and PPI in P2 and SENS using the bootstrap method with nboot=5000 and compared the generated CDFs to the above 95th extreme value thresholds to estimate the statistics of positive extreme occurrence probabilities. All other statistical significance of reanalysis and simulation results were evaluated by the Student's t-test throughout this chapter.

3.1.3 Dynamic Diagnosis Tools

We employed multiple dynamic diagnostic tools including the Extended Eliassen-Palm vectors [97] (hereafter referred to as **E**), eddy-induced geopotential height tendency at 250hPa [98], phase-independent 3-dimensional wave activity flux (WAF) [99], and a piecewise potential vorticity (PV) inversion method [100] to understand the teleconnection relationship revealed by the statistical analysis. The horizontal components of the 2-8 day band-pass-filtered daily **E** were given by Trenberth [97] in Equation 8 to describe transient eddy properties:

$$\frac{1}{2}\left(\overline{v'^2} - \overline{u'^2}\right)\mathbf{i} - \overline{u'v'}\mathbf{j} \tag{8}$$

where *u* and *v* are the zonal and meridional wind components, respectively, and the prime denotes the bandpass-filtered quantities.

The daily fields of the 250hPa geopotential height tendency induced by the convergence of transient eddy vorticity flux were given by Lau and Holopainen [98] and estimated in Equation 9,

$$\left(\frac{\partial Z_{250}}{\partial t}\right)_{eddy} = \frac{f}{g}\nabla^{-2}[-\nabla\cdot(\overline{V'\zeta'})] \tag{9}$$

where f is the Coriolis parameter, g is the gravity acceleration rate, V is the horizontal wind vector, and ζ is the relative vorticity.

Equation 10 shows the phase-independent 3-dimensional wave activity flux[99] based on the monthly reanalysis and modeling data to diagnose zonal propagation of locally

forced wave packet induced by small amplitude quasi-geostrophic eddy disturbances on a zonally varying basic flow.

$$\mathbf{W} = \frac{p\cos\emptyset}{2|\mathbf{U}|}\begin{bmatrix} \frac{U}{a^2\cos^2\emptyset}\left[\left(\frac{\partial\psi'}{\partial\lambda}\right)^2 - \psi'\frac{\partial^2\psi'}{\partial\lambda^2}\right] + \frac{V}{a^2\cos\emptyset}\left[\frac{\partial\psi'}{\partial\lambda}\frac{\partial\psi'}{\partial\emptyset} - \psi'\frac{\partial^2\psi'}{\partial\lambda\partial\emptyset}\right] \\ \frac{U}{a^2\cos^2\emptyset}\left[\frac{\partial\psi'}{\partial\lambda}\frac{\partial\psi'}{\partial\emptyset} - \psi'\frac{\partial^2\psi'}{\partial\lambda\partial\emptyset}\right] + \frac{V}{a^2}\left[\left(\frac{\partial\psi'}{\partial\emptyset}\right)^2 - \psi'\frac{\partial^2\psi'}{\partial\emptyset^2}\right] \\ \frac{f_0^2}{N^2}\left\{\frac{U}{a\cos\emptyset}\left[\frac{\partial\psi'}{\partial\lambda}\frac{\partial\psi'}{\partial z} - \psi'\frac{\partial^2\psi'}{\partial\lambda\partial z}\right] + \frac{V}{a}\left[\frac{\partial\psi'}{\partial\lambda}\frac{\partial\psi'}{\partial z} - \psi'\frac{\partial^2\psi'}{\partial\lambda\partial z}\right]\right\} \end{bmatrix} + \mathbf{C}_U M \tag{10}$$

Here *U and V* are the horizontal and meridional wind vectors, respectively. $\mathbf{U} = (U, V, 0)^T$ is a steady zonally inhomogeneous basic flow. $p = (\text{pressure}/1000\text{hPa})$ is normalized pressure, ψ' is a perturbation streamfunction, $(\emptyset, \lambda)$ are latitude and longitude, a is the earth's radius, f is the Coriolis parameter, $N^2 = (R_a p^\kappa / H)(\partial\theta/\partial z)$ is the squared buoyancy frequency, $\mathbf{C}_U$ represents the phase propagation in the direction of $\mathbf{U}$, and M can be interpreted as a generalization of small-amplitude pseudo-momentum for QG eddies onto a zonally varying basic flow.

Lastly, we quantified the influence of circulation anomalies at different levels using a piecewise potential vorticity (PV) inversion method [100]. The PV anomalies were calculated with reanalysis and simulation data for all pressure levels from 1000hPa to 100hPa in Equation 11,

$$q' = \frac{1}{f}\left[\frac{1}{(a\cos\phi)^2}\frac{\partial^2}{\partial\lambda^2} + \frac{f}{a^2\cos\phi}\frac{\partial}{\partial\phi}\left(\frac{\cos\phi}{f}\frac{\partial}{\partial x}\right) + f^2\frac{\partial}{\partial p}\left(\frac{\partial}{\partial p}\right)\right]\Phi' \tag{11}$$

where q is the potential vorticity, Φ is the geopotential height, f is the Coriolis parameter, and a prime represents the deviation from the smoothed climatological annual cycle. We then inverted individual PV "pieces" at different levels to evaluate near surface circulation responses (850hPa) to these PV anomalies. The horizontal anomalous wind field in Figure 16 was derived from the geopotential height field based on geostrophic balance. We partitioned the influence of lower troposphere (1000-850hPa) and middle to higher troposphere (700-100hPa) PV anomalies and compared their differences in the next section.

3.2 Numerical Results and Discussion

3.2.1 CAM5 Sensitivity Simulations

To diagnose the response of regional circulations to cryosphere forcing, we first examined the cumulative distributions of PPI and the strength change of the first pairwise MCA modes of Z850 and PPI shown in Figure 11 in each CAM5 sensitivity experiments. The empirical cumulative distribution function (CDF) in the CTRL scenario shows a similar distribution with the NCEP data except at two tails (Figure 11a), suggesting a positive-skewed distribution in the reanalysis due to strengthening cryosphere forcing. All sensitivity scenarios shift towards the positive direction comparing to the CTRL case, especially at larger percentiles with high PPI values, implying higher probabilities of unfavorable meteorological conditions and deteriorated ventilation under strong cryosphere forcing. In the high percentile interval with extreme PPI values, SENS4 demonstrates the largest increase in both numbers and magnitudes of extremes that is comparable with the NCEP data. These changes in PPI distributions are attributed to

variations in the strength of MCA modes in each scenario. For instance, CTRL in Figure 11b shows a symmetric distribution in the strengths of the first MCA modes and a higher population density towards the origin. When SIC and SST in August-November are prescribed with 2012 observations, SENS1 shows a clear shift towards positive Z850 and PPI modes relative to CTRL (Figure 11b). However, there is only a non-significant increase of PPI values of 0.09 on average (p = 0.18). The number of extreme members with PPI above the 95th percentile of the CTRL results ($\mathrm{PPI}_{\mathrm{CTRL}}^{95^{\mathrm{th}}} = 1.05$) remains the same in SENS1 with that in CTRL. Prescribing October and November snow data as observed in 2012 induces a larger increase in ensemble average PPI of 0.23 (p = 0.01) and the number of extreme members increases by a factor of ~2. But there is no clear shift pattern in the MCA modes of SENS2 (Figure 11c), implying deviated variations in PPI and the corresponding modes. Actually, the correlation between the Z850 mode and PPI is nonsignificant (r=0.15, p=0.17) and the increase of PPI values in SENS2 can only be explained by snow-induced temperature inversion rather than by unfavorable regional circulations. The inclusion of prescribed 2012 sea ice and snow observations in SENS3 leads to a significant increase in the mean PPI value (ΔPPI=0.20, p=0.01) and the number of extremes (×2.3). The same cryosphere forcing under a more realistic representation of tropical stratosphere in SENS4 results in the largest increase of ensemble mean PPI to 0.29 ($p=1.9\times10^{-3}$) and an increase by a factor of 3.5 in the number of extreme PPI members. Both increases of PPI values in SENS3 and SENS4 are closely related with the positive shift of the MCA modes (Figure 11d/e), suggesting synergic impacts of unfavorable circulations and local temperature inversion contributed by the cryosphere forcing.

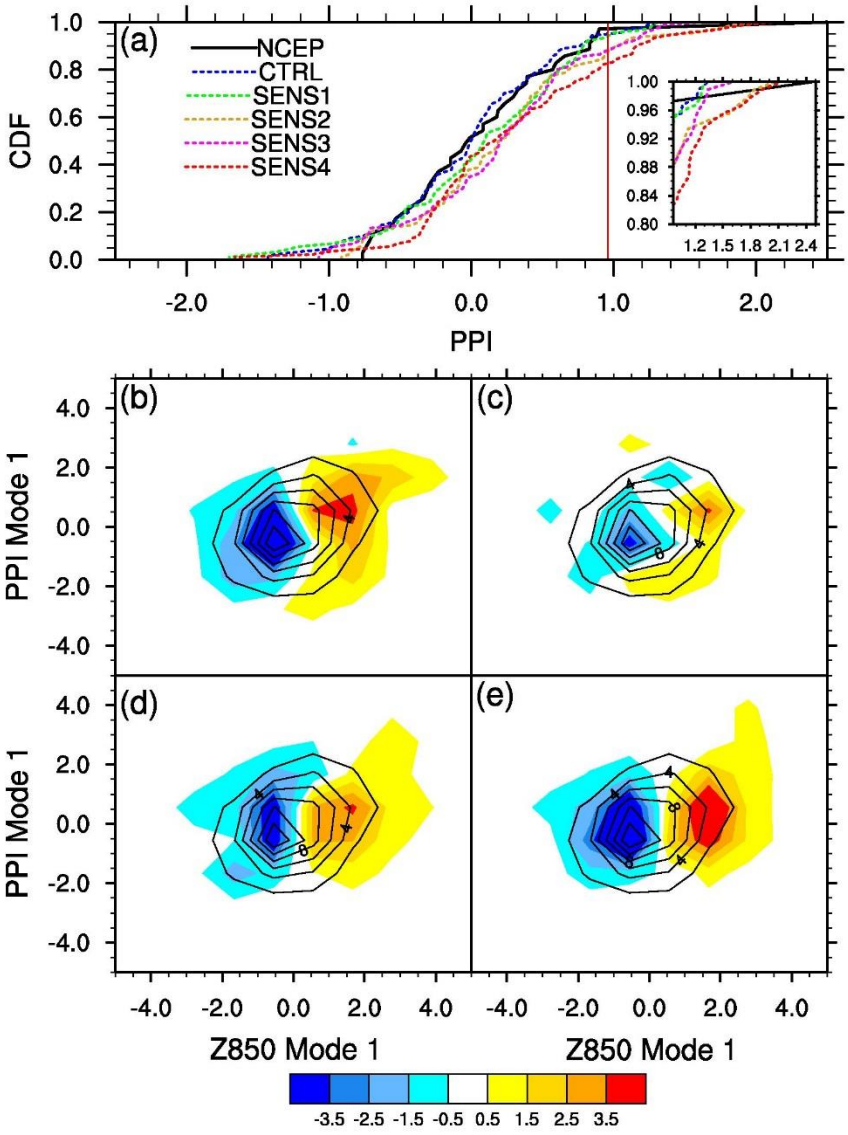

Figure 11 – The sensitivity response of PPI to cryosphere forcing. (a) empirical cumulative distribution function (CDF) of PPIs in NCEP reanalysis and CESM sensitivity scenarios; the red solid line denotes the 95th percentile value of PPI in the CTRL case ($PPI_{CTRL}^{95^{th}}$); (b) the two-dimensional kernel density estimation of the first MCA modes in CTRL (contour lines from 2% to 12% at intervals of 2%) and density

differences between SENS1 and CTRL (color shading; units: %); (c)-(e) the same with (b) but for differences between SENS2, SENS3, SENS4 and CTRL, respectively.

There appears to be an increasing trend of winter cold extremes in the northern high latitudes [101], which is partially attributable to the Arctic sea ice loss [102-104]. Meanwhile, winter snowfall over Eurasia has also increased [105, 106]. In 2012, most boreal regions suffered a chilly early winter with anomalously heavy snowfalls following a record-breaking decline of Arctic sea ice in September 2012. The cold anomaly is particularly apparent in the northern Eurasia in subsequent months and model sensitivity results suggests its formation is attributable to both Arctic sea ice and Eurasia snow forcing (Figure 12). Some of the dynamic response to cryosphere forcing can be explained by the strengthening of upward propagation of Rossby wave into the stratosphere and the weakening of the stratospheric polar vortex as well as stratosphere-troposphere coupling processes (Figure 13) [27, 107]. However, this analysis tends to emphasize the more zonally symmetric forcing of Arctic sea ice and likely underestimates the asymmetric Eurasia snow forcing. Our numerical experiments suggest higher sensitivity of ECP ventilation to boreal snow enhancement in SENS2/3/4 than to Arctic sea ice loss in SENS1, especially under the specific background flow in the tropical stratosphere to build up the teleconnection [95]. Both higher statistical correlation and modeling sensitivity imply the dominant role of asymmetric snow forcing in modulating the regional ventilation over Eastern China, though sea ice melting also constructively facilitates the adverse circulations to a certain extent. Nonetheless, Figure 11 provides clear evidence that the concurrence of Arctic sea ice decline and boreal snow expansion contributes most to the reinforcement of the unfavorable circulation pattern such as the Z850 MCA mode1 as well

as strong local temperature inversion, which further induces the enhancement of PPI as well as the deterioration of ECP ventilation.

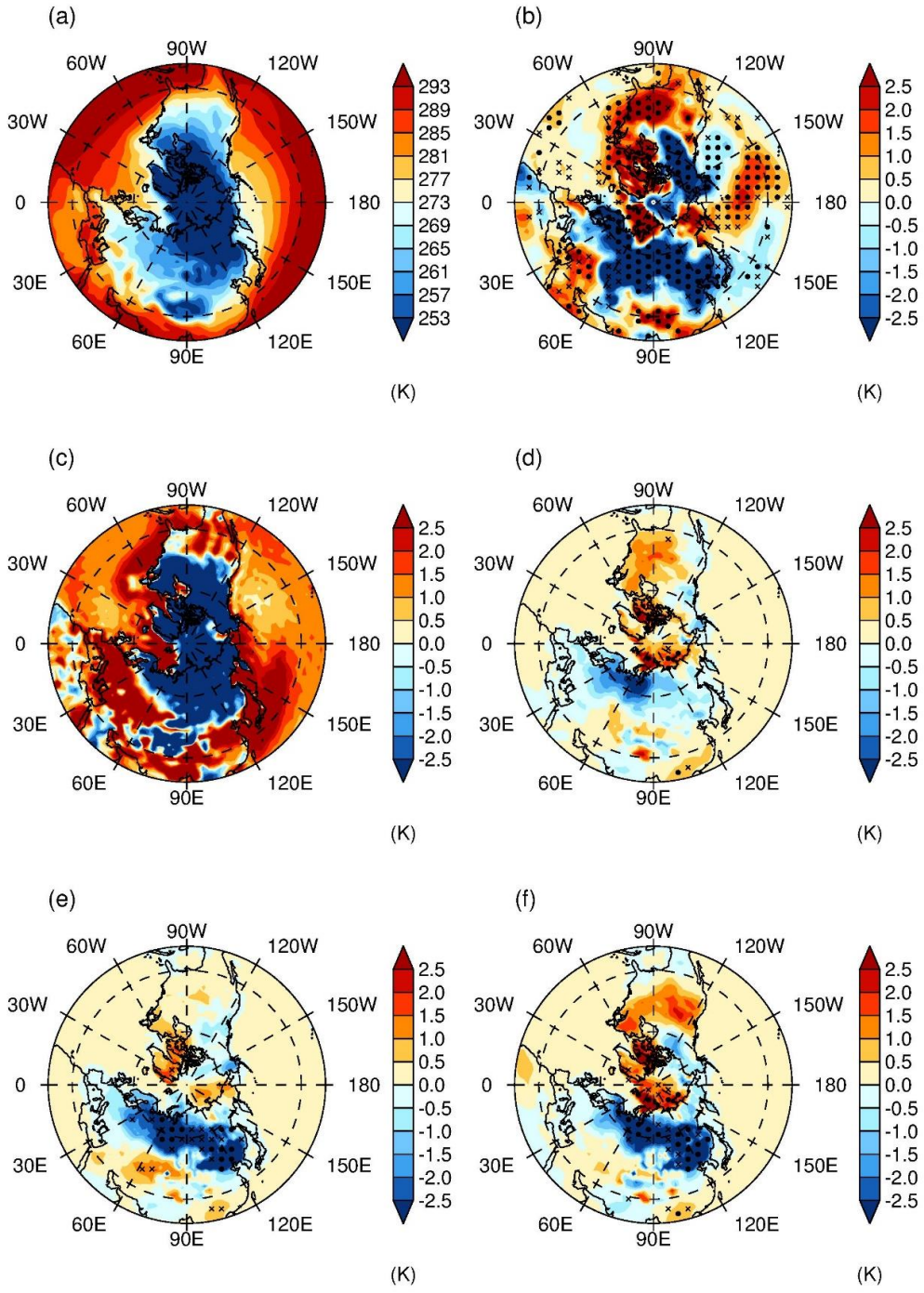

Figure 12 – Comparison of Surface Air Temperature (SAT) in December in NCEP reanalysis data and numerical simulations. (a) SAT climatology (1981-2010) in reanalysis; (b) SAT anomalies in December 2012 in reanalysis; (c) differences in SAT

climatology between the CTRL simulation and the reanalysis; (d) ensemble averaged SAT responses in SENS1 (SENS1-CTRL); (e) the same with (d) but in SENS2; (f) the same with (d) but in SENS3; In (b), (d), (e), and (f), black dots (cross) denote the 0.01 (0.05) significance level.

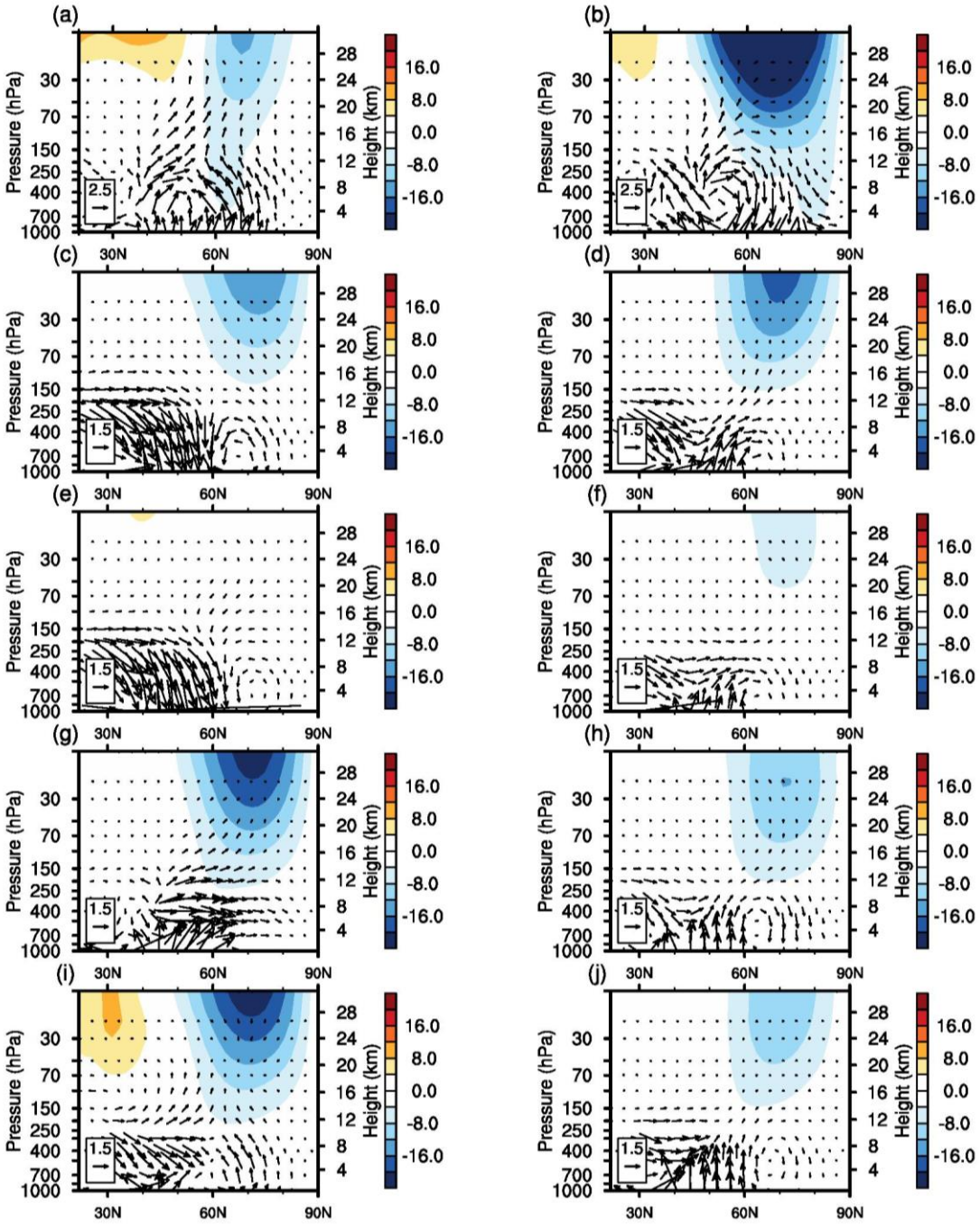

Figure 13 – Comparison of anomalous wave activity flux (WAF) and zonal winds in reanalysis and modeling simulations. (a) zonal mean WAF anomalies over East Asia (60° E -180° E, vectors; units: m^2/s^2) and anomalous zonal winds in December 2012 (color shading; units: m/s); (b) the same with (a) but for January 2013; (c) zonal mean

WAF differences over East Asia (vectors; units: m^2/s^2) and zonal wind differences (shading; units: m/s) between SENS1 extreme members and CTRL ensemble mean in November; (d) the same with (c) but for modeling December-January in SENS1; (e)-(f) the same with (c)-(d) but for SENS2; (g)-(h) the same with (c)-(d) but for SENS3; (i)-(j) the same with (c)-(d) but for SENS4. All the vertical components of vectors in (a)-(h) are scaled by 100 for clear illustration.

3.2.2 WACCM Sensitivity Simulations

We then used the high-top WACCM model with higher vertical resolutions instead of the low-top CAM5 model to verify the modeling sensitivity results. We compared the winter geopotential height fields at 500hPa between SENS and CTRL and projected the DJF monthly differences (SENS-CTRL) onto the reanalysis based EA pattern (Figure 14). We then fitted the 90 (30 years × 3 months) ensemble samples using the Generalized Extreme Value (GEV) distribution [96] and examined changes of both ensemble mean and positive extremes between SENS and CTRL. It's clear that the winter EA in SENS shifts towards its positive phase comparing to EA in CTRL with ensemble mean increase of 0.12 and positive extreme occurrence probability increased by 60% (8%±2%; Figure 14a). Such simulated positive shifting extent is weaker than that of the reanalysis data from P1 to P2 (18%±5%) but still significant at the 0.05 significance level. It is worth noting that we only changed the surface boundary conditions (SIC/SST) at these modeling grids with sea ice changes larger than 10% and kept other ocean grids unperturbed. Such static data ocean setting results in a lack of ice-ocean-atmosphere coupling and may attenuate the sea ice forcing as discussed in previous studies[108]. Considering the PPI responses, a similar positive shift is also observed in SENS in comparison to CTRL. The ensemble mean PPI

increases to 0.07 and the positive extreme probability of PPI increases to 9% (9%±2%)with a fold change of 0.8, both of which are smaller than the changes in the reanalysis data (mean change:0.37; extreme probability:16%±6%; Figure 14b). Figure 14c shows the comparison between ensemble members in different EA phases of CTRL and SENS, which confirms increasing PPI from CTRL to SENS as well as the enhancement effect of positive EA on PPI changes in both CTRL and SENS experiments. Moreover, PPI increases further to the highest ensemble mean of 0.42 with the concurrence of all unfavorable conditions including declined sea ice, positive EA, and anomalously heave snow over the ECP region (SENS_EA+snow, see Methods for details), which agrees well with the previous findings[18]. The PPI spatial distributions clearly demonstrate significantly positive enhancement over the whole Northern China regions (Figure 14d), which is dominated by these members with positive EA (Figure 14f) rather than those with negative EA (Figure 14e). It's also noted that negative EA has much stronger impacts on regional PPI in sensitivity simulations (Figure 14e) than that of the reanalysis data (Figure 14e), which could partly explain the damped response in the ensemble mean PPI with all members (Figure 14d).

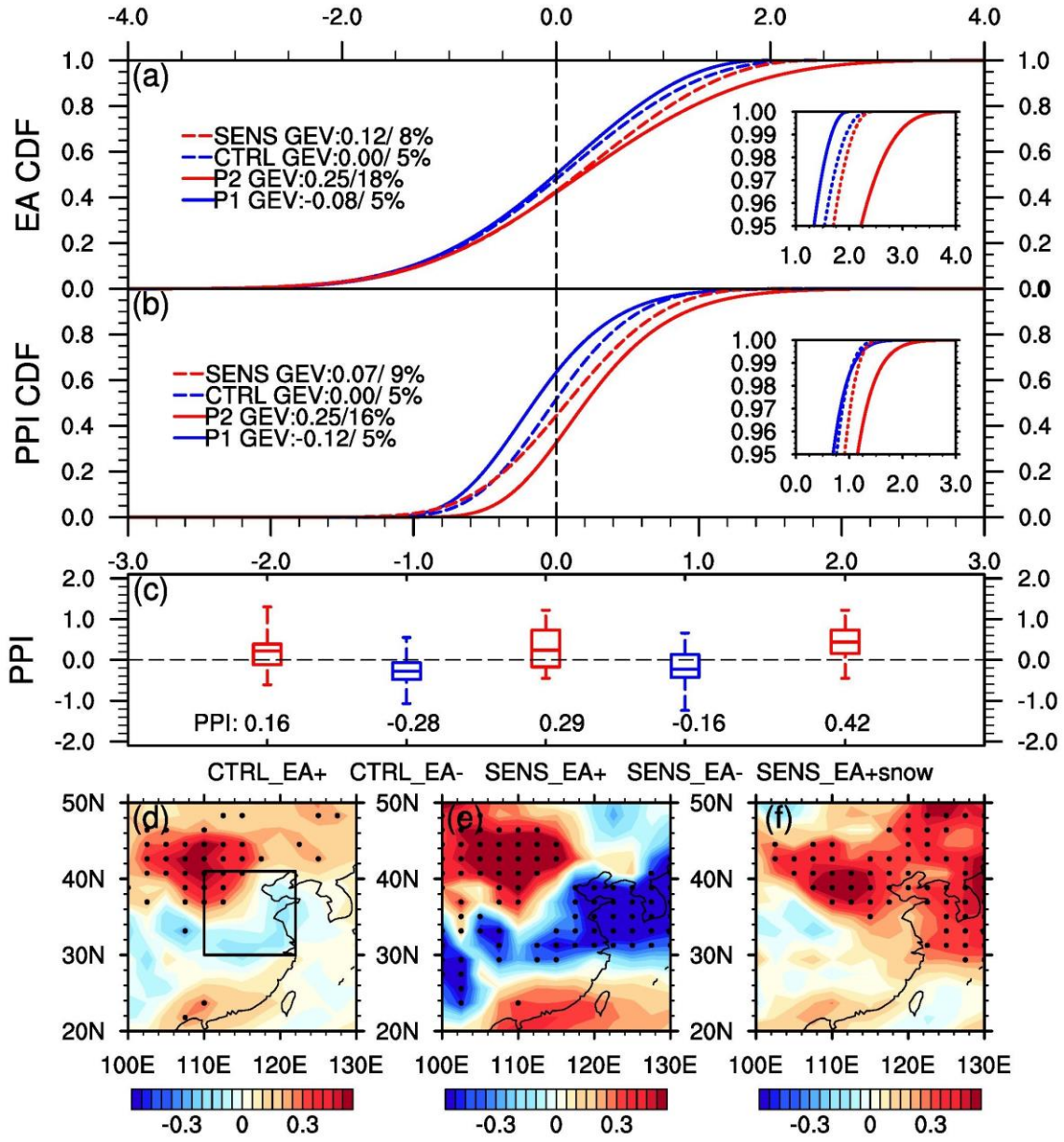

Figure 14 – Variations of winter (DJF) EA and PPI in the reanalysis data and numerical sensitivity experiments. (a) CDFs of EA in P1 and P2 of the reanalysis data and in CTRL and SENS experiments; The inlet shows the positive extreme changes; The numbers indicate the ensemble mean values and positive extreme occurrence probabilities; (b) same as (a) but for PPI changes; (c) comparisons of ECP regional averaged PPI in responses to two different phases of EA in CTRL and SENS

experiments; The numbers indicate the ensemble mean values for each case; (d) spatial distributions of ensemble averaged PPI differences between SENS and CTRL; the black box denotes the ECP region; (e) same as (d) but for PPI differences with concurrence of negative EA; (f) same as (d) but for PPI differences with concurrence of positive EA. In (d), (e), and (f), the black dots indicate the 0.05 significance level.

To elucidate the dynamic processes from the Arctic sea ice forcing to EA phase and PPI changes, we examined the transient eddy variations over the upstream region and quantified their impacts on regional circulation using the potential vorticity (PV) inversion method [100](see Methods for details). We plotted the **E** vectors—the indicators of transient eddy properties and their local interactions with the time-mean flow[109]—and the eddy-induced geopotential height tendency at 250hPa based on the 30 strongest positive EA years (10 maximums for each DJF month) in the reanalysis and the 30-year modeling DJF ensemble differences between SENS and CTRL in Figure 15. The divergence of E over the Atlantic Ocean leads to eddy-induced acceleration of the jet stream as well as negative tendencies in the 250hPa geopotential height field of both reanalysis and simulations (Figure 15a/b). Such negative tendencies result in cyclonic anomalies in the upper troposphere over the Atlantic Ocean and trigger wave train propagation to the downstream regions as shown in the winter averaged wave activity flux (WAF) and anomalous geopotential height fields in both reanalysis and modeling data (Figure 15c/d), which resembles a positive EA pattern (Figure 7). We then used PV inversion to examine the impact of the downstream manifestation of the positive EA pattern on regional circulation over the ECP area. We found significantly weakened winter monsoon in ECP that is attributed to the EA induced circulation anomalies. In contrast to strong

climatological northwesterly winds at 850hPa over Northeast Asia (Figure 16a/b), positive EA related PV anomalies in the middle to upper troposphere induce anomalous southeasterly winds in the lower troposphere over the East China coastal regions in both reanalysis and modeling results (Figure 16c/d), which suppress the air ventilation capability by the northerly monsoon winds and result in severe air stagnation over the ECP area. We also compared the impact of PV anomalies at different levels and found that such ventilation suppression effects in both reanalysis and simulation data are dominated by anomalous PV in the middle to upper troposphere (above 850hPa) rather than that in the lower troposphere (below 850hPa). In contrast to anomalous southeasterly winds induced by the middle to upper level PV anomalies (Figure 16c/d), those PV anomalies in the lower troposphere mainly lead to strong northerly winds with enhanced wind speed and air ventilation over the ECP region (Figure 16e/f). The overall impact of circulation anomalies depends on the counteraction between anomalies in the lower levels and those in the middle to higher levels. In the reanalysis data based on the strongest EA ensembles (Figure 17), the ventilation suppression effect due to middle and upper level circulation anomalies overwhelms the enhancement effect due to lower level anomalies with generally suppressed monsoon winds in total fields, and the sensitivity simulations reproduce such suppression effects in both actual anomalous fields and PV inversion fields but to a less extent (Figure 17). The simulated responses are more comparable to the temporal composite between P2 and P1 of the reanalysis data (Figure 17). All in all, we conclude that the Arctic sea ice decline in the preceding autumn and early winter induces strong transient eddy forcing with cyclonic anomalies in the upper troposphere over the Atlantic Ocean. Such disturbances trigger wave train propagation to the downstream regions with

positive EA-like responses in the upper and middle troposphere. Positive EA related circulation changes finally attenuate the winter monsoon intensity over the East Asia coastal regions and results in severe air stagnation in the ECP area.

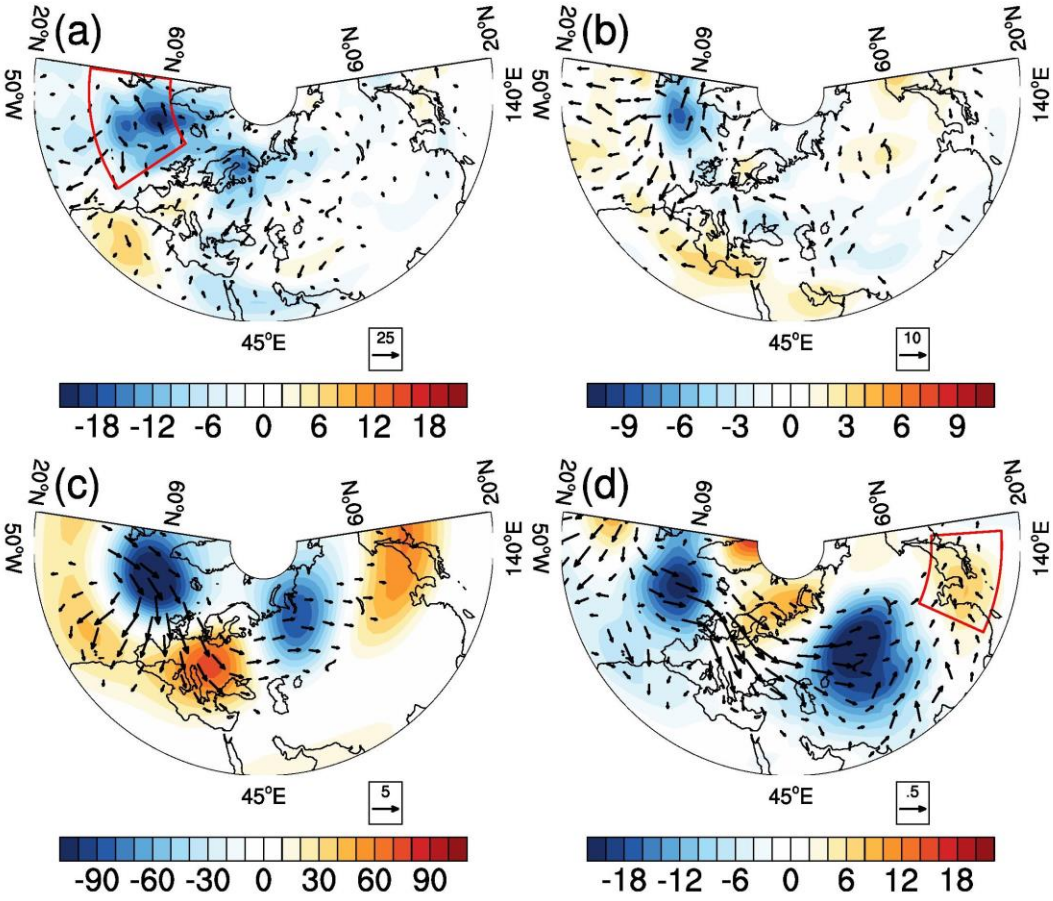

Figure 15 – Comparisons of transient eddy forcing, wave activity flux, and geopotential height anomalies in the NCEP reanalysis data and WACCM simulations in winter (DJF). (a) horizontal components of E (arrows) and geopotential height tendencies (shading) at 250hPa based on the 30 strongest positive EA cases of the reanalysis data; (b) same as (a) but based on the ensemble averaged difference of SENS and CTRL simulations; (c) wave activity flux (arrows) and geopotential height

anomalies (shading) at 250hPa based on the 30 strongest positive EA cases of the reanalysis data; (d) same as (c) but based on the ensemble averaged difference of SENS and CTRL simulations. The red box in (a) denotes the predominant anomalous transient eddy source region. The red box in (d) denotes the region of anomalous fields used for the PV inversion in Figure 16. See main text for details.

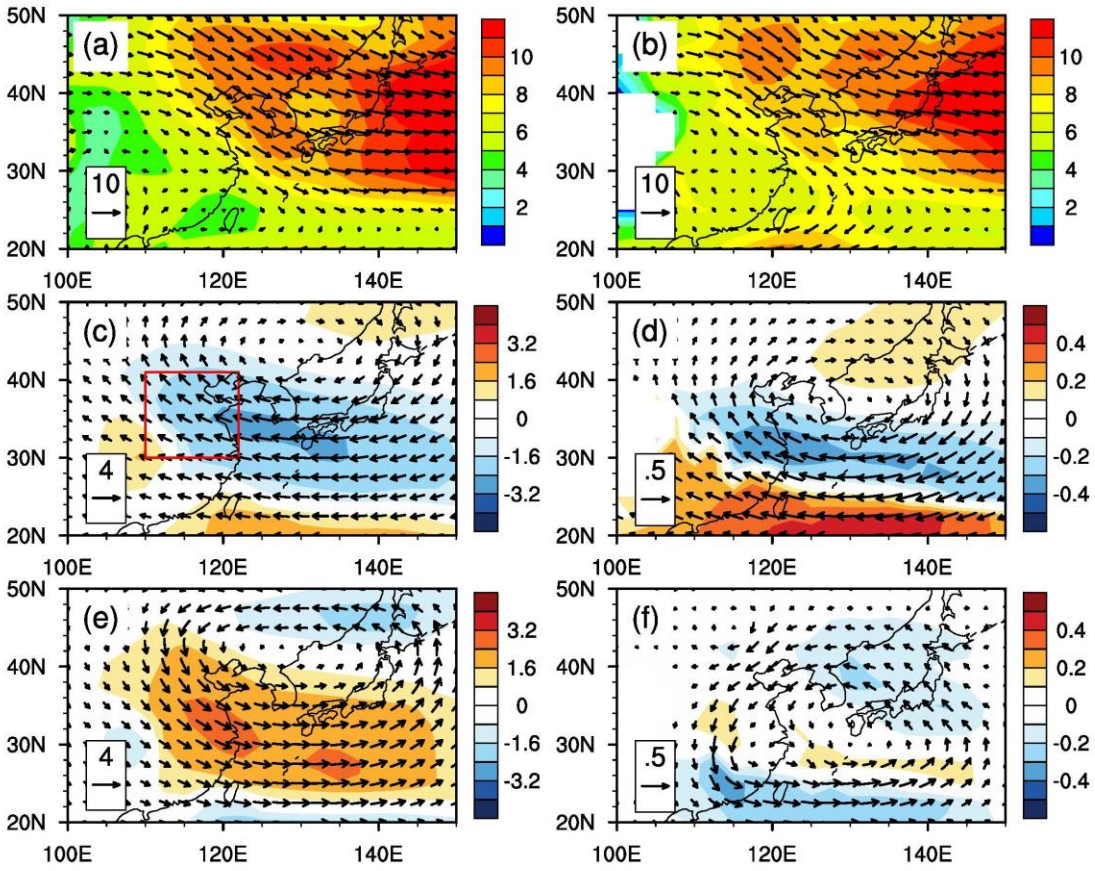

Figure 16 – Comparisons of winter (DJF) circulation over East Asia in the reanalysis data and sensitivity simulations. (a) 30-year (1981-2010) averaged climatological wind vectors (arrows) and wind speed (shading) at 850hPa based on the NCEP reanalysis data; (b) same as (a) but based on the ensemble averaged CTRL simulations; (c) anomalous wind vectors (arrows) and speed (shading) at 850hPa inversed by the

middle to upper troposphere PV anomalies (700-100hPa) over the red box region in Figure 15(d); (d) same as (c) but inversed by the middle to upper troposphere PV anomalies (700-100hPa) of the sensitivity simulations; (e) same as (c) but inversed by the lower troposphere PV anomalies (1000-850hPa) over the red box region in Figure 15(d); (f) same as (e) but inversed by the lower troposphere PV anomalies (1000-850hPa) of the sensitivity simulations. The ECP region is denoted by the red box in (c). The simulation data interpolated below the ground surface over the high-altitude regions are removed in (b), (d), and (f).

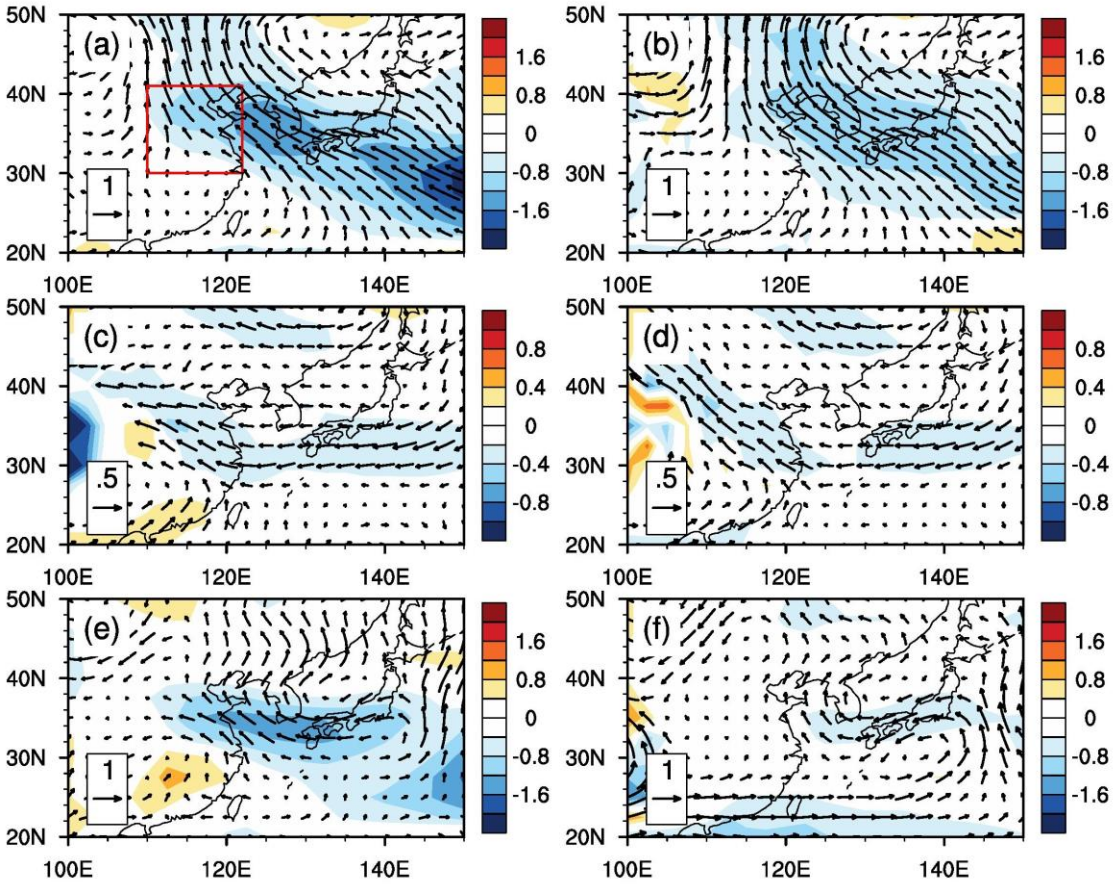

Figure 17 – Comparisons of composite anomalies and PV inversion by all level troposphere (1000-100hPa) anomalies in the reanalysis data and sensitivity simulations. (a) wind vectors (arrows) and speed (shading) anomalies in the 30 strongest DJF EA years of the reanalysis data; (b) same as (a) but based on the PV inversion of all level (1000-100hPa) anomalies of the 30 strongest EA years; (c) same as (a) but based on DJF differences between SENS and CTRL simulations; (d) same as (b) but based on the PV inversion of all level differences between SENS and CTRL; (e) same as (a) but based on the P2 years after 2000 (2000-2016); (f) same as (b) but based on the PV inversion of all level anomalies of the P2 years.

3.2.3 CMIP5 Future Projections

We further examined the CMIP5 RCP8.5 future projections of SIC, EA, and PPI based on 11 climate models (Table 5) to validate such teleconnection relationship on ECP air stagnation extreme events (see Methods for details). Similar with the previous analysis in Figure 14, we separated the whole CMIP5 time series into three periods—P1 from 1980 to 2020, P2 from 2021 to 2060, and P3 from 2061 to 2100—to isolate climate impacts of Arctic sea ice with different forcing intensity (Figure 18a). P1 shows the weakest ice forcing with slowly declining Arctic sea ice concentrations, while P2 shows moderate ice forcing and P3 shows the strongest ice forcing. We first compared the total winter EA responses to the ice forcing by separating all modeling samples into two groups, one with positive ice forcing (SIC+: months with standardized SIC > 0.5 standard deviation) and one with negative ice forcing (SIC-: months with standardized SIC < -0.5 standard deviation). It's clear that EA distributions in the SIC- group shift towards its positive phase comparing to EA in the SIC+ group, especially over the positive tail with the probability of positive extremes increased to 12% with a fold change of 1.4 (Figure 18b). By checking EA responses in different periods, we reconfirmed such positive shifting tendency of EA in P2 and P3, and the shifting magnitude is proportional to the forcing intensity with the probability of positive EA extremes increases to 8% in P2 (a fold change of 0.6; Figure 18c) and 9% in P3 (a fold change of 0.8; Figure 18d). Accordingly, PPI also shows strong positive shifting tendencies given positive EA (EA+: months with standardized EA > 0.5 standard deviation and vice versa in EA-), and such tendencies are significant in both ensemble mean value and probability of positive extremes that increase by 0.40 and 8% (a fold change of 1.6), respectively (Figure 18e). The probability of PPI positive extremes increases to 7% in P2 (a fold change of 0.4) with moderate ice forcing (Figure 18f), while

it increases to 10% in P3 (a fold change of 1.0) with strong ice forcing (Figure 18g). More frequent positive PPI extremes will pose higher risk on regional air quality, but they also provide strong incentives for the Chinese government to implement more stringent emission control policies on both greenhouse gases and aerosol pollutants to avoid the worst scenario into reality.

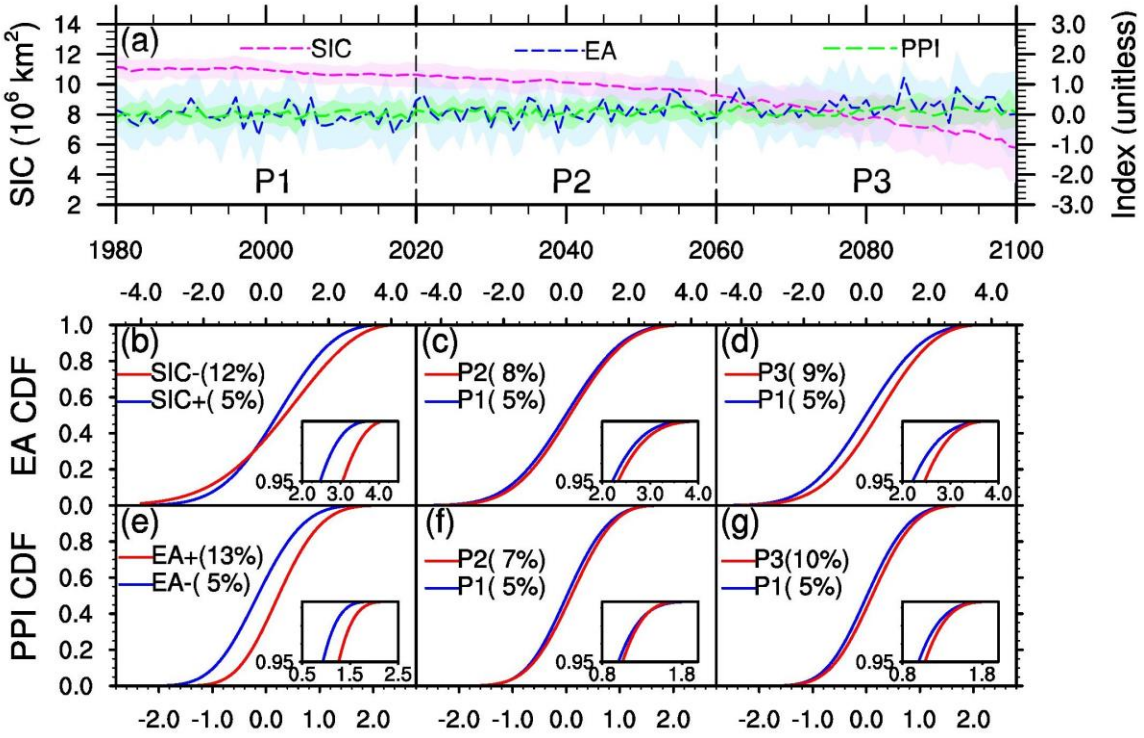

Figure 18 – Historical and future simulations of Arctic sea ice, EA, and PPI indices based on ensemble mean of 11 climate models in CMIP5 historical and RCP8.5 scenarios. (a) time series of ensemble mean SIC, EA, and PPI from 1980 to 2100. Color shadings denote ±1 standard deviation. The three time windows are listed and separated by black dash lines; (b) comparisons of EA CDFs in anomalously positive and negative SIC scenarios; the percentages in parentheses denote the probabilities of positive extremes (≥EA_{SIC+}^{95th}); (c) comparisons of EA CDFs in P1 and P2 periods;

the percentages in parentheses denote the probabilities of positive extremes ($\geq EA_{P1}^{95th}$); (d) same as (c) but for comparisons of P1 and P3; (e) comparisons of PPI CDFs in positive and negative EA cases; the percentages in parentheses denote the probabilities of positive extremes ($\geq PPI_{EA-}^{95th}$); (f) comparisons of PPI CDFs in P1 an P2 periods; the percentages in parentheses denote the probabilities of positive extremes ($\geq PPI_{P1}^{95th}$); (g) same as (f) but for comparisons of P1 and P3. The inlets in (b)-(g) show distributions of positive extremes.

3.3 Conclusions

We conducted series of numerical sensitivity modeling experiments with multiple climate models and analyzed the modeling results based on the CMIP5 models in this chapter. The modeling results corroborated the statistical findings in the previous chapter that boreal cryosphere changes such as declining Arctic sea ice and increasing Eurasian snow would lead to more positive phase of EA in winter and suppress regional air ventilation over the ECP area. The suppressed ventilation finally resulted in severe haze pollution in winter in concurrence with large amounts of anthropogenic emissions over this region. Such teleconnection relationship will keep exacerbating in future with air stagnation extremes increased by 100% by the end of the 21st century according to the CMIP5 RCP8.5 ensemble projections based on the 11 climate models. This climate penalty would simultaneously pose high pressures and strong incentives for the Chinese government to conduct its air quality regulations with more stringent emission controls. The dynamic diagnosis for the teleconnection pattern and climate sensitivity relationship also provides useful tools for operational air quality forecast at medium-range to short-term time scales. A clear understanding of regional air stagnation and its relationship with preceding remote climate forcing would benefit the environmental governance and

emission control practice by the Chinese government to achieve a more practical and sustainable cost-effective solution in routine atmosphere environment management.

CHAPTER 4. DEVELOPMENT OF A REGION-SPECIFIC ECOSYSTEM FEEDBACK FIRE MODEL (RESFIRE) IN THE COMMUNITY EARTH SYSTEM MODEL

4.1 Fire Model Development

In this chapter, we developed a REgion-Specific ecosystem feedback Fire model (RESFire) in the Community Earth System Model (CESM) to extend the fire modelling capability such that the interactions of fire with climate and ecosystems could be simulated and investigated by climate models. The major innovative features in RESFire include: (1) region and ecosystem dependent updates of natural/anthropogenic constraints for fire occurrence and spread; (2) fire emissions in forms of mass (gases and aerosols) and energy (sensible and latent heat) fluxes; (3) incorporation of fire disturbances on ecosystems through vegetation mortality, regrowth, and associated land cover changes; (4) climate model bias corrections to ensure the consistency of online simulation performance under fully coupled model settings with using offline reanalysis and observation data. We also incorporated online plume rise parameterization to better simulate vertical distribution and long-range transport of fire aerosols and their effects on weather and climate. The fire model development was described in the first section. RESFire modeling performance was evaluated using the ILAMB system and other benchmarks in the following section. We drew the conclusions in the last section.

4.1.1 The Community Earth System Model

CESM is a fully-coupled global climate model maintained by the National Centre for Atmospheric Research (NCAR) [89]. It is composed of five major components of the earth system including atmosphere, land surface, ocean, sea ice and land ice, plus one

central coupler component. As the latest release of CESM, CESM version 1.2.2 (CESMv1.2.2) has numerous new key features to improve our modelling capability to understand and predict the climate system. We developed the RESFire model in CESMv1.2.2 with both offline data atmosphere mode and online simulated atmosphere mode at a spatial resolution of 0.9° (lat)×1.25° (lon) and a temporal resolution of 30 minutes. The offline data atmosphere mode was driven by the combination of atmosphere observation and reanalysis data provided by the Climatic Research Unit and National Centres for Environmental Prediction (CRUNCEP) [110], while the online atmosphere mode was driven by the Community Atmospheric Model version 5 (CAM5) [90], the atmosphere component of CESM. RESFire was coupled with the Community Land Model version 4.5 (CLM4.5) [111]—the land component of CESM—in both simulation modes. We also added data interfaces between CLM4.5 and CAM5 to transport fire model inputs and outputs in the online mode. These newly incorporated fire modeling features are compatible with multiple major improvements in both CAM5 and CLM4.5 such as a new 3-mode modal aerosol scheme, a prognostic two-moment cloud formulation, and a revised photosynthesis scheme, etc. [90, 111]. Thereby, RESFire provides the state-of-the-science simulation capability to examine the physical, chemical, and biological processes through which fire interacts with climate and terrestrial ecosystems.

4.1.2 RESFire Model Framework

To account for climate-fire interactive processes comprehensively, we developed three components of RESFire in CESM (Figure 19): fire occurrence estimation, fire spread optimization, and fire impact parameterization. We started from the maximum fire count estimation, which was considered as the maximum fire occurrence potential triggered by

both natural and anthropogenic ignitions. Then we added natural constraints on the maximum fire occurrence potential to estimate fire counts with consideration of fire weather impacts. We further added anthropogenic constraints on fire counts to generate final fire count estimation. The final fire count product in combination with fire spread parameterization was used for burned area estimation at the next step. The maximum fire spread potential for a single fire spot in one grid was estimated by multiplying maximum fire spread rates with average fire duration time under an elliptical fire spread shape assumption [112]. We added natural and anthropogenic constraints successively on the maximum fire spread potential to optimize burned area estimation. The optimized burned area product was used in consequent fire impact parameterizations. In this paper, fire impacts consist of direct mass and energy emissions as well as disturbances on ecosystems, which include fire induced tree mortality and associated recovery processes. Such ecosystem disturbances could further lead to indirect fire impacts on the climate system by perturbing hydrological cycles, radiation budget due to surface albedo changes, and terrestrial ecosystem greenhouse gas budget.

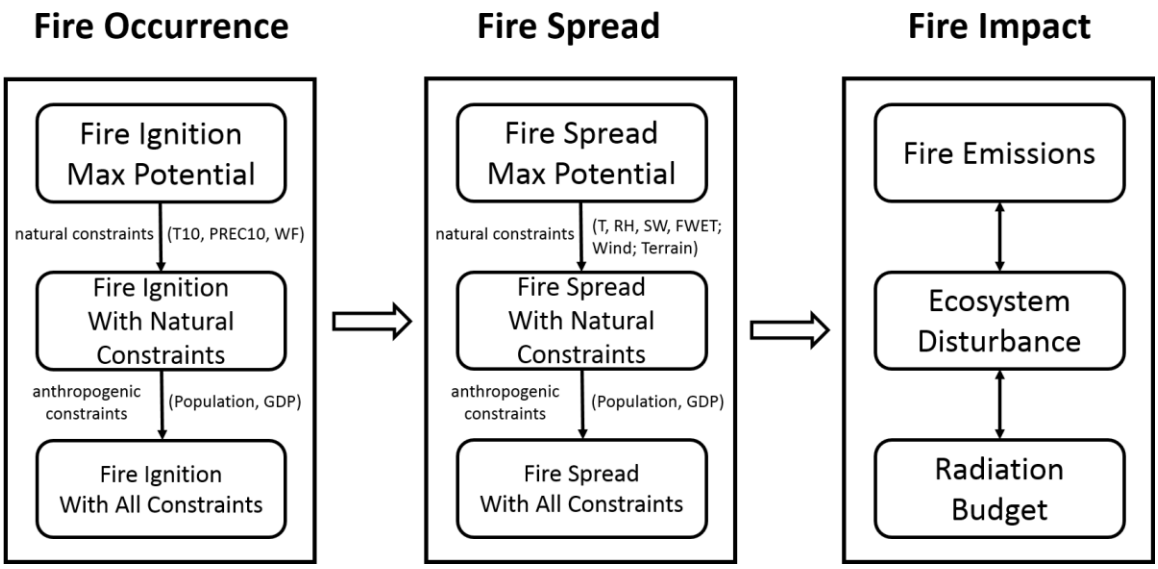

Figure 19 – A schematic diagram of the RESFire model development

To represent the diversified fire sensitivity due to different vegetation characteristics, regional climate and socioeconomic conditions, we divided the global land areas into 8 sub-regions based on combinations of the 14 GFED regions (Figure 20;Table 6) [55] and characterized the Plant Functional Types (PFTs) into 5 major groups (Figure 20; Table 7). We then developed region- and PFT-specific fire parameterizations for biomes in these sub-regions to improve fire modeling capability in the RESFire model. Such region- and PFT-specific parameterizations were used in the three RESFire components (Figure 19) with considerations of refined natural and anthropogenic constraints on fire occurrence and spread as well as various aspects of fire impacts.

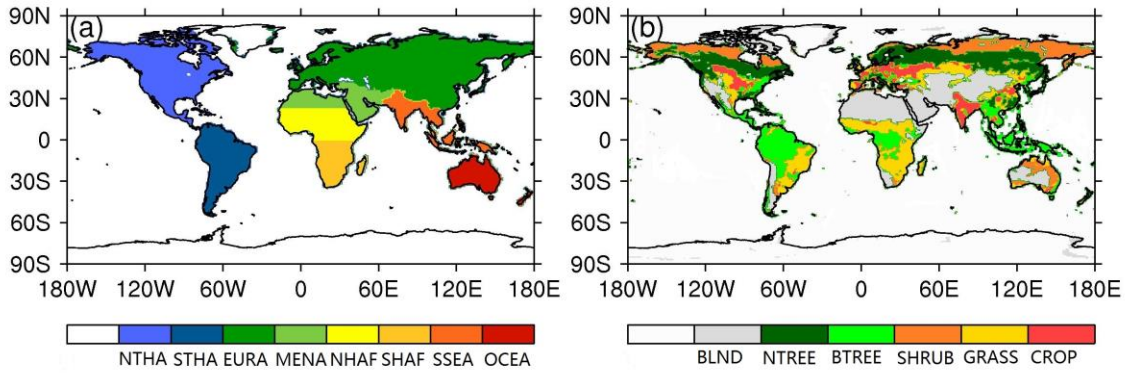

Figure 20 – Geographical regions (a) and predominant PFT groups (b) used by the region- and PFT-specific RESFire model. Each CLM grid has multiple PFT types at sub-grid level. Only predominant PFT types with largest fractions are shown in (b). The acronyms of region and PFT are listed in Tables 1 and 2, respectively.

Table 6 – Regions used in the fire model development

Region	Abbreviation	Full Name
R1	NTHA	North America
R2	STHA	South America
R3	EURA	Eurasia excluding Middle East and South Asia
R4	MENA	Middle East and North Africa
R5	NHAF	Northern Hemisphere Africa
R6	SHAF	Southern Hemisphere Africa
R7	SSEA	South and Southeast Asia
R8	OCEA	Oceania

Table 7 – Plant Functional Type groups used in the fire model development

PFT groups	Abbreviation	Full Name
-	BLND	Bare land
P1	NTREE	Needleleaf tree
P2	BTREE	Broadleaf tree
P3	SHRUB	Shrub
P4	GRASS	Grass
P5	CROP	Crop

4.1.3 Fire Occurrence

Fire can be triggered by either natural or anthropogenic ignitions. The maximum fire ignition potential (N_{clm}^{0}, count/grid/time step) in RESFire is given in Equation 12,

$$N_{clm}^{0} = (I_n + I_a)A_g \tag{12}$$

where I_n and I_a are the number of maximum natural and anthropogenic fire ignitions (count/km^2/time step), respectively. A_g is the grid area (km^2).

The natural fire ignition is a function of the cloud-to-ground fraction of lightning flashes I_l and latitude λ [112, 113] (Equation 13),

$$I_n = \frac{1}{5.16 + 2.16\cos(3\lambda)} I_l \tag{13}$$

and the anthropogenic fire ignition is a function of population density D_p [114, 115] (Equation 14),

$$I_a = \frac{\alpha D_p 6.8 {D_p}^{-0.6}}{n} \quad (14)$$

where $\alpha = 3.89 \times 10^{-3} (count\ person^{-1}\ mon^{-1})$ is the number of potential ignition sources by a person per month, and *n* is the number of time steps in one month.

The fire ignition potential (N_{clm}^0) is considered as the maximum fire spot number estimation without fire weather influences. It does not take account of the diversity of fire related social production and living habits or variable fire management capability among regions with different socioeconomic conditions either. Therefore, we next conducted the observation based regression analysis to incorporate both natural and anthropogenic constraint relationship into the fire model.

4.1.3.1 Natural Constraints on Fire Occurrence

On top of the maximum fire ignition potential, we added region- and PFT-specific natural and anthropogenic constraints successively to capture multiple enhancement and suppression effects on fire activities. The natural constraint factors consist of three fire weather variables: T10, PREC10, and WF (Table 8) [29]. The first two meteorological variables were used by several drought indices to characterize the atmosphere and hydrological drought conditions [116]. We considered these drought-related variables in a continuous time window (10-day running mean) to better represent the probability of fire occurrence as a consequence of cumulative effects in ambient environment and

biomass conditions. The last hydrological variable was used by a previous study [112] to characterize fuel combustibility. For training purposes, we obtained monthly fire weather data from the CLM land model outputs driven by the CRUNCEP observation-reanalysis data. We then used the observation-reanalysis combined weather data and satellite observed fire spot data to train the regression model.

Table 8 – Fire weather factors used as natural constraints on fire occurrence

Fire weather factors	Description	Notes
T10	10-day running mean of 2-m temperature	A meteorological variable to depict drought conditions [116]
PREC10	10-day running mean of total precipitation	A meteorological variable to depict drought conditions [116]
WF	Soil water fraction for top 0.05m layers	A hydrological variable to characterize fuel combustibility [112]

Given the large discrepancies between the maximum fire ignition potential and observed fire counts, we defined a common logarithm-based natural scaling factor for fire counts (NS_n) in Equation 15,

$$\mathrm{NS}_n = log_{10}(N_{modis}/N^0_{clm}) \tag{15}$$

where N_{modis} is the monthly MODIS climate modeling grid (CMG) fire count product (MYD14CMH) on board of the EOS-Aqua platform [117]. It's noted that the MODIS CMG fire products are generated at 0.5° spatial resolution from 1km pixel level active fire products with cloud cover corrections, which provides an approximate estimation for the modeling counterpart of the maximum fire ignition potential if assuming independence of detected fire pixels [118]. We used 4 years of monthly MODIS observational data (2003-2006) to investigate the natural constraint relationship while the

other years of data were used for validation. The inter-annual variability of these 4 years' observations was relatively small so that we reduced the influence of extreme samples in model training.

We examined the region-specific relationship between NS_n and fire weather factors using multi-linear ridge regression models (Equation 16),

$$\mathrm{NS}_n^{i,j} = \sum_{k=1}^{3} \beta_k^{i,j} \cdot X_k \tag{16}$$

where X_k are the three spatial and temporal variable fire weather factors in Table 8 and $\beta_k^{i,j}$ is the corresponding regression coefficient of the k^{th} factor associated with the i^{th} PFT group in the j^{th} sub-region. $\mathrm{NS}_n^{i,j}$ is obtained by filtering out gridded NS_n in the j^{th} sub-region with the fraction of the i^{th} PFT group greater than 30% in the monthly observational data from 2003 to 2006. To separate the temporal and spatial variations in the relationship, we trained the regression models with spatial averaged and temporal averaged data, respectively. Specifically, we first regionally averaged the monthly fire weather factors $X_k(x, y, t)$ and the corresponding $\mathrm{NS}_n^{i,j}(x, y, t)$ in the j^{th} sub-region with gridded observational burned area as averaging weights. We used weighted averaging to highlight major burning areas vulnerable to fire. Therefore, we generated monthly time series of fire weather factors $\bar{X}_k(t)$ and natural scaling factors $\overline{\mathrm{NS}}_n^{i,j}(t)$ for each sub-region, and then estimated the regression coefficients $\bar{\beta}_k^{i,j}$ using ridge regression for temporal variability. Similarly, we regressed annually averaged $\widetilde{\mathrm{NS}}_n^{i,j}(x, y)$ on annual mean weather factors $\tilde{X}_k(x, y)$ (all with monthly burned area as averaging weights) and

estimated the regression coefficients $\tilde{\beta}_k^{i,j}$ using ridge regression for spatial distribution. We applied the average of $\bar{\beta}_k^{i,j}$ and $\tilde{\beta}_k^{i,j}$ in the RESFire model to capture the spatial and temporal variability simultaneously and set the constant terms β_0 as the regional annual mean deviations between observational $\mathrm{NS}_n^{i,j}$ and simulated $\widehat{\mathrm{NS}_n^{i,j}}$ datasets (Equation 17),

$$\widehat{\mathrm{NS}_n^{i,j}} = \sum_{k=1}^{3} \frac{(\bar{\beta}_k^{i,j} + \tilde{\beta}_k^{i,j})}{2} \cdot X_k(x, y, t) + \beta_0 \quad (17)$$

We conducted variable selection first to circumvent collinearity problems in the regression model. If the correlation between two input variables exceeded the threshold, we removed one of them and built the regression model with the rest of input variables. Furthermore, the ridge regression method, which is a penalized regression method, has low sensitivity to collinearity and shows great potential to reduce the negative impact of the collinearity problem in ecological studies [119]. We set a suggested threshold of $|r| > 0.7$ [119] for correlations among the predictor variables in the regression model.

Figure 21 illustrates the temporal variability of fire occurrence in both observation and regression data for each region and PFT group. Since cropland fires are mostly controlled by agricultural activities with strong anthropogenic influences on the seasonality and spatial distributions [120, 121], we parameterized cropland fires separately by focusing on socioeconomic constraints following previous studies [122]. Therefore, we only applied the natural and anthropogenic constraining framework to the PFT groups 1-4 as shown here. Generally, most of regression data reproduce the seasonality in observational data for different PFT groups in each region, which are reflected by relatively high correlations between regression and observation data on the

top of each subplot (for instance, r=0.97 for PFT group 4 in region 5; Figure 21(P4R5)). The Africa regions (R5-6) show the strongest burning seasonality for all PFT groups, with peak fire seasons in cold and dry months in both northern and southern hemispheres of Africa. The temporal variation models capture well these seasonal changes with regression data in good agreement with observation data. The spatial variation models describe the spatially heterogeneous burning distributions in a similar manner, though the spatial predictability (Figure 22) is not as high as for temporal variation due to larger spatial variability in fire occurrence.

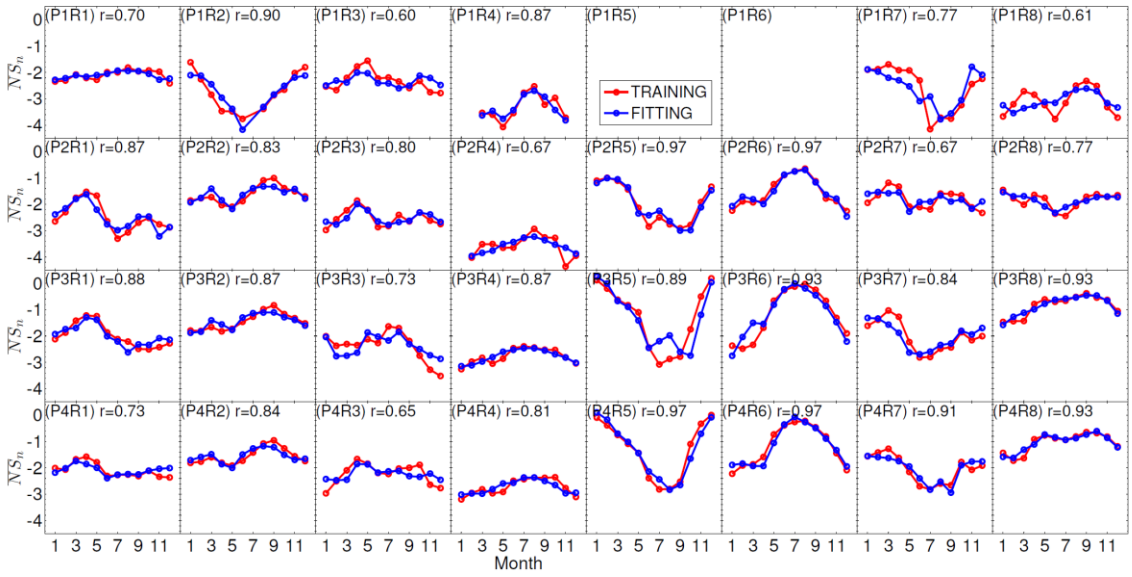

Figure 21 – Region- and PFT-specific natural constraints on temporal variation of fire occurrence. See Table 6 and Table 7 for the full names of region and PFT numbers shown on the top left corners. The correlation coefficient between observation and regression data for each PFT group and region is shown.

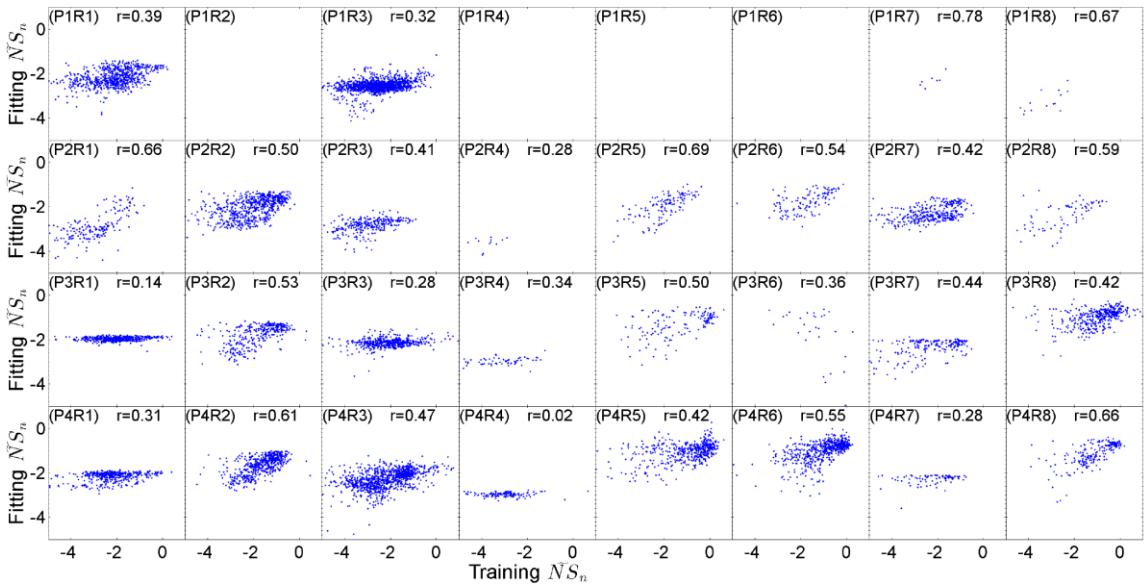

Figure 22 – Region- and PFT-specific natural constraints on spatial variations of fire occurrence.

4.1.3.2 Anthropogenic Constraints on Fire Occurrence

We defined a demographic scaling factor for fire count (AS_n) in the same manner of NS_n after including natural constraints:

$$AS_n = log_{10}(N_{modis}/N'_{clm}) \quad (18)$$

where N'_{clm} is the fire count estimation with consideration of natural constraints NC_n:

$$N'_{clm} = N^0_{clm} \times NC_n \quad (19)$$

The natural constraint NC_n in the j^{th} sub-region is a weighted average of exponents of scaling factors NS_n for the i^{th} PFT group with the weight of its fractional coverage f^i:

$$NC_n = \sum_{i=1}^{n} (10^{\mathrm{NS}_n^{i,j}} \times f^i) \tag{20}$$

Given high noises with large uncertainties in the raw data, we followed the method of *Li et al.* [122] and resampled the data by averaging AS_n in 50 consecutive bins of population density in the log scale, and then generated linear and nonlinear weighted fitting functions by setting sampling sizes as weights for the resampled data in each bin. We obtained anthropogenic constraints for the 4 PFT groups in the 8 sub-regions based on these weighted fitting functions between population and anthropogenic scaling factors (Figure 23). The anthropogenic constraint relationship differs among different PFT groups and regions. For instance, Eurasia (R3) as the most populated region generally shows strong human suppression effects for most PFT groups because of effective early detection and prevention of fire danger. On the contrary, South America (R2) demonstrates predominant enhancement effects for many PFT groups, especially in less populated regions, which could be related with deforestation burning activities over this region. In North America (R1), distinctions between prescribed burning in the southeast

U.S. and large wildfires in the west U.S. lead to more complex relationship with mixed suppression and enhancement effects that are nonlinear for many PFT groups.

We estimated anthropogenic constraints AC_n based on anthropogenic scaling factors and PFT fractional coverages in the same way like natural constraints NC_n,

$$AC_n = \sum_{i=1}^{n} (10^{\mathrm{AS}_n^{i,j}} \times f^i) \tag{21}$$

where $\mathrm{AS}_n^{i,j} = f(population)$ is a fitting function of population density as shown in Figure 23.

After taking account of both natural constraints NC_n and anthropogenic constraints AC_n, we estimated the final fire count estimation N_{clm}^{f} in Equation 22,

$$N_{clm}^{f} = N'_{clm} \times AC_n = N_{clm}^{0} \times NC_n \times AC_n \tag{22}$$

This final fire count estimation is the basis for burned area and fire impact parameterizations in the following sections.

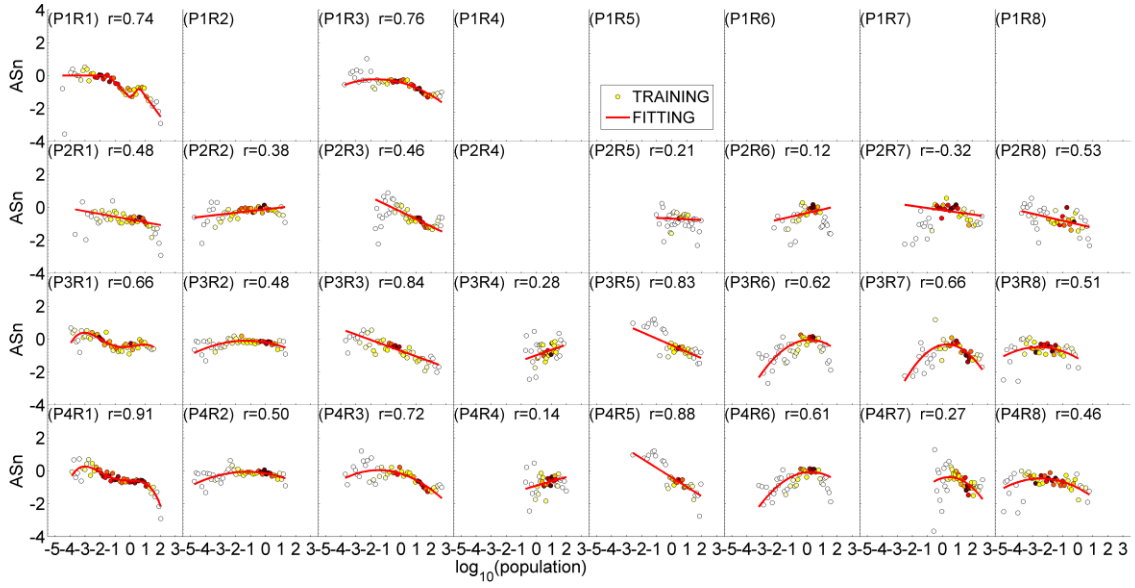

Figure 23 – Same as Figure 21 but for the anthropogenic constraints on spatial variation of fire occurrence. the color shading denotes sampling density in each bin of population density. See detailed explanation in the main text.

4.1.4 Fire Spread

To simulate burned area in the fire model, we need to estimate fire spread in addition to fire occurrence. We generated the gridded maximum burned area potential (BA^0_{clm}) as a function of fire count (N^f_{clm}) and maximum spread area per fire spot (A_{max}):

$$BA^0_{clm} = N^f_{clm} \times A_{max} \tag{23}$$

The maximum spread area per fire spot (A_{max}) was parameterized under the assumption of an elliptical spreading shape [112] and passive suppression due to terrain

impedance and landscape fragmentation [123]. Specifically, the elliptical fire spreading area A_{max}^{ellip} is a function of PFT-dependent maximum fire spread rates (fsr_{max}, m/s), average fire duration time (τ), length-to-breath ratio ($L_B = 1.0 + 10.0[1 - \exp(-0.06W)]$, where W is wind speed, m/s), and head-to-back ratio of the theoretical elliptical fire shape ($H_B = \frac{L_B + \left({L_B}^2 - 1\right)^{0.5}}{L_B - \left({L_B}^2 - 1\right)^{0.5}}$) in Equation 24 adopted from *Li et al.*[112]:

$$A_{max}^{ellip} = \frac{\pi \times \left(fsr_{max} \times \frac{0.1 L_B}{1 + \frac{1}{H_B}} \right)^2 \times \tau^2}{4 \times L_B} \left(1 + \frac{1}{H_B}\right)^2 \times 10^{-6} \quad (24)$$

The passive fire suppression due to terrain impedance was adopted from *Pfeiffer et al.* [123], which describes the scarcity of larger fires in mountain regions. The terrain impedance factor (slf) was determined in Equation 25 as a piecewise function of median terrain slope angle γ, which limits the impedance effect only in grid cells with median slope angles larger than 1.7°. We calculated the gridded median slope angle γ following the *Zhang et al.* [124]'s method to aggregate the maximum D8 slope at 1 arc minute resolution based on the ETOPO1 global digital elevation model [125] in Equation 25:

$$slf = \begin{cases} 1 & \gamma < 1.7^{\circ} \\ \dfrac{1}{\frac{5}{9}\pi\gamma - 2} & \gamma \geq 1.7^{\circ} \end{cases} \quad (25)$$

Similarly, we adopted the landscape fragmentation suppression factor (A_{max}^{frag}) from *Pfeiffer et al.* [123] in Equation 26,

$$A_{max}^{frag} = (1.003 + e^{(16.607-41.503f^{non-crop})})^{-2.169} \quad (26)$$

which is approximated as a function of non-crop PFT fractions in grid cells ($f^{non-crop}$) based on the Monte Carlo simulation results.

Such fragmentation suppression factors are the average contiguous area fractions of natural PFT patches in each grid, which set the upper limit of burned area of individual fire spots in Equation 27,

$$A_{max} = \min(A_{max}^{frag}, slf \times A_{max}^{ellip}) \quad (27)$$

We then defined a logarithm-based natural scaling factor for fire spread (NS_a) based on the ratio of GFED burned area products and simulated maximum burned area potential in Equation 28,

$$\mathrm{NS}_a = log_{10}(BA_{GFED}/BA_{clm}^0) \quad (28)$$

where BA_{GFED} is the GFED4.1s burned area dataset with contributions from small fires [53, 55, 126].

4.1.4.1 Natural Constraints on Fire Spread

In burning events, fire spread is constrained mostly by wind and fuel combustibility, the latter of which is a function of moisture content of fuel bed. Since we

already encapsulated the wind factor in the elliptical fire spreading area (A_{max}^{ellip}), here we used surface air temperature (T), relative humidity (RH), surface soil wetness (SW), and the fraction of wet canopy (FWET) as surrogates to characterize fuel combustibility (Table 9). T and RH determine the transfer of water vapor into and out of fine fuel and control the short-term fuel moisture content, while SW and FWET derived from the amount of rainfall affect fire behavior by modulating the fuel moisture content at both short (hourly) and long (seasonal) time scales.

Table 9 – Fire weather factors used as natural constraints on fire spread

Fire weather factors	Description	Notes
TBOT	Surface air temperature	A meteorological variable to control the short-term moisture content of fuels
RH	Surface air relative humidity	A meteorological variable to control the short-term moisture content of fuels [*Li et al.,* 2012]
SW	Surface soil wetness factor	A hydrological variable to characterize both the short-term and long-term moisture content of fuels [*Li et al.,* 2012]
FWET	Fraction of wet canopy	A hydrological variable to characterize both the short-term and long-term moisture content of fuels

We applied natural constraints on fire spread calculation as with fire occurrence by conducting ridge regressions of NS_a on the four fire weather factors based on the 2003 to 2006 monthly observational data. We first determine the collinear input variables. We then built two series of regression models for temporal and spatial variations of fire spread based on regional averaged and annual averaged regression data, respectively. Figure 24 shows region- and PFT-specific temporal variations of natural scaling factors in both observation and regression data. Africa regions (R5-6) still have the strongest seasonal variability of

fire spread in all PFT groups. The fire spread seasonal variations in other biomes are less significant but nonnegligible, especially over the regions with strong weather seasonality. It is noted that the fire seasonality could be variable among different PFT groups in the same region, such as the pronounced seasonal shift between peak fire months over the broadleaf forest areas (P2R8) and the grassland areas (P4R8) in Australia. These differences are attributed to different climatic zones and fire regimes of the predominant biome. In Australia, broadleaf trees mostly grow in temperate zones of southeast Australia with the four-season pattern, while grass mostly grows in the tropical areas of northern Australia with the wet and dry climatic pattern just like the southern hemisphere of Africa (R6). These so-called “bushfires” tend to be most common and severe during summer and autumn (December-March) in forest areas because of higher temperatures and drought conditions that are conducive to fire spread, while bushfires in tropical savannas usually occur during the dry season (April-October) when the biomass is fully cured and ready to burn [127].

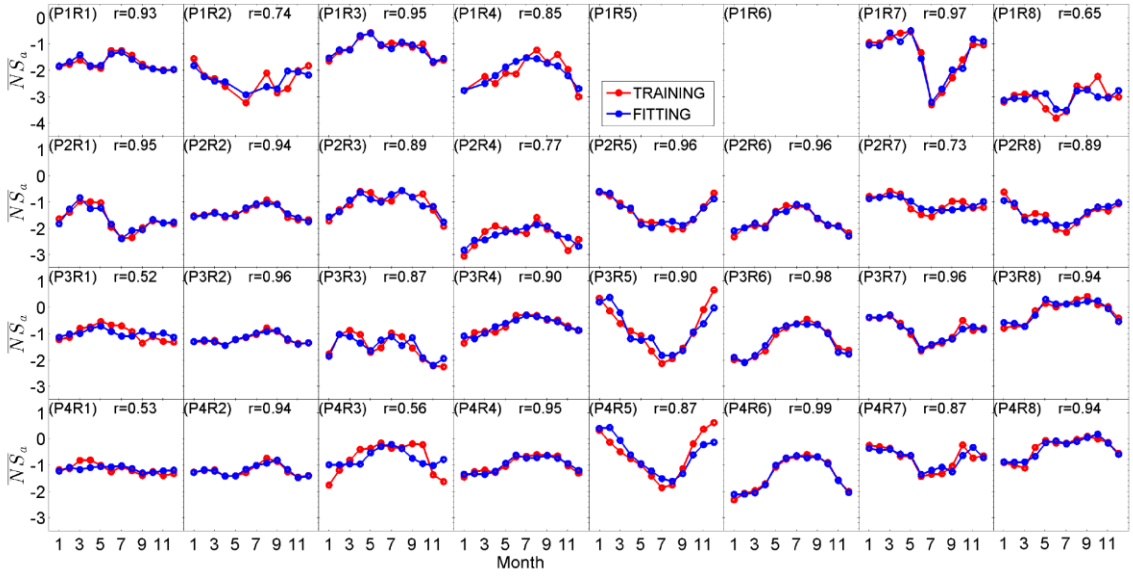

Figure 24 – Same as Figure 21 but for fire spread.

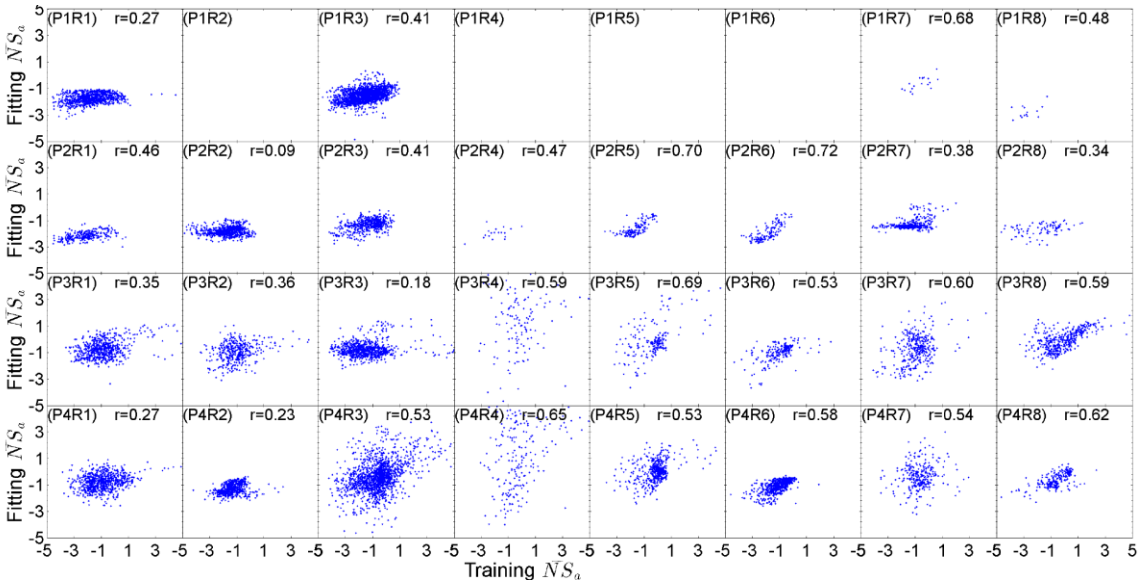

Figure 25 – Region- and PFT-specific natural constraints on spatial variations of fire spread.

Similar with fire occurrence, the regression models are capable to replicate diversified seasonality of fire spread in different biomes. Figure 25 shows the regression

results for spatial variations of natural influences on fire spread, which are significant in biomes such Africa and Australia savannas. Again, we estimated the natural constraint on burned area (NC_a) as weighted averaging of natural scaling factors for each PFT group (Equation 29):

$$NC_a = \sum_{i=1}^{n} (10^{\mathrm{NS}_a^{i,j}} \times f^i) \tag{29}$$

After adding natural constraints on both temporal and spatial variability of fire spread, we next implemented anthropogenic impacts to finalize fire spread optimization.

4.1.4.2 Anthropogenic Constraints on Fire Spread

We defined a logarithm-based demographic scaling factor for fire spread (AS_a) to characterize human impacts on burned area:

$$\mathrm{AS}_a = log_{10}(BA_{GFED}/BA'_{clm}) = log_{10}(\frac{BA_{GFED}}{BA^0_{clm} \times NC_a}) \tag{30}$$

We applied Equation 30 to all regions and PFT groups including cropland areas, where agricultural activities determine burning seasonality and intensity of crop residuals. It is noted that we only considered anthropogenic constraints on cropland fire and set NS_a for cropland fires to zero. NS_a for other PFT fires were described in the previous section. We estimated the anthropogenic scaling factor AS_a in each biome by separately fitting polynomial functions with gridded population density distribution (Figure 26) and Gross Domestic Production (GDP) at country levels. Compared to Figure 23, Eurasia (R3) again shows suppression effects with increasing population density,

though such effect is more significant in grass and cropland regions. South America (R2) preserves moderate fire enhancement effects with increasing population density over rainforest regions (P2) that can be attributed to anthropogenic burning driven by deforestation and agriculture activities in this area. North America (R1) still shows mixed effects with both enhancement and suppression effects in many forest and cropland areas, which might be contributed by concurrence of prescribed burning and fire prevention management.

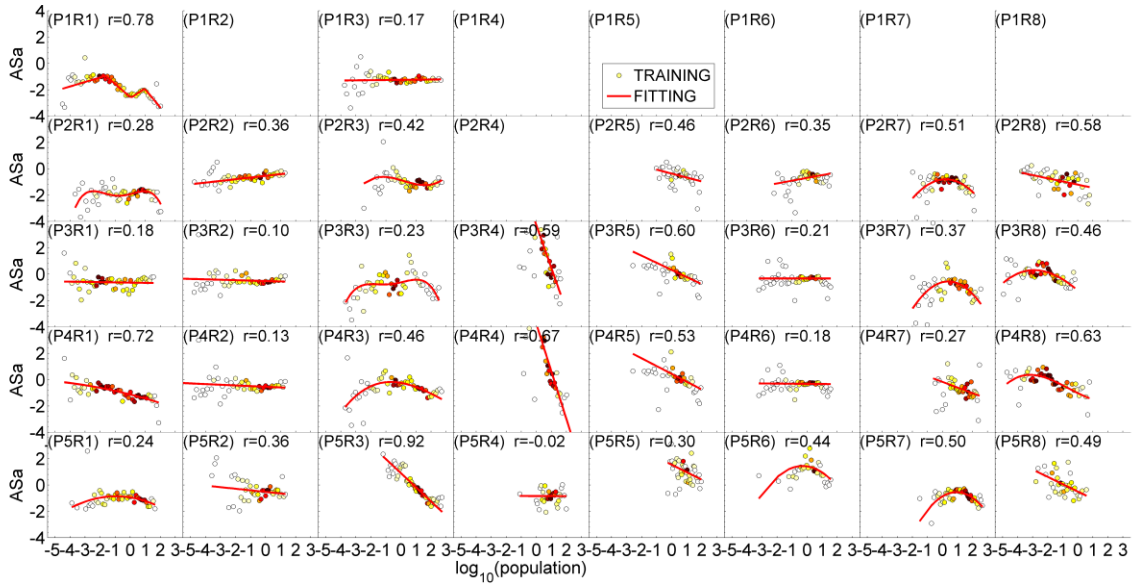

Figure 26 – Same as Figure 23 but for the anthropogenic constraints on spatial variation of fire spread.

With consideration of both natural and anthropogenic constraint effects, we estimated the final burned area BA_{clm}^{f} in Equation 31:

$$BA_{clm}^{f} = BA_{clm}^{0} \times NC_a \times AC_a \tag{31}$$

where AC_a is the anthropogenic constrain on burned area as $AC_a = \sum_{i=1}^{n}(10^{\mathrm{AS}_a^{i,j}} \times f^i)$.

4.1.5 Fire Impacts

We consider two types of fire impacts in the RESFire model: the short-term direct effect and long-term indirect effect. The direct effects include fire emissions in forms of mass and energy fluxes, and the indirect effects include longer term disturbances to ecosystems through post-fire changes in land cover and ecosystem structure due to fire-induced vegetation mortality [128].

4.1.5.1 Fire Emissions

We estimated fire carbon emissions (E_{clm}^{c}, gC/m^2/s) as a combination of carbon storage (C_i, gC/m^2), burned area (BA_{clm}^{f}), and PFT-specific combustion completeness (CC_i):

$$E_{clm}^{c} = \sum_{i=1}^{n} C_i \times BA_{clm}^{f} \times CC_i \tag{32}$$

By multiplying corresponding emission factors [129], we estimated fire emissions for 39 gases and aerosols (E_{clm}^{k}, g species/m^2/s) in Equation 33:

$$E_{clm}^{k} = \frac{E_{clm}^{c}}{cf^{c}} \times EF^{k} \tag{33}$$

where $cf^c = 480$ (gC/kg dry matter) is the carbon to dry matter conversion factor, and EF^k is the k^{th} species' emission factor used by the GFED4.1s data.

To compute the Fire Radiative Power (FRP, W/m^2) estimation, we inversed the conversion factor cf^e used by *Kaiser et al.* [52] to convert fire carbon emissions to sensible heat fluxes:

$$E_{clm}^{frp} = \frac{E_{clm}^{c}}{cf^c \times cf^e} \tag{34}$$

where cf^e is PFT-specific factors ranging from 0.13 to 1.55 $kg\ dry\ matter \cdot MJ^{-1}$ (Table 2 in *Kaiser et al.* [52]). And the fire line intensity (*flint*, kW/m) was parameterized based on released fire energy and fire line length of the ellipse fire shape,

$$flint = \frac{E_{clm}^{frp}}{1000 \times BA_f} \times fsr_{dw} \times \Delta t \times \frac{2 \times L_B}{\left(L_B + \sqrt{{L_B}^2 - 1}\right) \times \left(3 \times (L_B + 1) - \sqrt{3 \times {L_B}^2 + 10 \times L_B + 3}\right)} \tag{35}$$

where fsr_{dw} is the fire spread rate (m/s) at the downwind direction (Equation 36) and Δt is seconds per time step.

$$fsr_{dw} = fsr_{max} \times NC_a \times 0.05 \times \frac{2 \times L_B}{1 + \frac{1}{H_B}} \tag{36}$$

The associated moisture fluxes ($E_{clm}^{H_2O}$, mm H_2O/s) were estimated based on stoichiometry by using Equation 37 adopted from *Jacobson* [130]:

$$E_{clm}^{H_2O} = E_{clm}^{CO_2} \times \frac{M_{H_2O}}{M_{CO_2}} \times \frac{cf^{H_2O}}{\rho^{H_2O}} \tag{37}$$

where $cf^{H_2O} = 0.83 \frac{mol\ H_2O}{mol\ CO_2}$, and $\rho^{H_2O} = 1000\ kg/m^3$.

Finally, we obtained the latent heat flux (E_{clm}^{LH}, W/m^2) by multiplying the moisture flux with latent heat of evaporation (Equation 38):

$$E_{clm}^{LH} = E_{clm}^{H_2O} \times H \tag{38}$$

with $H = 2.501 \times 10^6\ J/kg\ H_2O$.

4.1.5.2 Ecosystem Disturbances

We consider both vegetation mortality and whole-plant mortality in the ecosystem disturbance parameterization. The vegetation mortality simulation is that of the default fire model in CLM [112, 122] (hereafter indicated as LL2013) by transferring a part of unburned plant tissues (leaf, stem, root, etc.) to the litter pool with fixed tissue-mortality factors, while the whole-plant mortality is parameterized by multiplying simulated FRP with observation-based sensitivity relationship between plant mortality rates and FRP. Though plant traits like bark thickness and tree size are also found to influence fire-induced tree mortality [131], such detailed information is unavailable in the CLM model because of its PFT-based modeling structure. We collected multiple fire induced plant mortality rates from field measurements and satellite observations worldwide and

implemented the sensitivity relationship with fire intensity into the fire model. The plant mortality rates are region and PFT dependent to reflect the nature of variable heat endurance capability of plant species to fire scorching, which could remedy the missing plant trait information in the model to some extent. The newly incorporated whole-plant fire mortality and associated land cover changes are essential in climate-fire-ecosystem feedbacks revealed by previous studies [132].

Table 10 lists the fire induced mortality rates (MR, 100%/year/grid) for each PFT except grass and crops. Usually grassland would recover in a relatively short time period after burning due to reduced self-shading and competitive pressure[133], and previous studies indicated positive feedback processes in the grass-fire cycle over many transitional forest edge and savanna regions [134-136]. For cropland, it is mainly managed by agricultural practices instead of natural ecological succession. Therefore, we assume less fire induced perturbation in these two PFT groups. For shrubs, we used the fixed whole plant mortality of 30% once FRP exceeded a threshold value based on the averaged literature data [137-139]. For broad leaf trees, the fire induced whole plant mortality was estimated as a linear function of fire line intensity (*flint*, W/m) based on field measurements [38, 131, 140]. For needleleaf trees in boreal regions, the fire induced tree mortality was parameterized by region-specific nonlinear functions of FRP based on satellite observed sensitivity relationship [62].

Table 10 – Fire induced whole-plant mortality rates for each PFT group

PFT	Mortality Rates	Equations
Shrub	Fixed	$MR = 30\%, \quad \text{if } flint \geq 50\ W/m$
Broadleaf tree	*f*(*flint*)	$MR = 0.000885 \times flint$
Needleleaf tree	*f*(*FRP*)	$MR = \begin{cases} 0.0444 \times \log10(FRP) + 0.64, FRP > 0, North\ America \\ 0.0783 \times \log10(FRP) + 0.26, FRP > 0, Eurasia \end{cases}$

We illustrate the sensitivity relationship between fire induced tree mortality and FRP over the two boreal continental regions in Figure 27. Previous studies showed that boreal Eurasian forest fires are less intense than that in North America [141], and different fire dynamics and plant traits would have significant impacts on tree survival in those regions [62]. These regional characteristics of fire intensity and burn severity are present in satellite measurements [142]. Therefore, we used satellite observed FRP and tree mortality data in post-fire boreal forest regions and fitted a nonlinear function for each biome based on the medians of statistically resampled data (Figure 27). By implementing region specific relationship, the RESFire model could capture these regional differences and capture the effects of fire disturbances on the ecosystem structure and vegetation population. Considering that actual tree death is not an instantaneous event, we deposited the fire induced tree morality into a mortality potential pool (MP, 100%/grid) and then withdrew a fraction of it at a specified fire mortality rate (*fmr*, 100%/second/grid) per time step (Equation 39),

$$\frac{dMP}{dt} = \frac{\sum_{i=1}^{3} MR^i \times BA_f \times f^i}{\Delta t} - fmr = \frac{\sum_{i=1}^{3} MR^i \times BA_f \times f^i}{\Delta t} - \frac{MP}{tsc} \qquad (39)$$

where Δt is seconds per time step, and *fmr* is the instantaneous whole plant mortality rate due to fire estimated by the contemporary mortality potential pool MP over a temporal scaling constant *tsc* as seconds per year.

The whole mortality potential pool would almost run out within the following two to three years if no new mortality potential being added after burning. For those fractional tree/shrub patches that were burned to death, we deducted the mortality fraction at the grid level from the original PFT fraction value and added the same deducted fraction to grassland if it exists in the same grid, or bare land if no grassland exists in the grid. In this way, we are capable to simulate simplified land cover changes with fire induced dynamic vegetation variations in the RESFire model. Such variable PFTs with accordingly updated optical properties would influence surface albedo estimation in the land model and other PFT-related ecosystem structure and function, and further trigger series of radiation, biogeochemical, and hydrological feedbacks after fire burning.

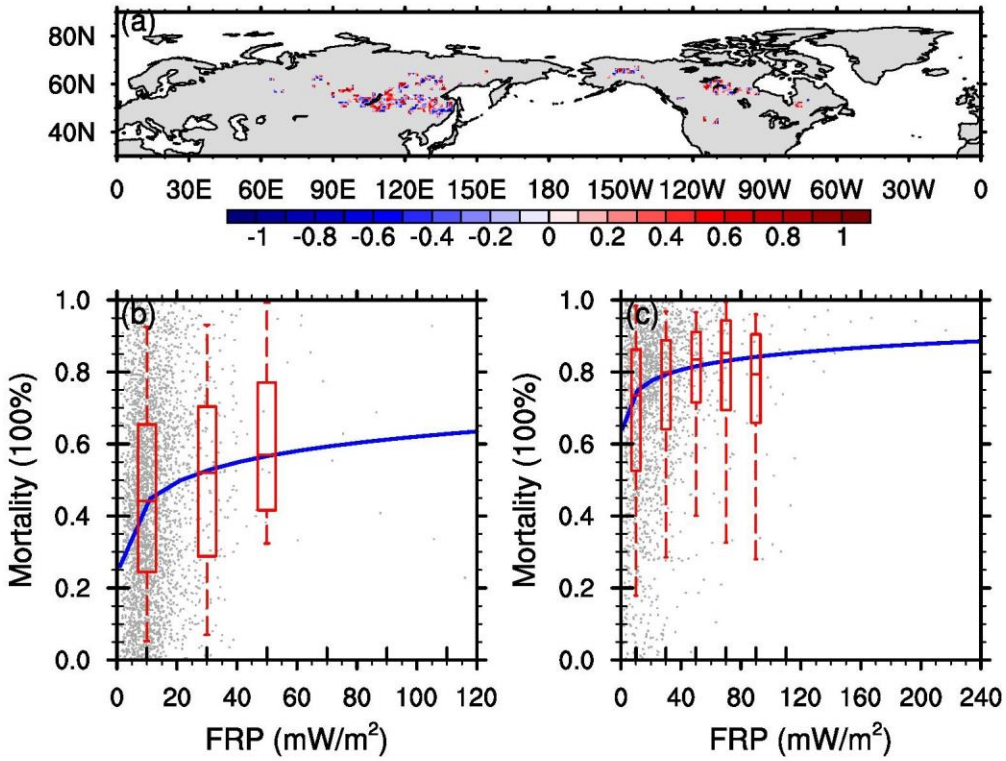

Figure 27 – Relations between FRP and boreal tree mortality. (a) The spatial distribution of correlation coefficients between satellite observed FRP and tree mortality; (b) raw gridded data (grey dots), statistical samples (red boxes) and fitted sensitivity relationship (blue line) of FRP and tree mortality over boreal Eurasia; (c) same as (b) but over boreal North America.

Besides mortality, we also considered post-fire recovery processes over burned regions. Previous studies suggested that the post-fire recovery is mostly a self-replacement process in many burned regions [137, 143]. We only considered stand-replacing processes without interspecific competitions during secondary succession and post-fire recovery in RESFire. We collected and averaged the PFT-specific annual recovery rates (RR,

100%/year/grid) from several in-situ and satellite based observations for secondary succession in Table 11.

Epting and Verbyla [137] found that sever burning speeds up vegetation recovery due to reduced competition pressure in the post-fire environment. To incorporate such a positive feedback mechanism, we adjusted the natural PFT fraction recovery rate (*frr*, 100%/second/grid) according to the contemporary tree mortality fractions (MF, 100%/grid), which is a surrogate of burn severity (Equation 40),

$$frr = 10 \times MF \times \frac{RR}{tsc} \tag{40}$$

We applied these adjusted PFT-specific recovery rates in combination with the estimated mortality rate to allow burned ecosystem to regrow back. Since we do not consider complete vegetation dynamics here, the gridded PFT fractions can only decrease by fire induced mortality, and then restore back to default pre-fire levels at a full recovery if there is no further fire disturbance. The instantaneous change in PFT fractions (*dfr*, 100%/second/grid) at the grid level is a function of fire induced plant mortality reduction and post-fire recovery (Equation 41),

$$dfr = -\frac{dMF}{dt} = frr - fmr \tag{41}$$

Table 11 – Post-fire recovery rates for each PFT group

PFT	Recovery Rates	References
Shrub	10%/year/grid	*Rydgren et al.* [144]
Broadleaf tree (tropical regions)	5%/year/grid	*Chazdon* [145]; *Finegan* [146]; *Guariguata and Ostertag* [147]
Broadleaf tree (boreal regions)	8%/year/grid	*Beck and Goetz* [148]; *Epting and Verbyl* [137]
Needleleaf tree	15%/year/grid	*Epting and Verbyla* [137]; *Goetz et al.* [149]; *Jin et al.`* [143]

4.1.6 Weather/Climate Modelling Bias Corrections

The fire modeling performance depends strongly on the quality of fire weather variables. When CAM5 simulation results were used in the fire model, model meteorological biases lead to significant biases in burned area estimates`. These model biases, especially precipitation related hydrological biases, are common in the current generation of climate models [150]. To reduce the negative impacts from climate model biases, we introduced bias corrections in the online fire mode on the basis of a statistical distribution mapping method [151, 152]. In general, we first evaluated the online CAM5 modeling performance of gridded fire weather variables (Table 8 and Table 9) against the offline counterparts based on the CRUNCEP data of the training period (2003-2006). For grids cells with significant modeling biases, we then obtained the cumulative distribution function (CDF) of the offline daily value based on the observation-reanalysis combined data and the online daily value driven by the CAM5 model. We fitted linear mapping functions based on the two sets of distribution in each biased grid cell. Lastly, we used the mapping function to project the CAM5 fire weather variables onto the corresponding values at the same quantile in the reanalysis data (Figure 28). In this way, we reduced the

climatology mean biases of CAM5 model simulations while keeping the variability simulated by the model. We transformed the precipitation data in a logarithm scale before fitting mapping functions since precipitation intensity spectra usually follow the exponential distribution [151].

Figure 28 demonstrates examples of online bias corrections for simulated surface temperature and precipitation data, in which we find significantly cool and wet biases over most African regions as well as biased drought conditions over South American rainforest and savanna regions in CAM5 results (Figure 28a/b). The CDFs in Figure 28c/d corroborate such bias tendencies across all quantiles of CAM5 simulated surface temperature and 10-day running mean precipitation in a selected grid cell of South America. We then used the mapping functions shown in Figure 28e/f to project the CAM5 simulations onto the reanalysis data such that the online weather biases were reduced. In the next section, we further evaluate the effectiveness of fire weather bias

corrections on fire regime simulations by comparing both raw and bias corrected fire model products with benchmarks.

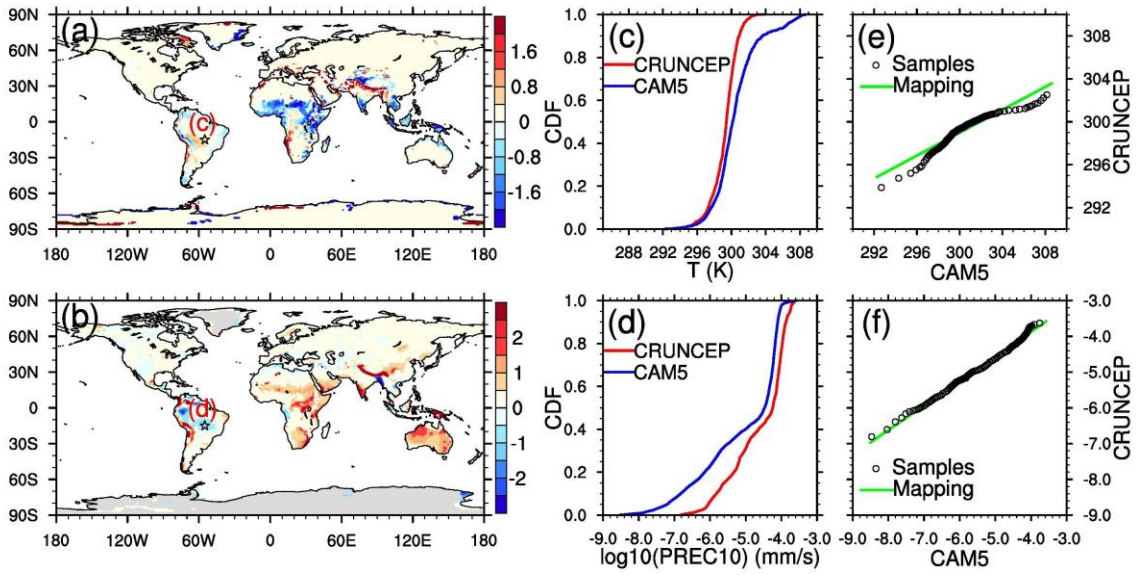

Figure 28 – Online fire weather biases and corrections using the distribution mapping method. (a) Spatial distributions of online biases in surface temperature (unit: K); only biases at the 0.05 significance level are shown. (b) same as (a) but for 10-day running mean precipitation biases (unit: 10^{-5} mm/s). (c) CDF of daily surface temperature in a sample grid cell from CRUNCEP and CAM5; (d) same as (c) but for 10-day running mean precipitation in the same sample grid cell. (e) samples of daily surface temperature in the sample grid cell from CRUNCEP and CAM5 (circles) and the corresponding mapping function (green line); (f) same as (e) but for logarithmic 10-day running mean precipitation.

4.2 Fire Simulation and Evaluation

We conducted 3 sets of fire simulations using RESFire with both CRUNCEP data atmosphere forcing and CAM5 simulated atmosphere forcing. The first simulation set (RESFire_CRUNCEP) was driven by the 1997-2010 CRUNCEP observation-reanalysis combined atmospheric data including global 6-hourly surface temperature, wind speed, specific humidity, air pressure, precipitation and surface downward solar radiation [110] with a steady state in initial spun-up files after several hundred years' simulation. The second simulation set (RESFire_CAM5nc) was coupled with the active CAM5 atmosphere model without fire weather bias corrections and run for 10 years from the same initial conditions. The third simulation set (RESFire_CAM5c) was branched by coupling with bias-corrected CAM5 atmosphere model and running for 10 years. All three sets used the same prescribed climatological cloud-to-ground lightning data, population density, nitrogen and aerosol deposition, and land cover data at the 2000 year values. The cyclical 3-hourly lightning data was interpolated from the NASA LIS/OTD grid product v2.2 2-hourly climatological lightning data with the cloud-to-ground lightning fractions calculated based on *Prentice* and *Mackerras* [113]. The population density data was derived from the Gridded Population of the World version 3 (GPWv3) [153]. The semi-static land use and land cover change data was based on version 1 of the Land-Use History A product (LUHa.v1) at the 2000 values [154] except fire induced PFT disturbances in RESFire. The monthly nitrogen and aerosol deposition data were based on simulations with the CESM atmospheric chemistry and transport model and provided with CESMv1.2 [89]. All these modeling settings are similar with previous CLM4.5-fire simulation studies [112, 122, 128].

Afire fire simulations, we used the International Land Model Benchmarking (ILAMB) system [155] to evaluate the RESFire modeling results associated with fire behavior and impacts. The ILAMB system is an integrated land model benchmarking system designed to improve the performance of land models and to reduce key uncertainties in land surface processes. As one of the major uncertainty sources in land models, fire simulation has considerable influences on the modeling of biogeochemical, biophysical, and hydrological processes. We evaluated the RESFire results in the context of burned area, fire emissions, and ecosystem disturbances to provide a comprehensive evaluation of fire modeling performance. Table 12 lists the benchmark metrics and their references.

Table 12 – Fire model benchmark metrics and references

Category	Variable	Dataset	Source
Intensity	Burned area	GFED4.1s	ftp://fuoco.geog.umd.edu *Giglio et al.* [126]; *Randerson et al.* [53]
	Emissions	GFED4.1s	ftp://fuoco.geog.umd.edu *Giglio et al.* [126]; *Randerson et al.* [53]; *van der Werf et al.* [55]
	FRP	MODIS active fire products	ftp://fuoco.geog.umd.edu *Giglio et al.* [117]
Impacts	Plant mortality	Satellite data	*Rogers et al.* [62]
	Ecosystem resilience	*In-situ* data	*Goulden et al.* [156]

4.2.1 Burned Area

We examined both spatial distributions and seasonal variations of global and regional burned area data in offline and online modes in Figure 29. In general, the spatial distribution of burned area simulations agrees well with the GFED4.1s dataset (Figure

29a) with spatial correlation coefficients of 0.68~0.75 in coupled and uncoupled modes, which are comparable with the LL2013 uncoupled fire model performance (r=0.71) [128]. The offline modeling results driven by the CRUNCEP atmosphere data (Figure 29c, RESFire_CRUNCEP) outperform the online results driven by CAM5 weather inputs (Figure 29e, RESFire_CAM5c with bias corrections; Figure 29g, RESFire_CAM5nc without bias corrections); after bias corrections in fire weather (RESFire_CAM5c), the online results show considerable improvements in all seasons over most regions, especially over Africa and South America. For instance, the high bias in surface temperature and low bias in precipitation over the central South America region result in an unrealistic drought environment in the CAM5 simulation, which leads to a high bias in burned area estimates. The bias correction module in RESFire reduces biases in CAM5 fire weather factors and improves the fire modeling performance with reduced deviation from the benchmark over this region. The seasonal variation estimates are also

significantly better in offline (Figure 29d) and online bias corrected products (Figure 29f) than raw online results (Figure 29h).

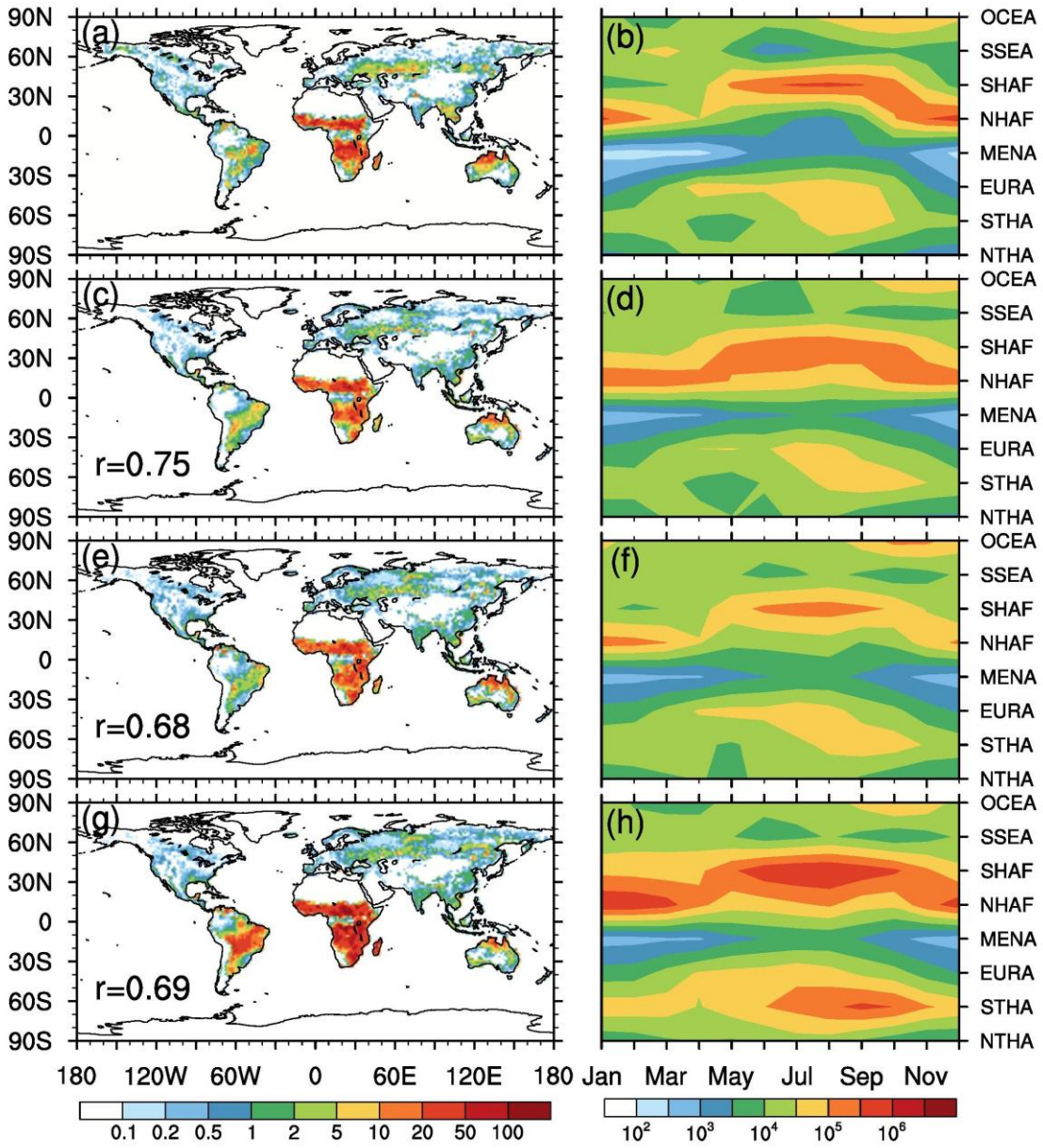

Figure 29 – Comparisons of spatial distributions and seasonal variations of burned area in the observations and simulations. (a) GFED4.1s burned area fractions (%) averaged from 1997 to 2010; (b) seasonal variations of averaged GFED4.1s burned

area (km^2) in the 8 sub-regions; (c)-(d) same as (a)-(b) but from RESFire_CRUNCEP; (e)-(f) same as (a)-(b) but from RESFire_CAM5c; (g)-(h) same as (a)-(b) but from RESFire_CAM5nc. The spatial correlation coefficients between simulated burned areas and GFED4.1s data are shown on the bottom left corners of (c), (e), (g).

To provide a more quantitative understanding of modeling performance, we applied the ILAMB system to the RESFire results from different modes and quantified burned area modeling scores using multiple metrics, which include absolute and relative biases, seasonal phase, interannual variability, RMSE, and Taylor score in Table 13. For comparison, we also listed the evaluation results of the default CLM LL2013 fire scheme driven by the same data atmosphere forcing named as CLM45bgc_CRUNCEP. It's noted that the default CLM LL2013 fire model was calibrated using different atmospheric reanalysis data [157] with an old version of the GFED dataset (GFED3) as benchmarks [54, 158], and the simulation period was also different from this work (1997-2004 in *Li et al.* [128] vs. 1997-2010 here). Though *Li and Lawrence* [159] recalibrated the LL2013 fire model in CLM recently, the updated CLM-fire model is not available until the release of the new version of CESM. Therefore, our CLM45bgc_CRUNCEP run is based on the same version of LL2013 without recalibration and its burned area result (316Mha/yr) is very close to the published one (322Mha/yr) in *Li et al.* [128], which suggests the equivalence of our CLM45bgc_CRUNCEP simulations with the previous published ones [122, 128]. As shown in the table, the burned area simulations from the RESFire model in both offline and online modes outperform the default fire scheme in most benchmarking metrics, such as absolute and relative annual mean biases and phase variations. The smaller spatial and temporal biases and higher scores in the RESFire results corroborate the previous

comparisons in Figure 29. By comparing the evaluation results between online modeling results with (RESFire_CAM5c) and without bias corrections (RESFire_CAM5nc), we also find significant improvements in all benchmarking metrics after implementing fire weather bias corrections. In general, the overall modeling score increased from 0.50 of CLM45bgc_CRUNCEP to 0.61 of RESFire_CRUNCEP and 0.60 of RESFire_CAM5c, respectively. These results illustrate the improved modeling capability of the RESFire model driven by either offline reanalysis or online simulation data, which is necessary for both fire hindcast or future projection studies.

Table 13 – ILAMB evaluation results for burned area estimates

Annual Mean	Units	GFED4s	CLM45bgc _CRUNCEP	RESFire _CRUNCEP	RESFire _CAM5c	RESFire _CAM5nc
Annual Mean	Mha/yr	485.49	315.66	427.66	471.77	1033.62
Bias	Mha/yr	–	-169.84	-57.83	-13.72	548.13
Relative Bias	100%	–	-0.35	-0.12	-0.03	1.13
RMSE	Mha/mon	–	87.19	77.84	82.95	126.52
Phase	months	–	1.35	0.34	0.55	0.58
Global Bias Score	–	–	0.50	0.59	0.57	0.53
RMSE Score	–	–	0.42	0.45	0.45	0.39
Phase Score	–	–	0.75	0.80	0.82	0.82
Taylor Score	–	–	0.36	0.81	0.78	0.56
Interannual Score	–	–	0.55	0.55	0.55	0.52
Overall Score	–	–	0.50	0.61	0.60	0.53

4.2.2 Fire Emissions

We evaluated the interannual variability of fire mass emissions and compared both online and offline annual mean carbon emissions with the GFED4.1s data over each sub-

region (Figure 30). Similar with the burned area estimates, the RESFire_CRUNCEP fire carbon emission also agree well with the benchmark data, which showed two major fluctuation periods around 2000 and 2008 with a temporal correlation of 0.80. It is worth noting that we only trained the RESFire model with the four-year data from 2003 to 2006, which show less interannual variation than the other years. The successful reconstruction of large variations in the other years demonstrated the effectiveness of RESFire. Since CAM5 simulated atmosphere internal variability does not necessarily represent the interannual variability of real atmosphere, we only examined the statistical characteristics of RESFire online results with bias corrections (RESFire_CAM5c). The 10-year averaged RESFire_CAM5c carbon emissions are larger than the GFED4.1s and RESFire_CRUNCEP by 18% and 16%, respectively. High bias region includes temperate North America, northern hemisphere of South America, Europe, and Middle East. (Figure 30b). One consequence is that the tendency of underestimating fire induced aerosol loading [63] was not as severe in the online CAM5 simulations. The published LL2013 CLM4.5-fire carbon emission is 2.1Pg C yr^{-1} averaged from 1997 to 2004 [128], which is lower than our results here, but we should point out again that such biases could result from different atmosphere forcing data and benchmarks used in LL2013.

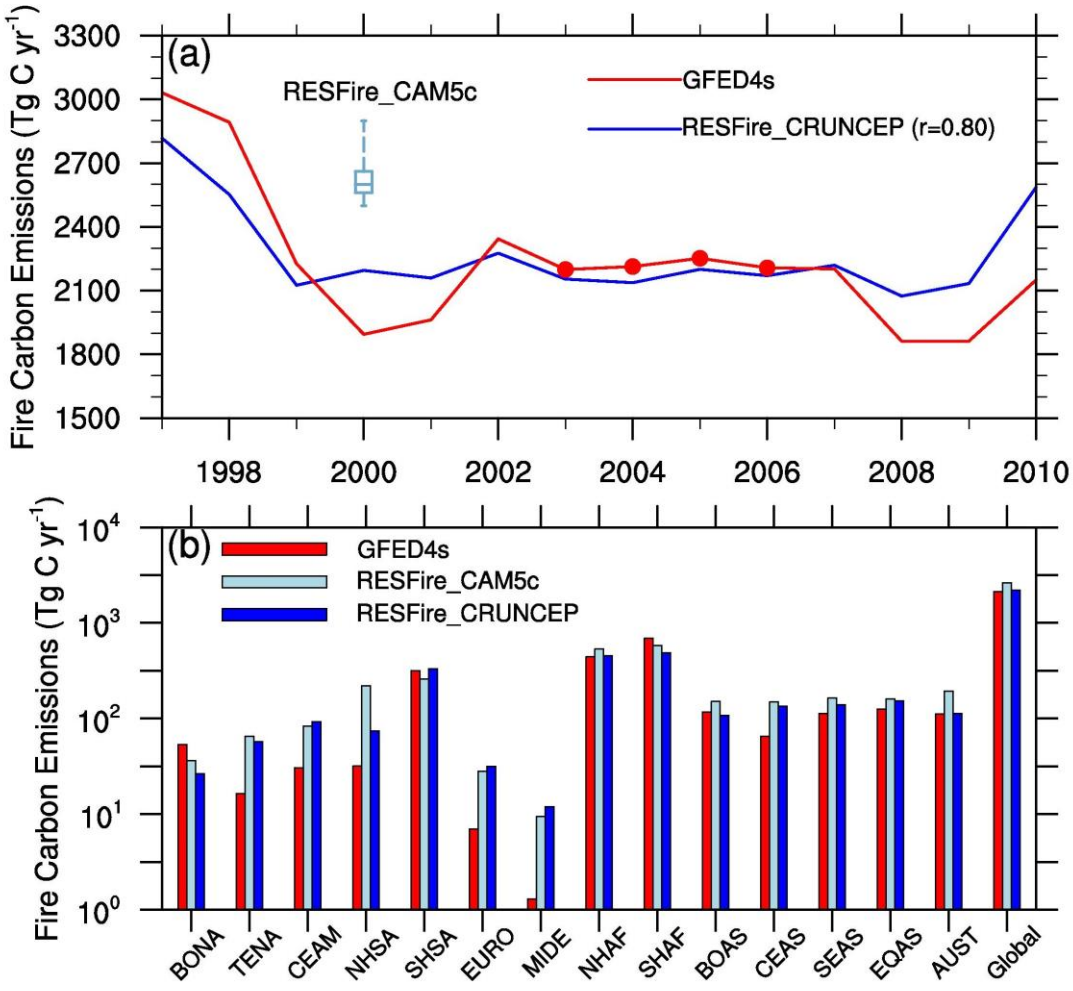

Figure 30 – Comparisons of interannual and regional fire carbon emissions. (a) Temporal variations of annual fire carbon emissions from GFED4.1s and RESFire_CRUNCEP with the correlation coefficient shown in the parenthesis. The red dots denote the years used for fire model training. Statistical results from RESFire_CAM5c under the 2000-year climate condition are shown in the box for comparison. (b) Regional and global annual fire carbon emissions from GFED4.1s, RESFire_CRUNCEP, and RESFire_CAM5c. The 14 regions are the same with GFED dataset [55]. BONA: Boreal North America; TENA: Temperate North America; CEAM: Central America; NHSA: Northern Hemisphere South America; SHSA:

Southern Hemisphere South America; EURO: Europe; MIDE: Middle East; NHAF: Northern Hemisphere Africa; SHAF: Southern Hemisphere Africa; BOAS: Boreal Asia; CEAS: Central Asia; SEAS: Southeast Asia; EQAS: Equatorial Asia; AUST: Australia and New Zealand.

In Table 14, we examined the averaged fire emissions (1997-2010) of specific trace gases and aerosol species. The default CLM45bgc_CRUNCEP does not provide fire emissions for each species, so we only compared the offline RESFire_CRUNCEP and online RESFire_CAM5c results with the GFED4.1s data. Both modeling outputs agree well with the benchmark data in most species. It is also noted that RESFire_CAM5c results have lower interannual variability than GFED due to the suppressed internal variability with fixed external forcing in CAM5 atmosphere.

Table 14 – Comparisons of annual averaged fire emissions with standard deviations of interannual variability

Units: Tg yr^{-1}	GFED4s	RESFire_CRUNCEP	RESFire_CAM5c
Carbon	2235±346	2271±221	2629±106
CO_2	7574±1133	7665±1081	8421±426
CO	365±81	423±92	446±23
CH_4	16±6	21±6	21±1.2
NMHC	18±2	24±1	27±1.2
H_2	10±1.9	11±0.7	12±0.6
NO_x	15±1.8	14±1	16±0.8
N_2O	0.95±0.15	0.75±0.05	0.87±0.04
$PM_{2.5}$	37±6	35±2	40±2
TPM	48±8	52±3	59±3
TC	19±3.7	18±1	21±0.9
OC	17±3	18±3	19±0.9
BC	1.9±0.3	2.4±0.2	2.7±0.1

We also compared spatial distributions of simulated FRP against satellite observations (MYD14CMH) onboard Aqua MODIS [117] in Figure 31. All data are annual averaged from 2003 to 2010. The uncertainties in the conversion factors also contribute to the discrepancies between the observations and simulation results. Both offline and online simulation results had low biases in most regions except over Africa, where the simulation results were overestimated to some extent. However, the discrepancies at such degree are acceptable because the simulated FRP mostly affect the fire-induced tree mortality estimation, which bears larger uncertainties in the ecosystem responsive relationship to fire disturbances as we saw in Figure 27. We examined the fire related tree mortality and regrowth in the next section to demonstrate the RESFire modeling capability regarding ecosystem feedbacks to fire.

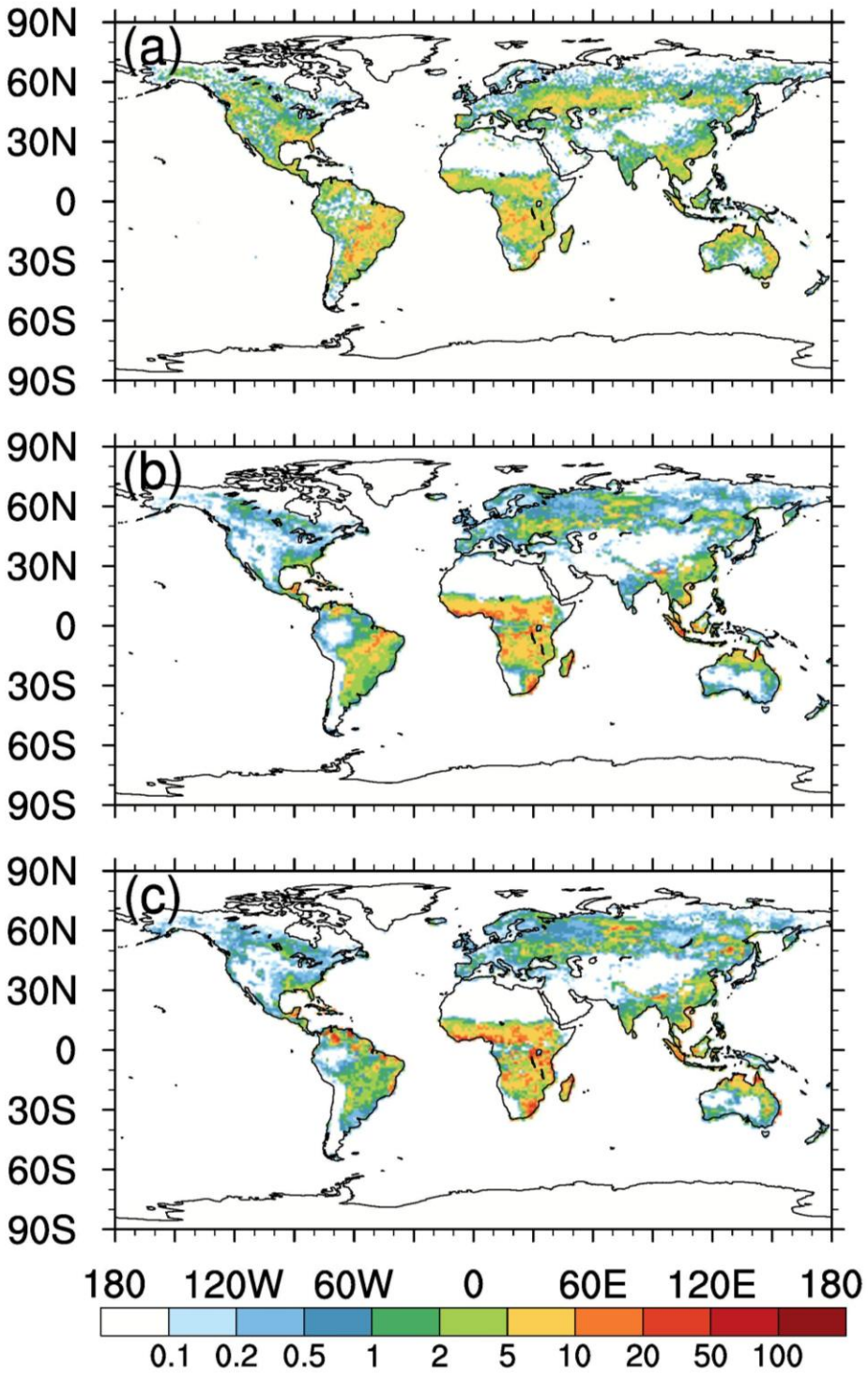
(a)
(b)
(c)
90N
60N
30N
0
30S
60S
90S
180
120W
60W
0
60E
120E
180
0.1
0.2
0.5
1
2
5
10
20
50
100

Figure 31 – Comparisons of observed and simulated FRP. (a) Annual average FRP (mW/m^2) from Aqua MODIS observations; (b) and (c) are same as (a) but from RESFire_CRUNCEP and RESFire_CAM5c, respectively.

4.2.3 Ecosystem Disturbances

Given the sparsity of global fire induced mortality data, we only compared the simulated tree mortality with the satellite data over boreal regions [62]. Similar to the satellite observations, the RESFire mortality results show higher mortality in North America regions and lower mortality over Eurasia (Figure 32). Such distinctions are derived from different fire behaviour and plant traits. To be specific, American fires are characterized by more crown fire with higher intensity and severity, while Eurasian fires are dominated by surface fires with lower intensity and severity [62]. The tree species with stronger burning endurance are also predominant in Eurasia. Both factors determine the different tree mortality rates in response to fire. The model therefore captures the contrast of tree mortality rate between the two regions, though the model underestimates the mortality rates in Alaska and Siberia due to the low biases in model estimated burned area and FRP. Such low biases are derived from a shortage of sufficient natural and anthropogenic fire triggers in the model with low lightning and population density over these regions. While the current implementation of tree mortality will require further improvements, we note that if only partial vegetation mortality is included, the model simulated recovery rate would be artificially fast since the reduction of leaf area index (LAI) would enhance light use efficiency of photosynthesis. When the whole plant mortality is included, the regrowth time will be longer and more realistic.

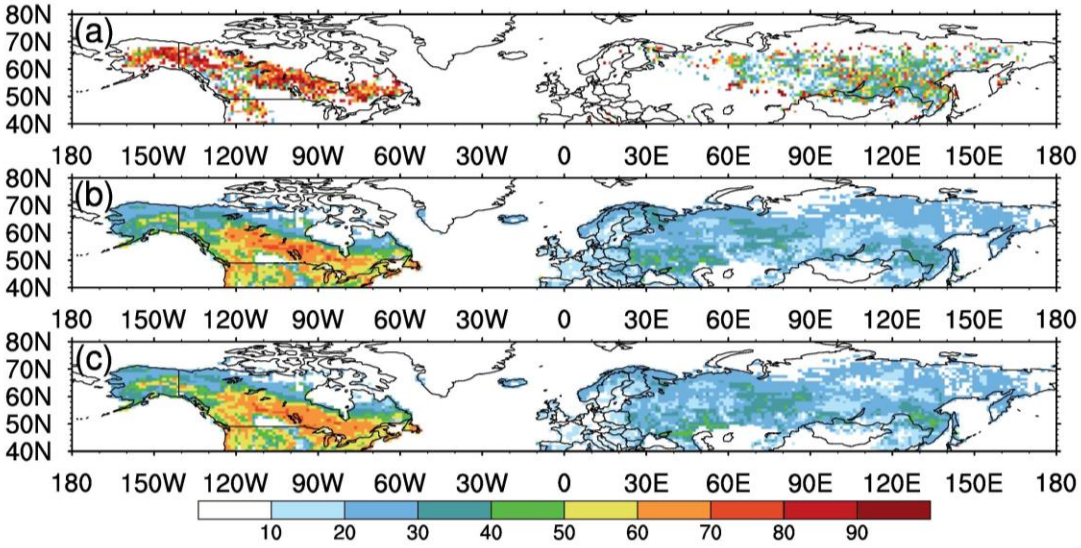

Figure 32 – Comparisons of fire induced tree mortality rates (%) in satellite observations and model simulations. (a) Annual averaged tree mortality rates based on satellite observations from 2001 to 2009; (b) annual averaged tree mortality rates in the fire seasons over the same period from RESFire_CRUNCEP; (c) same as (b) but from RESFire_CAM5c 10-year averaging results under the 2000 climate condition.

To evaluate temporal variability of post-fire ecosystem recovery, we followed previous studies [61] and designed an idealized burning scenario by introducing single-year burning events in fire peak months of each typical fire region. Figure 33 shows the simulated fire disturbance and post-fire evolution of vegetation characteristics and ecosystem production in the context of carbon stock, production, respiration, and efficiency in a sample grid of Canadian boreal forest region (Manitoba: 261° E, 56° N). We chose this site to compare modeling results with theoretical trends as well as *in-situ* and satellite observations in previous studies [156, 160]. The dominant boreal tree species of Manitoba

are black spruce, jack pine, and trembling aspen, while vegetation varies with stand age and soil drainage [161]. *Goulden et al.* [156] examined the temporal variations of boreal forest production and respiration during secondary succession after stand-replacing crown fire. They compared the stand observations with theoretical trends and concluded the transition of post-fire forest stands from carbon source to sink within 11-12 years. *Hicke et al.* [160] assessed the impact of fire on NPP in the North America boreal forest using satellite observations and estimated a similar mean NPP recovery period of about 9 years. The model simulation showed that the total vegetation carbon (TOTVEGC) decreases substantially after fire disturbances because of the implemented plant mortality and fire carbon emission losses. In contrast, the coarse woody debris carbon (CWDC) was estimated to increase as a result of plant mortality. With more loss of productive vegetation, the simulated photosynthesis capability of the ecosystem decreased considerably, leading to significantly decreased gross primary production (GPP) and net ecosystem production (NEP). However, the net primary production (NPP) changes were less significantly than GPP due to reduced competition and respiration consumption after large fractions of plant mortality in the model. Given the estimates of similar reductions in both GPP and autotrophic respiration (AR), simulated NPP only had minor changes, which led to enhanced production efficiency in NPP/GPP. The simulated rates of above changes decreased with time after the fire disturbance and the ecosystem properties were restored to the pre-fire condition around two decades later except TOTVEGC since the vegetation carbon accumulated slowly and required more years to fully restore to the pre-fire level. The post-fire ecosystem evolution showed similar variations in other regions, though the recovery rates are different for other PFT groups (Figure 34). In general, the mean recovery

period of post-fire forest is about 3~18 years with transition from carbon source to sink in each PFT region. These simulations in the idealized experiment agreed well with both theoretical trends and observed variations in previous studies [156, 160], demonstrating good modeling performance in ecosystem responses to fire.

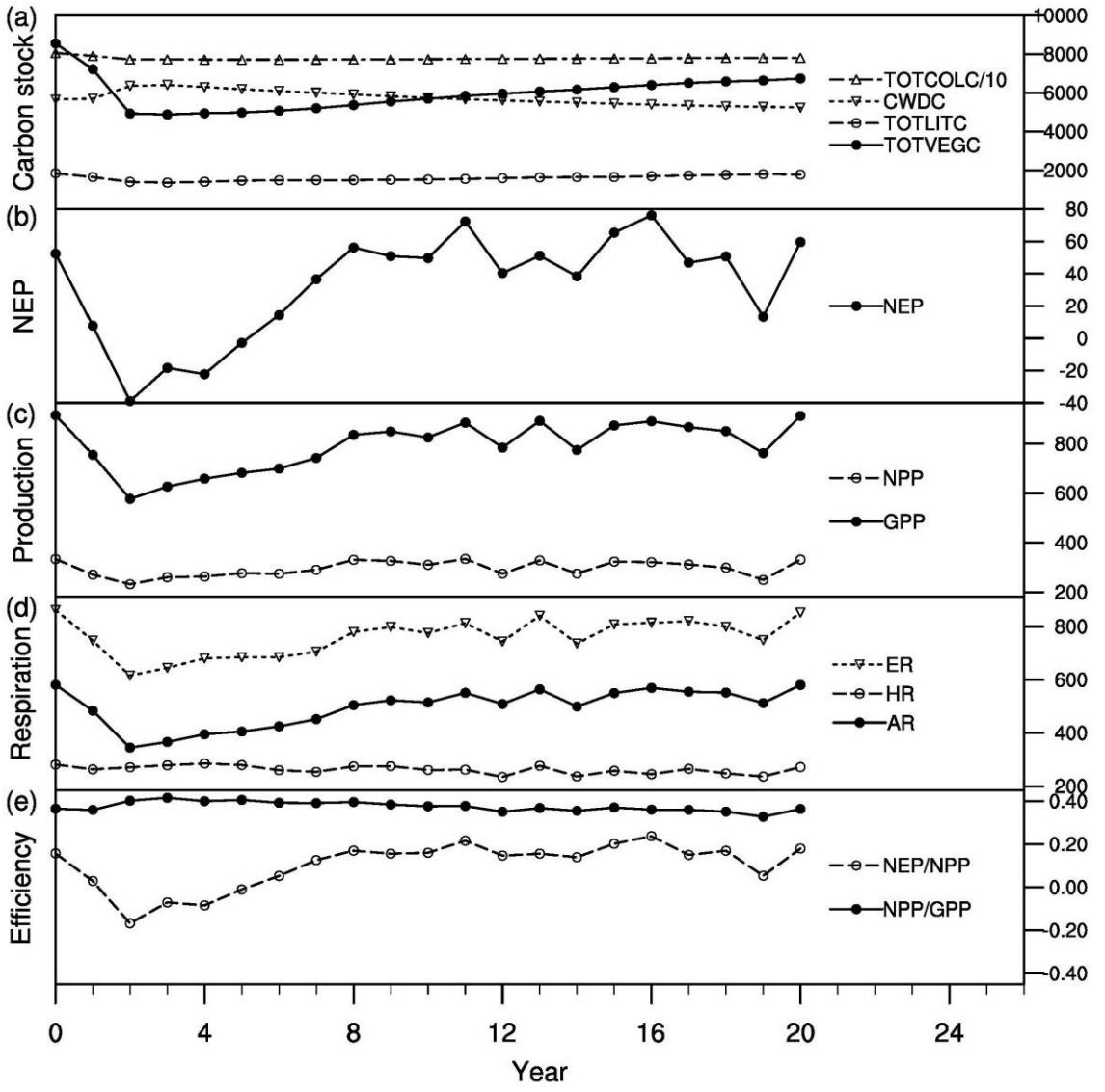

Figure 33 – Simulated post-fire temporal evolution of carbon budget and ecosystem productivity in Manitoba based on the idealized burning experiment. (a) total column carbon (TOTCOLC, gC/m^2), coarse woody debris carbon (CWDC, gC/m^2), total litter

carbon (TOTLITC, gC/m^2), and total vegetation carbon (TOTVEGC, gC/m^2); (b) Net ecosystem production (NEP, gC/m^2/yr); (c) Net primary production (NPP, gC/m^2/yr) and gross primary production (GPP, gC/m^2/yr); (d) total ecosystem respiration (ER, gC/m^2/yr), heterotrophic respiration (HR, gC/m^2/yr), and autotrophic respiration (AR, gC/m^2/yr); (e) ecosystem carbon storage efficiency (NEP/NPP, unitless) and plant production efficiency (NPP/GPP, unitless). The time of fire disturbance is at year 0.

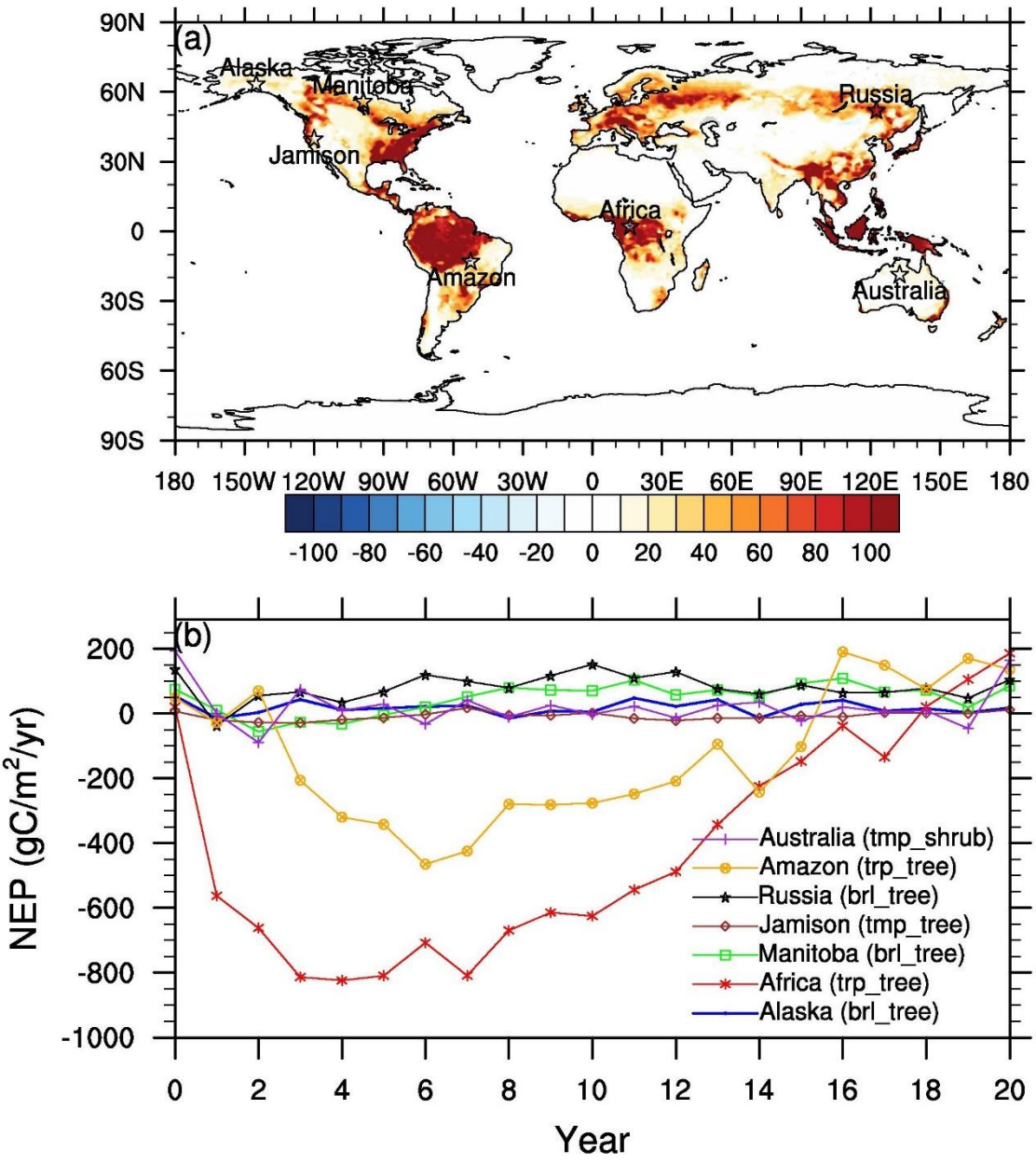

Figure 34 – Simulated post-fire temporal evolution of carbon budget in different PFT regions based on the idealized burning experiment. (a) spatial distributions of annual averaged NEP (gC/m^2/yr); (b) temporal variations of post-fire NEP in each disturbed grid.

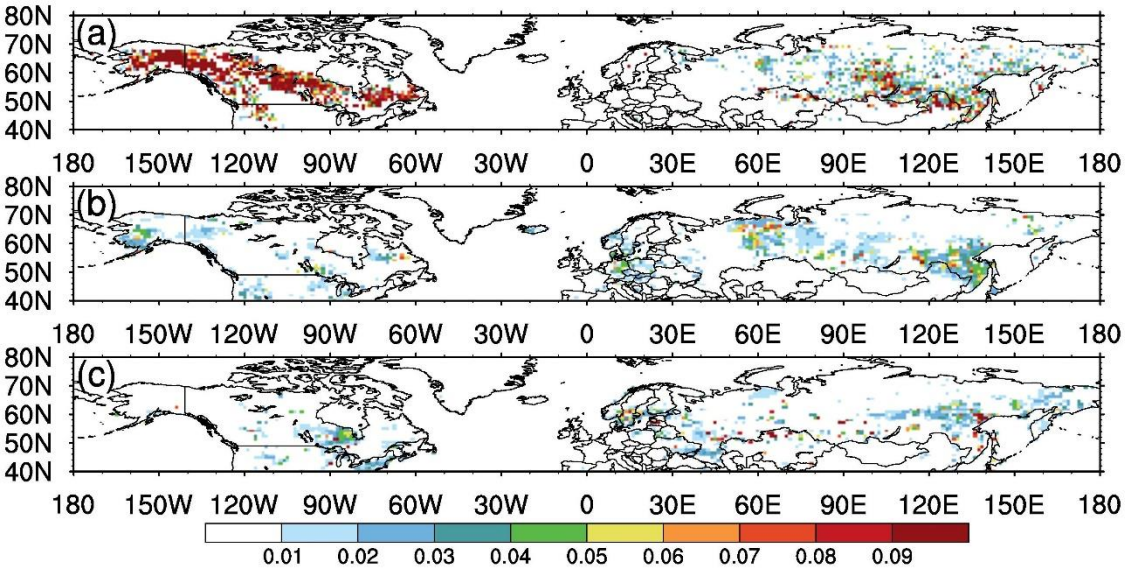

Figure 35 – Comparisons of fire induced spring albedo changes (unitless) based on satellite observations and model simulations. (a) annual averaged spring albedo changes based on MODIS satellite observations from 2003 to 2006; (b) annual averaged spring albedo changes based on RESFIRE_CRUNCEP simulations from 2003 to 2006; (c) same as (b) but from RESFIRE_CAM5c under the 2000-year climate condition.

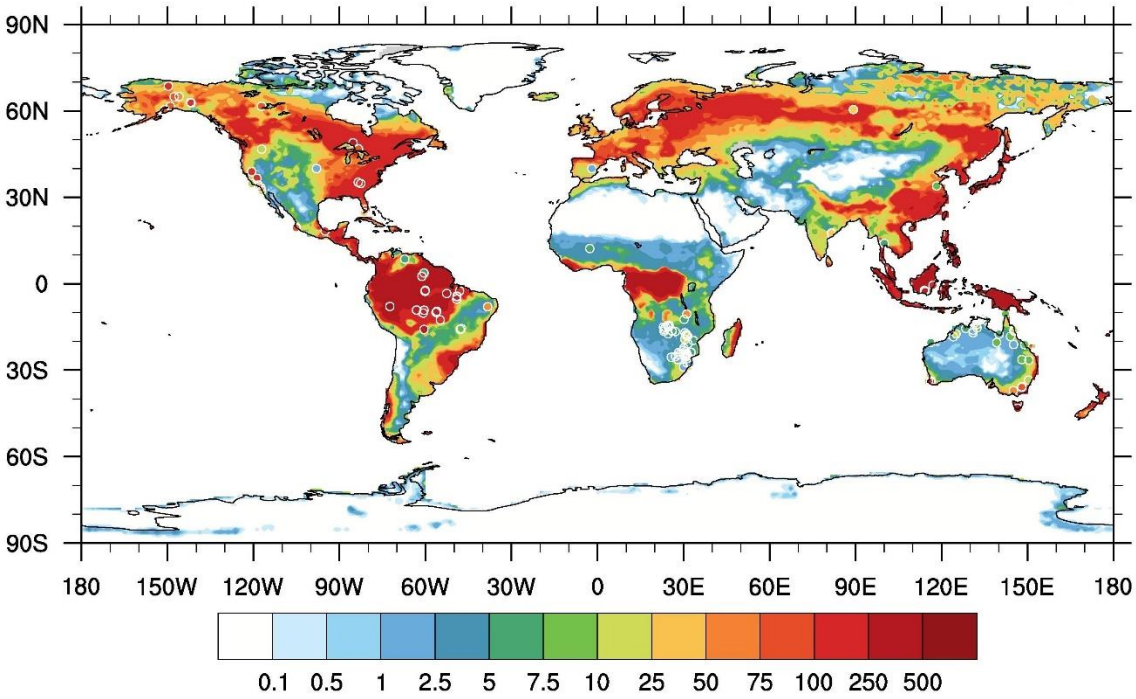

Figure 36 – Comparisons of fuel loads (unit: t/ha) in CLM (contour shading) and *in-situ* measurements (white circles).

4.3 Conclusions and Discussion

In this work, we developed a region-specific ecosystem feedback fire model that fully considers regional differences in fire behavior and impacts. We refined the fire occurrence and spread parameterization and added online fire weather bias corrections as well as ecosystem disturbances in the model. The RESFire model performed well according to the ILAMB benchmarking results, which suggest significant improvements of burned area simulation in both offline CRUNCEP data atmosphere driven mode and online CAM5 driven mode. The overall fire modeling scores increase from 0.50 of the default CLM LL2013 fire scheme to 0.61 of RESFire_CRUNCEP and 0.60 of RESFire_CAM5c with improved spatial and temporal distributions of fire activities. The

fire impact evaluation results also demonstrated good modeling capability in fire emissions in forms of mass and energy fluxes. The mean annual fire carbon emissions of RESFire agreed well with the latest GFED4.1s data within 12% in offline and online modes. Fire emissions for gaseous and aerosol species as well as energy fluxes showed generally good agreement with benchmarking data. With the implementation of whole plant mortality and recovery, the simulations of fire disturbances on ecosystems and land cover were more comprehensive to capture multiple post-fire impacts such as increasing surface albedo in boreal forest with decreasing radiative forcing in a long-term time scale [57] (Figure 35). We summarized the comparison between the RESFire model in this work and the default CLM LL2013 fire model in Table 15. These advanced modelling features with fully interactive climate-fire-ecosystem mechanisms are essential to understand the role of fire in the climate system and ecosystem changes.

Table 15 – Comparisons between the RESFire model and the LL2013 fire model

Fire model		The LL2013 fire model	RESFire
Occurrence	Ignition	climatological lightning and anthropogenic triggers	climatological lightning and anthropogenic triggers
	Flammability	a global function of fuel load, RH, and soil wetness	region- and PFT-specific functions of fuel load, T10, PREC10, and soil water
	Suppression	a function of population density and GDP	region- and PFT-specific functions of population density and a global unified function of GDP
Spread	Spread rate	a function of wind speed and fuel wetness	functions of wind speed and fuel wetness
	Duration	fixed (1 day)	fixed (1 day)
	Combustibility	a function of root zone soil wetness and RH	region- and PFT-specific functions of T, RH, SW, and FWET
	Suppression	a function of population and GDP	region- and PFT-specific functions of population and global unified function of GDP as well as passive constraints from terrain and landscape fragmentation
Impact	Emissions	carbon emissions at surface	carbon, trace gases and aerosols with dynamic plume rise
	Ecosystem disturbance	vegetation mortality with fixed mortality rates for each part (leaf, stem, root, etc.)	vegetation mortality and fire intensity sensitive whole plant mortality, PFT dependent recovery, and land cover changes
	Radiation budget	none	sensible and latent heat fluxes

CHAPTER 5. UNDERSTANDING CLIMATE-FIRE-ECOSYSTEM INTERACTIONS USING RESFIRE AND IMPLICATIONS FOR DECADAL CLIMATE VARIABILITY

In the previous chapter, we developed a region- and PFT-specific fire model (RESFire) with comprehensive climate and ecosystem feedback mechanisms in the CESM modeling framework. The RESFire model performs well driven by either offline data atmosphere and online CAM5 simulated atmosphere, which enables the advanced modeling capability to investigate the complex climate-fire-ecosystem interactions as well as to predict future climate change with fully interactive fire disturbances. Therefore, we designed and conducted series of numerical experiments using the RESFire model to explore the role of fire in the climate system and its influence on decadal climate variability.

5.1 Modeling Experiments

RESFire includes two major fire impact pathways: the direct fire disturbances through fire emissions and the indirect fire disturbances through land use and land cover changes (LULCC). These two pathways correspond to two disturbance objects, the climatic radiative forcing and the terrestrial carbon balance. To quantify fire impacts on these two terms in different climate background, we designed two groups of sensitivity simulations for present day and future scenarios in Table 16. In each simulation groups, we conducted one control run (CTRLx) and two sensitivity runs (SENSxA/B). The CTRL runs were designed with fully interactive fire disturbances such as fire emissions with plume rise and fire induced LULCC with different boundary conditions for present day (CTRL1) and a moderate future emission scenario (CTRL2) of the Representative Concentration Pathway 4.5 (RCP4.5), respectively. In each scenario, we successively turned off the direct and indirect fire disturbance mechanism in the sensitivity runs to isolate each fire feedback

influence. For instance, we estimated the direct impact of fire emissions on radiative forcing at present day (RCP4.5 future scenario) by comparing SENS1A (SENS2A) with CTRL1 (CTRL2). We also estimated the indirect impact of fire induced LULCC on terrestrial carbon balance at present day (RCP4.5 future scenario) by comparing SENS1B (SENS2B) with SENS1A (SENS2A). The total fire impact was evaluated by differencing CTRL runs with SENSxB runs since both fire feedback mechanisms were turned off in the latter. Using these sensitivity experiments, we are capable to evaluate the two-way climate-fire-ecosystem interactions that are beyond the scope of previous one-way perturbation studies in terms of either climate impacts on fires [118, 162, 163] or fire feedback to climate [63, 128, 164, 165].

Table 16 – Fire sensitivity simulation experiments for the present-day and RCP4.5 future scenarios

Scenario	Present day (2000)			Future (RCP4.5)		
Name	CTRL1	SENS1A	SENS1B	CTRL2	SENS2A	SENS2B
Time	2001-2010	2001-2010	2001-2010	2051-2060	2051-2060	2051-2060
Atmosphere	CAM5	CAM5	CAM5	CAM5	CAM5	CAM5
Land	CLM4.5	CLM4.5	CLM4.5	CLM4.5	CLM4.5	CLM4.5
Ocean	Climatology	Climatology	Climatology	RCP4.5 data	RCP4.5 data	RCP4.5 data
Sea ice	Climatology	Climatology	Climatology	RCP4.5 data	RCP4.5 data	RCP4.5 data
Non-fire emissions	ACCMIP	ACCMIP	ACCMIP	RCP4.5	RCP4.5	RCP4.5
Fire emissions	Online fire aerosols with plume rise	–	–	Online fire aerosols with plume rise	–	–
Land cover	Fire disturbance on present-day conditions	Fire disturbance on present-day conditions	Fixed present-day conditions in 2000	Fire disturbance on RCP4.5 conditions	Fire disturbance on RCP4.5 conditions	Fixed RCP4.5 conditions in 2050

5.1.1 Climate Models

1. CAM5

As the latest version of the atmosphere model in CESM, CAM5 is coupled by the dynamical core and the physical parameterization suite. There are four options for the dynamical core [90], including the Finite-Volume (FV) dynamical core, the Spectral Element (SE) dynamical core, the Eulerian dynamical core, and the semi-Lagrangian dynamical core. The total parameterization package in CAM5 also consists of four primary components that are precipitation processes, clouds and radiation, the surface model, and turbulent mixing [90]. Each of them is then divided into various sub-components. The major improvements in CAM5 include:

(1) A new moist turbulence scheme [166] that explicitly simulates stratus-radiation-turbulence interactions;

(2) A new shallow convection scheme [167] using a realistic plume dilution equation and closure;

(3) A prognostic, two-moment formulation [168] for cloud droplet and cloud ice with mass and number concentrations that represents stratiform microphysical processes;

(4) A revised cloud macrophysics scheme [169] that provides a more transparent treatment of cloud processes and imposes full consistency between cloud fraction and cloud condensate;

(5) An updated radiation scheme (the Rapid Radiative Transfer Method for GCMs (RRTMG), [170, 171]) that employs an efficient and accurate modified correlated-k method for calculating radiative fluxes and heating rates;

(6) A new 3-mode modal aerosol scheme (MAM3, [172]) with internally mixed representations of number concentrations and mass for Aitkin, accumulation, and coarse aerosol modes;

(7) A full inventory of observationally based aerosol emission mass and size;

These physical enhancements permit new research capabilities to assess aerosol impacts on cloud properties and radiative forcing. As such CAM5 represents the first version of CAM with the modelling capability of cloud-aerosol indirect radiative effects[90], which are of great interest of this climate-fire interaction study.

2. CLM4.5

As the latest version of the land model for CESM, CLM represents several land surface aspects regarding surface heterogeneity. It consists of multiple sub-models for land biogeophysics, biogeochemistry, the hydrological cycle, human dimensions, and ecosystem dynamics [111]. The major improvements in CLM4.5 include:

(1) A revised canopy radiation scheme and canopy scaling of leaf processes [173];

(2) A revised photosynthesis scheme [174];

(3) Improved cold region hydrology and optional VIC-based hydrology [175, 176];

(4) A new snow cover fraction parameterization [177];

(5) A new lake model [178];

(6) A newly introduced surface water store that permits prognostic wetland distribution modeling [177];

(7) A Century-like vertically resolved soil biogeochemistry scheme with revised denitrification and biological fixation processes [179];

(8) A revised fire model including anthropogenic triggers and suppression as well as agricultural, deforestation, and peat fires [112, 122], which was further improved as is shown in the previous section;

(9) An updated biogenic volatile organic compounds model (MEGAN2.1, [180]);

(10) A methane production, oxidation, and emission model [181];

(11) An extension of the crop model including interactive fertilization, organ pools [182], and irrigation [183];

(12) 13C and 14C isotope fractionation [179];

(13) Newer and higher resolution input datasets;

All the improvements together with the new RESFire model and other modeling features in CAM5 and CLM4.5 provide the state-of-the-science simulation capability to examine the physical, chemical, and biological processes by which global fires interact with climate and terrestrial ecosystems.

5.1.2 Model Input Data

We used the simulation results from the last chapter as the initial conditions for the present-day sensitivity experiments (CTRL1/SENS1x) in this chapter to save the spin-up

time. The boundary conditions including the prescribed climatological (1981-2010 average) sea surface temperature and sea ice data for the present-day scenario were provided by Met Office Hadley Centre (HadISST) [81]. Similarly, the nitrogen and aerosol deposition rates were also prescribed from a time-invariant spatially varying annual mean file for 2000 and a time-varying (monthly cycle) globally-gridded deposition file, respectively, as the standard data sets necessary for the present-day CAM5 simulations [89]. The climatological 3-hourly cloud-to-ground lightning data via bilinear interpolation from NASA LIS/OTD grid product v2.2 (http://ghrc.msfc.nasa.gov) 2-hourly lightning frequency data and the world population density data were fixed at the 2000 levels for all the present-day simulations. The non-fire emissions from anthropogenic and other sources at present-day were based on ACCMIP [184] for the 2000 year. We replaced the old prescribed GFED2 fire emissions [185] in the default setting with online coupled fire emissions generated by the RESFire model in the CTRL runs. We then turned the coupled fire emissions off in the SENS runs to evaluation fire direct impacts on radiative forcing. We used the fixed historical land use and land cover change data for 2000 based on version 1 of the Land-Use History A product (LUHa.v1) [154] for the CTRL1 run. We then perturbed the LULCC data in the sensitivity experiments as described in RESFire model development to evaluate fire indirect impacts on terrestrial ecosystems.

For the future scenario experiments, we replaced all the present-day datasets with the RCP4.5 prediction datasets including the prescribed boundary conditions of global SST and sea ice data in 2050, the cyclical non-fire emissions and deposition rates fixed in 2050 under the RCP4.5 scenario, and the annual LULCC data for the RCP4.5 transient period in 2050 based on the Future Land-Use Harmonization A products (LUHa.v1_future) [154]. All these datasets were described in the technical note of CAM5 [90] and the introduction of CESM [89] and stored on the NCAR Yellowstone system. It is worth noting that we kept the climatological lightning data and the population density data in the future scenario

experiments the same with the present-day scenario due to data availability and great uncertainties in those future projection data. In other words, we did not consider the influence of demographic changes and lightning frequency changes in our future projection simulations but focused on the impact of climate change other than lightning.

The global mean GHG mixing ratios in the CAM5 atmosphere model were fixed at the 2000 levels (CO_2: 367.0ppmv; CH_4:1760.0ppbv; N_2O:316.0ppbv) in all present-day experiments and they were provided by the prescribed RCP4.5 projection datasets with the well-mixed assumption and monthly variations in the future scenarios. These GHG mixing ratios were then broadcasted to the CLM4.5 land model in all scenarios. In return, the land model diagnosed the balance of all carbon fluxes between net ecosystem production (NEP, g $CO_2/m^2/s$, positive for carbon sink) and depletion from fire emissions, landcover change flux, and carbon loss from wood products pools etc., and then outputted the net CO_2 flux to the atmosphere model in forms of net ecosystem exchange (NEE, g $CO_2/m^2/s$, positive for carbon source). Though fire emissions could influence the value of NEE, it is often assumed that fire carbon emissions are offset by carbon absorption of vegetation regrowth and fires are neither a source nor a sink for CO_2 [28]. Therefore, we did not consider the radiative forcing of fire related greenhouse gases (GHGs) in our sensitivity experiments.

5.1.3 Model Performance Evaluation Benchmarks

Multiple observational and simulated datasets were applied to evaluate the modelling performance related with radiative forcing. We collected space based and ground based column aerosol optical depth (AOD) products from MODIS [72] and the Aerosol Robotic Network (AERONET, https://aeronet.gsfc.nasa.gov/) to compare with the model simulated AOD. We then followed the *Ghan*'s method [186] to estimate fire aerosol

effects on the planetary energy balance through direct radiative forcing, cloud radiative forcing, and surface albedo forcing (Equation 42).

$$\begin{gathered} Direct\ radiative\ forcing: \Delta(F - F_{clean}) \\ Cloud\ radiative\ forcing: \Delta\left(F_{clean} - F_{clear,clean}\right) \\ Fire\ aerosol\ surface\ albedo\ forcing: \Delta F_{clear,clean} \\ Total\ aerosol\ forcing: \Delta F = \Delta(F - F_{clean}) + \Delta\left(F_{clean} - F_{clear,clean}\right) + \Delta F_{clear,clean} \\ Land\ cover\ change\ surface\ albedo\ forcing: F_{SENS1A} - F_{SENS1B} \end{gathered} \tag{42}$$

Here Δ is the difference between atmosphere simulations with and without fire emissions, F is the shortwave radiative flux at the top of the atmosphere, F_{clean} is the radiative flux calculated as an additional diagnostic from the same simulations but neglecting the scattering and absorption of solar radiation by all the aerosol, and $F_{clear,clean}$ is the flux calculated as additional diagnostic but neglecting scattering and absorption by both clouds and aerosols. The surface albedo forcing is largely the contribution of changes in surface albedo induced by fire aerosols and land cover changes, which is small but nonnegligible in some specific regions [186]. We compared our online coupled fire estimations with previous offline prescribed fire modeling studies [63, 187] and analyzed the differences.

We also examined the fire modeling performance regarding terrestrial carbon balance such as burned area and fire carbon emissions, gross primary production (GPP, positive for carbon sink), net primary production (NPP, positive for carbon sink), net ecosystem productivity (NEP, positive for carbon sink), and net ecosystem exchange (NEE, positive for carbon source). These carbon budget related variables were calculated in Equation 43-44 and compared against the satellite based GFED4.1s datasets [53, 55,

126], the MODIS primary production products [188, 189], and the previous modeling results used for terrestrial model comparison projects [190, 191] to generate a comprehensive evaluation.

$$\mathrm{GPP} = \mathrm{NPP} + R_a = (\mathrm{NEP} + R_h) + R_a \tag{43}$$

$$\mathrm{NEE} = C_{fe} + C_{lh} - \mathrm{NEP} \tag{44}$$

Here R_a is the total ecosystem autotrophic respiration (g C/m^2/s), R_h is the total heterotrophic respiration (g C/m^2/s), C_{fe} is the fire carbon emissions (g C/m^2/s), and C_{fe} is the carbon loss (g C/m^2/s) due to landcover change, wood products, and harvest.

5.2 Modeling Results and Analysis

5.2.1 Radiative Forcing

Figure 37 shows the comparison between CAM5 simulated column AOD and satellite retrieved MODIS AOD at 550nm. It's noted that both AOD data resulted from all emission sources including fire and non-fire emissions, and significant differences are found in specific regions due to large biases in modeling emissions. In the MODIS AOD data, the most predominant hot spot regions include eastern China as discussed in Chapter 2 and 3, South Asia such as India, and Africa. The first two hot spots are contributed mostly by anthropogenic emissions, while the last hot spot region is dominated by fire emissions. Since the non-fire emissions used in CAM5 simulations are biased low, these hot spots in east and south Asia regions are not as appreciable as those observed in remote sensing data. However, the model well captures the high AOD regions over the north and south Africa,

where have large biomass burning contributions. It's also noticeable that the CAM5 model overestimates the dust emissions significantly since some spuriously high AOD hot spots emerge over the Sahara and Arabian desert regions.

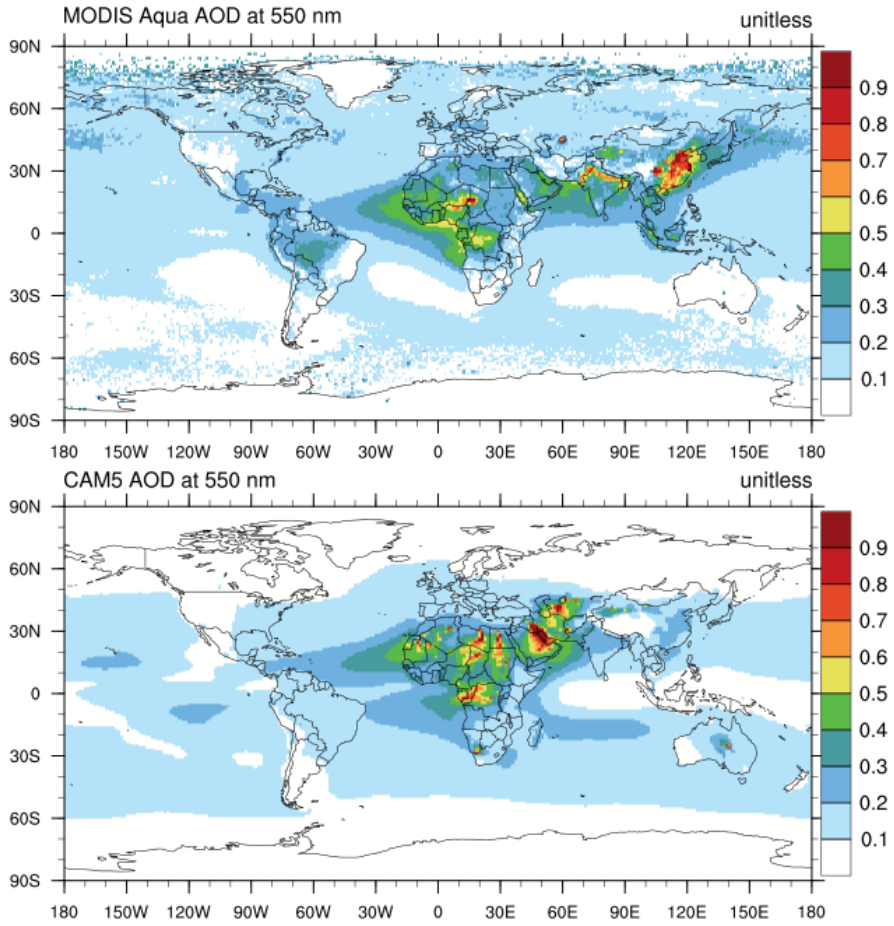

Figure 37 – Comparison of annual averaged MODIS retrieved column AOD at 550nm (top) aboard the Aqua satellite and CAM5 simulated column AOD at 550nm (bottom) in 2000.

To further evaluate the fire related AOD modeling performance, we compared the difference between CTRL1 and SENS1A to isolate the contributions from fire emissions in Figure 38. The spatial distributions clearly reveal African savanna as the major biomass

burning region around the world. We also compared the monthly AOD at 6 fire-prone sites with AERONET *in situ* observations to get a better understanding of temporal variations. Most sites show strong seasonal variations in monthly AOD as observed by AERONET, and the fire model well captures fire seasons in these regions with certain biases in simulated AOD. Generally, the CAM5 AOD results show low biases in most regions, especially over the Southeast Asia rain forest regions like Chiang Mai, where deforestation and agricultural related burning activities prevail.

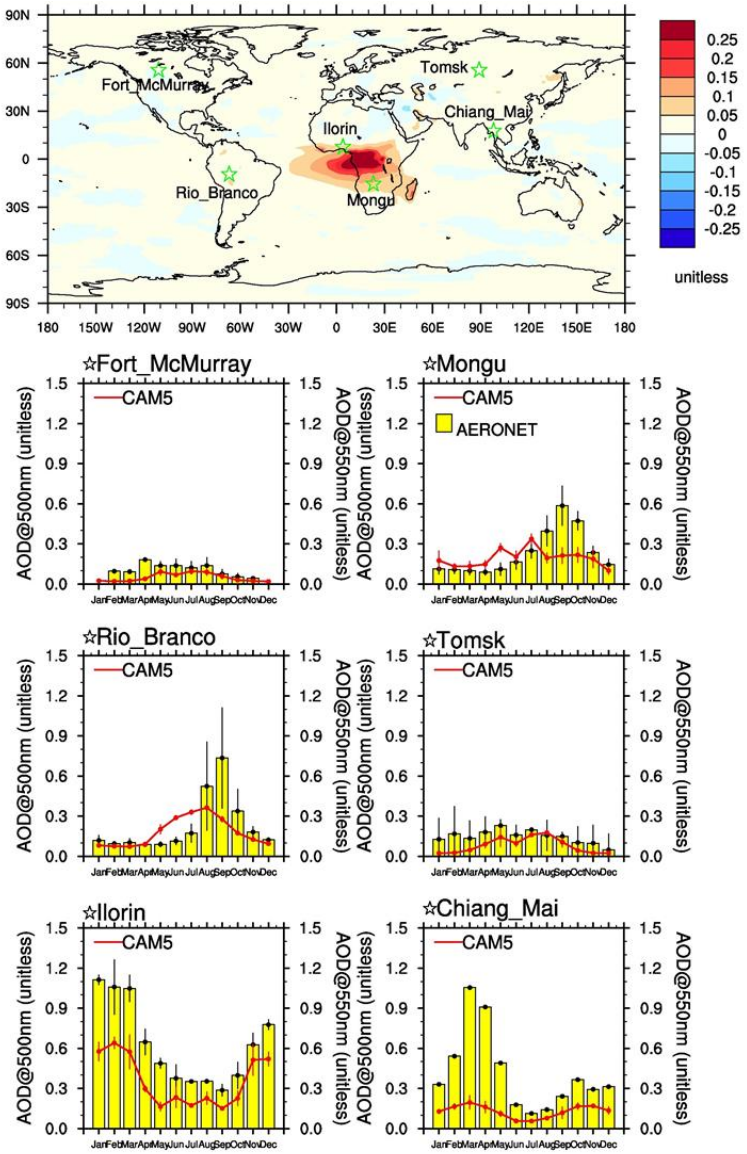

Figure 38 – Annual averaged fire related AOD at 550nm and comparisons with AERONET *in situ* observations in 2000.

Lastly, we estimated the radiative forcing of fire induced aerosol and land cover changes and compared with previous studies in Figure 39 and Table 17. As expected, the fire aerosol direct radiative forcing is most prominent in tropical Africa and downwind ocean regions, where show the strongest warming effects due to burning activities in African savanna. In contrast, the fire aerosol induced cloud radiative forcing shows generally cooling effects in most regions due to enhanced cloudiness, and such cooling effects are more pervasive over high latitude regions such as boreal forest in North America and eastern Siberia. The surface albedo RF shows similarly spatial patterns with moderate cooling effects in boreal regions. The global averaged values for the fire aerosol direct, cloud, and surface albedo RF in 2000s are 0.08 ± 0.04 W/m^2, -1.0 ± 0.09 W/m^2, and -0.08 ± 0.10 W/m^2, respectively, and the surface albedo RF related with fire induced land cover changes is 0.06 ± 0.11 W/m^2. After combining all these forcing terms, we ended up with a total RF of -0.94 ± 0.17 W/m^2 for the present day scenario, which is much larger than the estimates of around -0.55 W/m^2 in the previous fire RF studies [63, 187]. It's noted that both Ward et al. [63] and Jiang et al. [187] conducted uncoupled fire sensitivity simulations with prescribed fire emissions from CLM3 model simulations [162, 163] and different versions of GFED datasets [126, 192], respectively. The annual fire carbon emissions in Ward et al. [63] ranged from 1.3Pg C yr^{-1} for present day simulations to 2.4Pg C yr^{-1} for the future trajectory with ECHAM atmospheric forcing, while the daily fire BC, POM and SO_2 emissions in Jiang et al. [187] were based on the GFEDv3.1 dataset with an annual averaged fire carbon emission of 1.98Pg C yr^{-1}[192]. Both of their fire emissions were

lower than our RESFire model simulations of 2.6Pg C yr^{-1} (Table 18), which might lead to the differences in fire aerosol radiative forcing estimation. It's also worth noting that all fire emissions were released into the lowest CAM level as surface sources in Ward et al. [63], and the default vertical profile based on the AeroCom protocol [193] was used in Jiang et al. [187]. In our simulations, we developed a simplified plume rise parameterization [194] in RESFire and applied online vertical profiles with diurnal cycles to the vertical distribution of fire emissions. It's reported that our plume rise results suggested higher plume rise heights and penetration rates of fire aerosols to planetary boundary layer (≥50%) in the late afternoon than previous studies [193, 195, 196]. These higher elevated fire plumes with higher penetration rates affected the vertical distribution and lifetime of fire aerosols and further influenced optical properties and radiative forcing. We also compared the future scenario results with the present-day conditions in Table 17, which suggests a ~47% enhancement of total fire aerosol and land cover change radiative forcing from $-0.94\pm0.17 W/m^2$ at present day to $-1.38\pm0.15 W/m^2$ in the RCP4.5 future scenario. Such enhanced negative radiative forcing is dominated by the increasing fire aerosol cloud radiative forcing at a similar changing ratio with Ward et al.'s CCSM future projection results [63].

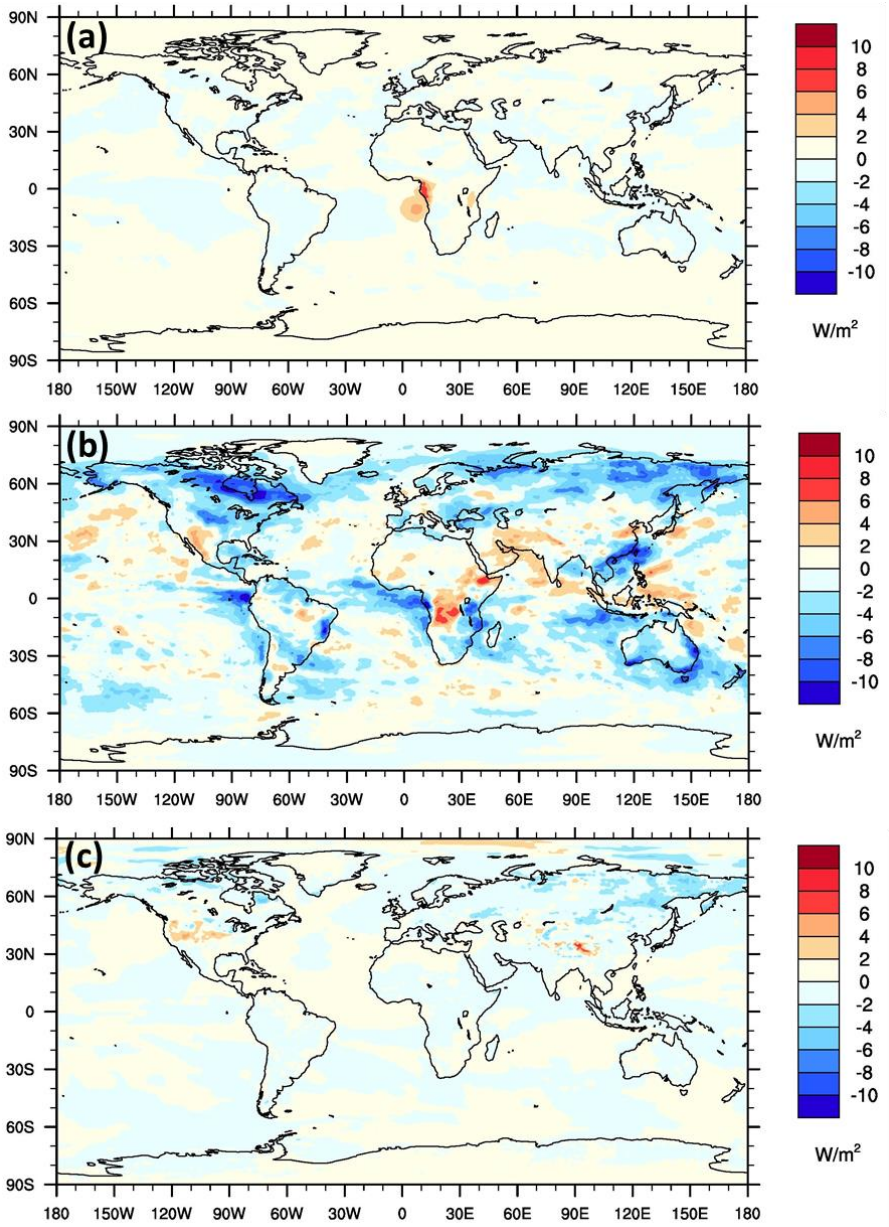

Figure 39 – Fire contributed (a) aerosol direct radiative forcing, (b) cloud radiative forcing, and (c) surface albedo radiative forcing.

Table 17 – Comparisons of fire contributed radiative forcing in present-day and future scenarios based on this work and previous studies

Unit: W/m^2	This work		Jiang et al. [187]	Ward et al. [63]	
Time	2000s	2050s	2000s	2000s	2100s (CCSM/ECHAM)
Aerosol-Radiation Effect	0.08±0.04	0.05±0.04	0.16±0.01	0.10	0.12/0.25
Aerosol-Cloud Effect	-1.00±0.09	-1.40±0.05	-0.70±0.05	-1.00	-1.42/-1.74
Snow/Ice Albedo Effect	-0.08±0.10	-0.06±0.05	0.03±0.10	0.00	0.00/0.00
Land Albedo Effect	0.06±0.11	0.03±0.10	–	-0.20	-0.23/-0.29
Total	-0.94±0.17	-1.38±0.15	-0.55±0.07	-0.55*	-0.83/-0.87*

*: the total radiative forcing includes other effects such as GHGs and climate-BGC feedback;

5.2.2 Carbon Balance

After radiative forcing, we evaluated the RESFire modelling performance regarding terrestrial carbon budget in Table 18. We used the previous modelling studies and the latest GFEDv4.1s datasets as the benchmarks and examined fire related variables including global burned area, fire carbon emissions, GPP, NPP and NEE in the present-day scenario of 2000s. The RESFire model results performs well in global burned area and fire carbon emissions driven by either offline CRUNCEP atmosphere data (RESFire_CRUNCEP) and online CAM5 simulated atmosphere data with bias corrections (RESFire_CAM5c). The annual averaged burned area results are very close to the GFEDv4.1s benchmark value of 510Mha yr^{-1}, while the default fire model in CLM shows significant low biases. When it comes to fire carbon emissions, the offline

RESFire_CRUNCEP result is still consistent with the GFEDv4.1s benchmark of around 2.2Pg C yr^{-1}, and the online RESFire_CAM5c result show a 18% higher value than the benchmark, which is still within the uncertainty range of the benchmark data. It's worth noting that the GFED datasets has low bias issues in fire emissions and modelling studies [41, 63], a moderate increase in fire carbon emissions would alleviate such low bias problems in fire modelling studies and reduce the need for rescaling.

We then compared the CLM simulated carbon budget variables such as GPP and NEE against 10 process-based terrestrial biosphere models that were used for the IPCC fifth Assessment Report [191]. Both the offline and online CLM GPP results are around 142Pg C yr^{-1}, which are higher than the MODIS primary production products (MOD17) of 109.29Pg C yr^{-1} [189] and near the upper bound of ensemble modelling results (133±15Pg C yr^{-1}) [191]. Such high GPP estimation leads to ~11% higher NPP in the CLM simulations than the mean MODIS product of 56Pg C yr^{-1} from 2001 to 2003 as well as the old CLM results by Li et al. [128]. These differences may result from the different atmosphere forcing data used to drive the CLM land model. However, the NEE results based on the RESFire model in CLM are consistent with the benchmarks from the IPCC AR5 and ensemble modelling results, indicating the robustness of the fire and land modelling performance.

Table 18 – Comparisons of RESFire modeling results of carbon budget with previous studies

Variables	Time	This work		Li et al. [128]	Benchmark	Sources
Models		RESFire-CRUNCEP	RESFire-CAM5	DATM-CLM4.5		
Burned Area (Mha/yr)	1997-2004	508±15	472±14	322	510±27	GFED4.1s [53, 126]
Fire Carbon Emissions (Pg C/yr)	1997-2004	2.3±0.2	2.6±0.1	2.1	2.2±0.4	GFED4.1s [55]
NEE (Pg C/yr)	1990s	-2.6±0.6	-2.0±1.3	-0.8	-1.1±0.9	IPCC AR5 [197]
					-2.0±0.8	10 models average [191]
GPP (Pg C/yr)	2000-2004	142±2	142±1	130	133±15	10 models average [191]
NPP (Pg C/yr)	2000-2004	62±1	63±0.7	54	54	Zhao and Running [188]

After the evaluation of carbon budget in the CLM land model, we further decomposed the components in NEE and compared the new RESFire simulation results with the old fire model simulations by Li et al. [128]. We isolated the fire contributions to each carbon budget variables by differencing the fire-on and fire-off experiments driven by the data atmosphere in Table 19 following the same setting in Li et al. [128]. We found a 58% increase in fire induced NEE variations simulated by RESFire than the old LL2013 fire model. This increase is mainly contributed by both enhanced fire emissions and suppressed NEP by RESFire. As discussed in the previous section, RESFire simulated higher annual averaged fire carbon emissions (2.08Pg C yr^{-1}) than the LL2013 fire model (1.9Pg C yr^{-1}) in CLM, which contributed 31% of the difference. Meanwhile, RESFire simulated smaller NEP changes due to fire, which could be attributed to newly added fire

induced land cover changes. In RESFire, we considered fire induced whole plant mortality and post-fire vegetation recovery as discussed in Chapter 4, both of which were missing in the default LL2013 fire model. The newly incorporated fire induced land cover changes would influence ecosystem productivity and respiration as shown by carbon budget variables in Table 19. To be specific, the fire induced whole plant mortality and recovery would moderate the variations in ecosystem productivity and respiration of either autotrophic and heterotrophic species and further suppress fire induced NEP changes. The suppressed NEP change explains 52% of the total difference in simulated NEE changes.

Table 19 – Diagnosis of carbon budget variables in the data atmosphere driven RESFire-CRUNCEP and the default CLM-LL2013 fire simulations

Variables	RESFire-CRUNCEP			Li et al. [128]		
(Pg C/yr)	ΔFire	Fire on	Fire off	ΔFire	Fire on	Fire off
NEE	1.58	-2.67	-4.25	1.0	-0.1	-1.1
C_{fe}	2.08	2.08	0.0	1.9	1.9	0.0
$-NEP+C_{lh}$	-0.5	-4.75	-4.25	-0.9	-2.0	-1.1
NEP	0.5	4.8	4.3	0.8	3.0	2.3
NPP	0.4	61.7	61.3	-1.9	49.6	51.6
Rh	-0.1	56.9	57.0	-2.7	46.6	49.3
GPP	-0.1	142.3	142.4	-5.0	118.9	123.9
Ra	-0.5	80.6	81.1	-3.1	69.3	72.4
C_{lh}	0.0	0.05	0.05	-0.1	1.0	1.1

Similar with radiative forcing, we examined changes of the carbon budget variables in RCP4.5 future scenarios in Table 20. In general, the global burned area increases by 19% from the present-day scenario in CTRL1 (464±19Mha yr^{-1}) to the RCP4. 5 future scenario in CTRL2 (551±16Mha yr^{-1}). Accordingly, the annual averaged fire carbon emission increases by 100% from 2.5±0.1Pg C yr^{-1} at present to 5.0±0.3Pg C yr^{-1} in future. This increase is larger than the previous CLM modeling study of 25%~52% by *Kloster et al.* [162, 163], which might result from different climate sensitivity between RESFire and old CLM fire models. The carbon budget variables including GPP, NEP, and NEE increase by 4%, 7%, and 33%, respectively. These carbon variables affect terrestrial ecosystem productivity as well as fuel load supply for biomass burning. The complex climate-fire-ecosystem interactions will be discussed in the next section.

Table 20 – Comparisons of carbon budget variables in the sensitivity experiments of present-day and future scenarios

Variables	This work						Kloster et al. [162, 163]	
Time (scenario)	2000s (CTRL1)	2050s (CTRL2)	2000s (SENS1A)	2050s (SENS2A)	2000s (SENS1B)	2050s (SENS2B)	2000s	2050s
Burned Area (Mha/yr)	464±19	551±16 (↑19%)	437±17 (↓6%)	535±19 (↓3%)	458±18 (↓1%)	545±18 (↓1%)	176-330	–
Fire Carbon Emissions (Pg C/yr)	2.5±0.1	5.0±0.3 (↑100%)	–	–	–	–	2.0-2.4	2.7(↑25%)/ 3.4(↑52%)
GPP (Pg C/yr)	141±1.2	146±1.1 (↑4%)	143±1.0 (↑1%)	149±1.3 (↑2%)	142±1.5 (↑1%)	150±1.3 (↑3%)	–	–
NEP (Pg C/yr)	1.4±0.04	1.5±0.04 (↑7%)	1.4±0.04 (→0%)	1.6±0.04 (↑7%)	1.4±0.02 (→0%)	1.6±0.05 (↑7%)	–	–
NEE (Pg C/yr)	1.2±0.03	1.6±0.05 (↑33%)	1.2±0.02 (→0%)	1.6±0.05 (→0%)	1.2±0.02 (→0%)	1.6±0.05 (→0%)	–	–

5.2.3 Climate-Fire-Ecosystem Interactions

In the last section, we found a 19% increase of annual mean global burned area in the RCP4.5 future scenario compared to the present-day scenario. We examined the driving force and spatial distributions of this increase in Figure 40. The fuel load distribution shows heterogeneous changes with significant increases in boreal forest regions over Eurasia as well as rain forest regions in Africa and south American savanna and decreases in southeast Asia and Australia, while the fire spread distribution shows more clear patterns of increasing fire spread rates over middle- to high-latitude regions but decreasing fire spread rates over tropical regions. The burn area changes are mainly driven by fire weather changes as suggested by fire spread rates since the increasing and decreasing areas in

burned area resemble the spatial pattern in fire spread rate changes. In another word, fire weather changes dominate fire regime changes in future and determine the varying tendencies of burned intensity in each region.

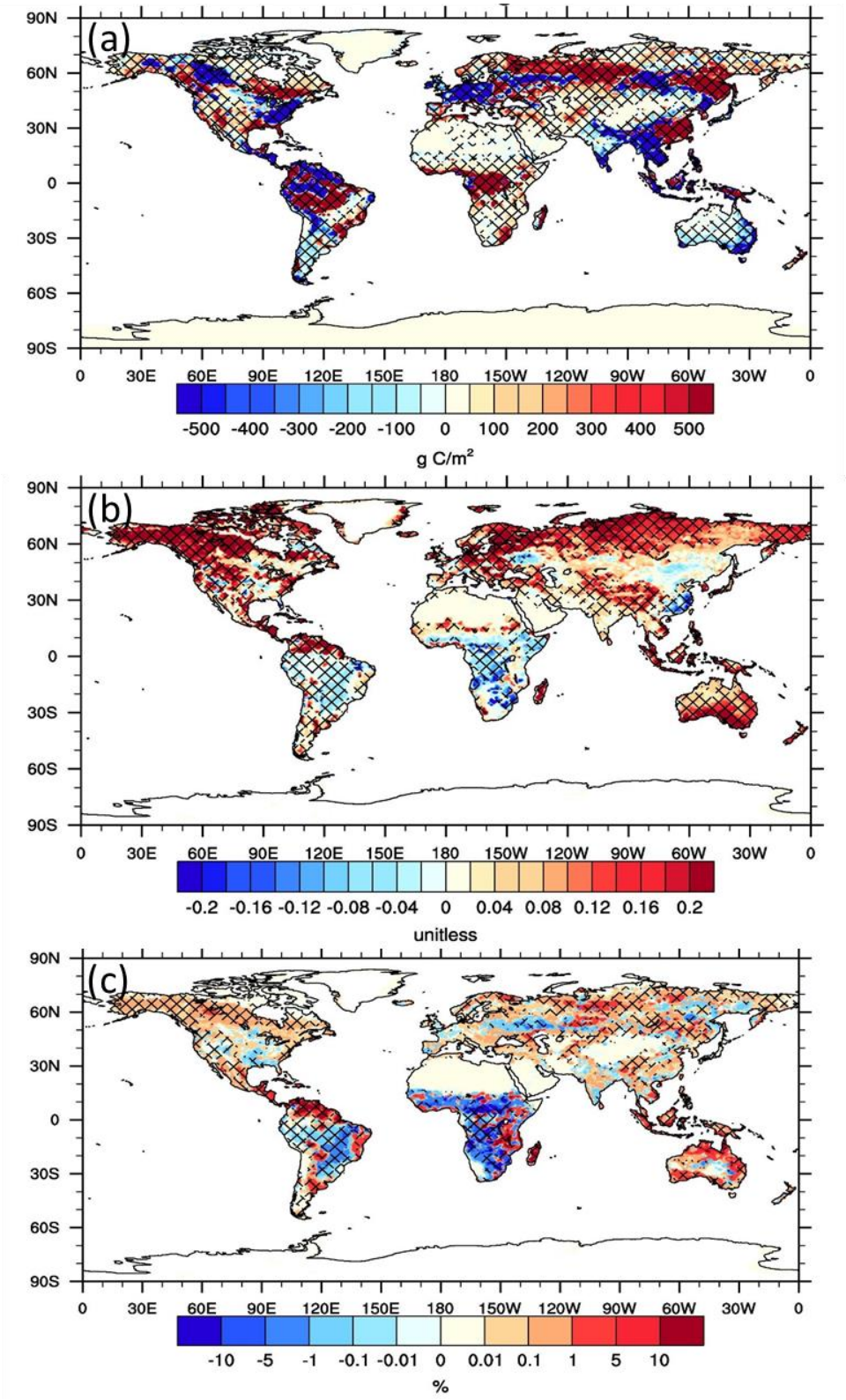
(a)
90N
60N
30N
0
30S
60S
90S
0 30E 60E 90E 120E 150E 180 150W 120W 90W 60W 30W 0
-500 -400 -300 -200 -100 0 100 200 300 400 500
g C/m²
(b)
90N
60N
30N
0
30S
60S
90S
0 30E 60E 90E 120E 150E 180 150W 120W 90W 60W 30W 0
-0.2 -0.16 -0.12 -0.08 -0.04 0 0.04 0.08 0.12 0.16 0.2
unitless
(c)
90N
60N
30N
0
30S
60S
90S
0 30E 60E 90E 120E 150E 180 150W 120W 90W 60W 30W 0
-10 -5 -1 -0.1 -0.01 0 0.01 0.1 1 5 10
%

Figure 40 – Changes in fire related variables between the RCP4.5 future scenario (CTRL2) and the present-day scenario (CTRL1). (a) changes in annual averaged fuel loads; (b) changes in annual averaged fire spread rate factors (FSF); (c) changes in annual averaged burned area; The net grids denote the 0.05 significance level.

To understand changes in specific fire weather variables, we compared the differences of fire aerosol AOD, surface temperature, and precipitation in Figure 41. Those regions with significantly increased burned areas also show enhanced fire aerosol AOD over boreal forest regions, southeast Asia, and downwind regions of central America. The enhanced AOD over these regions also reduce surface temperature in these regions while the other regions show neutral to positive surface temperature changes. The boreal forest region in north America show the strongest warming effect that may contribute to the large increases of biomass burning over this region. We also found suppressed precipitation over north America and southeast Asia, which also partly explain increasing tendencies of biomass burning over the same regions.

The examination of fire, ecosystem, and climate variables suggest different feedback mechanisms in their interactions. To quantify these distinct feedback pathways, we compared the sensitivity experiment results with the control runs and isolated direct and indirect feedback mechanisms in Figure 42. The comparison of the fire emission sensitivity experiments (CTRL2 vs SENS2A) suggests a positive feedback mechanism in that fire aerosol emissions tend to suppress precipitation in most regions (Figure 42a) and result in a 15.7Mha yr^{-1} increase in global burned area (Figure 42b). In the contrary, the comparison of fire induced land cover change experiments (SENS2A vs. SENS2B) suggests a negative feedback mechanism due to reduced fuel load supply with

consideration of fire induced LULCC. After the incorporation of fire disturbances on land cover, the global fuel load reduces in mang post-fire regions (Figure 42c) and leads to a 10.2Mha yr^{-1} decrease in global burned area (Figure 42d). The total interactive effect depends on the counteraction of these two contradictive feedback mechanisms, which increases the complexity of climate-fire-ecosystem interactions at regional and global scales.

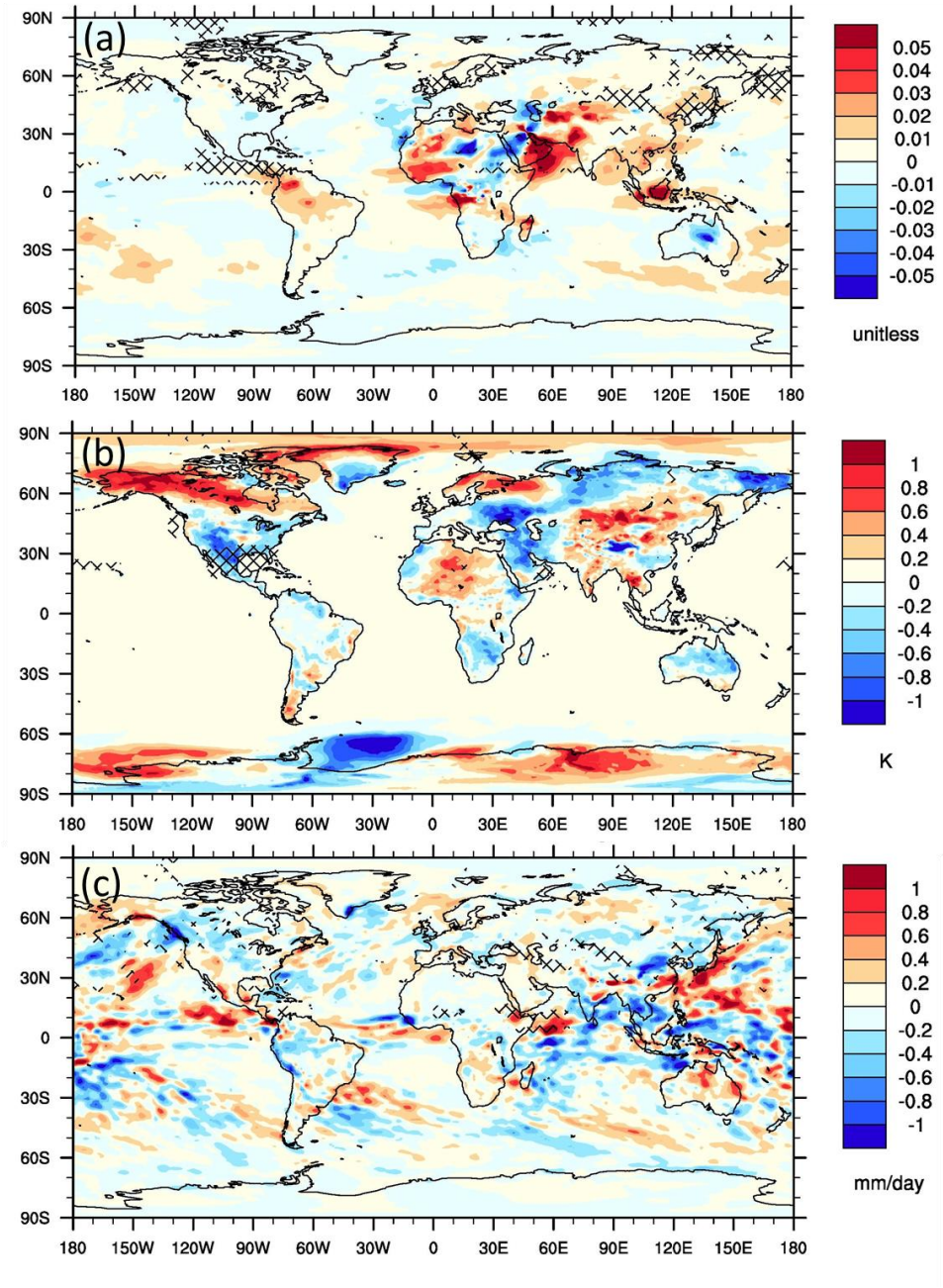

Figure 41 – Changes in annual averaged climate variables between the RCP4.5 future scenario (CTRL2) and the present-day scenario (CTRL1). (a) changes in column

AOD; (b) changes in surface temperature; (c) changes in precipitation rates; The net grids denote the 0.05 significance level.

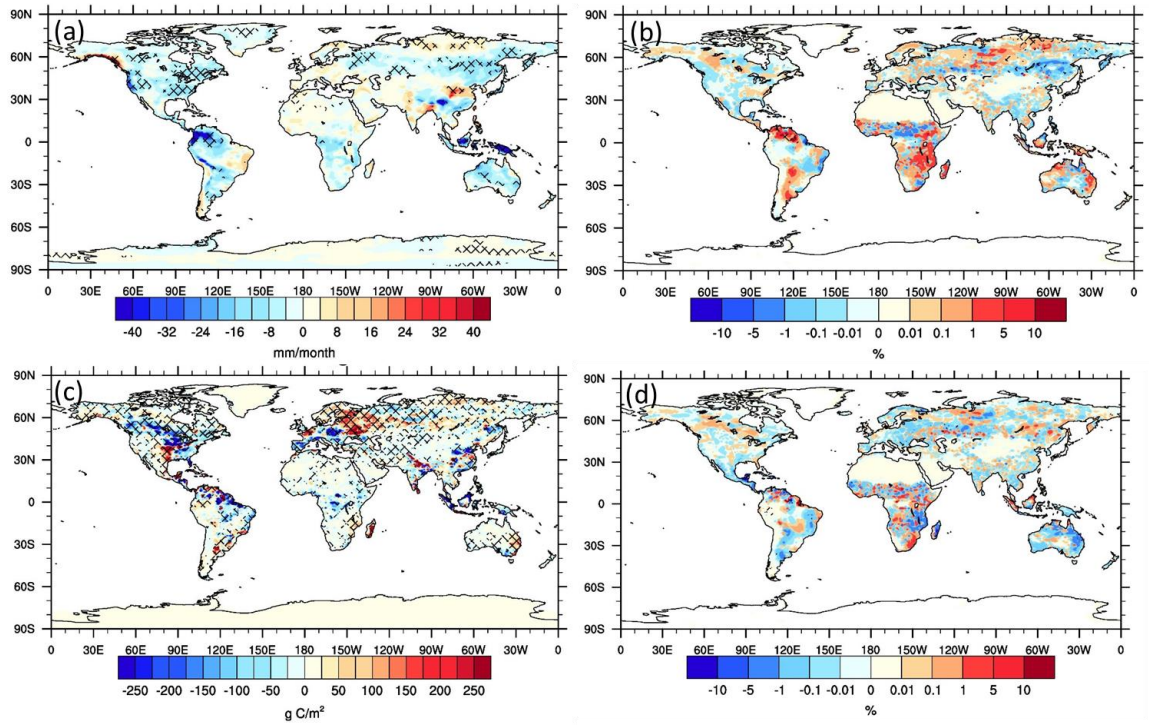

Figure 42 – Comparisons of climate-fire-ecosystem interactions in fire sensitivity experiments in the future scenario. (a) differences of 30-day running mean precipitation between fire emission sensitivity experiments (CTRL2-SENS2A); (b) same as (a) but for differences of annual mean burned area; (c) differences of fuel loads between fire induced land cover change sensitivity experiments (SENS2A-SENS2B); (d) same as (c) but for differences of annual mean burned area; The net grids denote the 0.05 significance level.

5.3 Conclusions and Discussion

In this chapter, we conducted series of fire modeling sensitivity and future prediction experiments with the consideration of different climate-fire-ecosystem feedback mechanisms. We evaluated the RESFire modeling performance in the context of radiative forcing and terrestrial carbon balance. We summarized the fire radiative forcing results for the present-day and the RCP4.5 future scenarios in Figure 43. We mainly considered fire induced radiative forcing changes related with fire aerosols and land cover changes. It's found that the fire radiative forcing increased from -0.94 ± 0.17 W/m^2 in 2000s to -1.38 ± 0.15 W/m^2 in 2050s, which was dominated by increased global biomass burning intensity and subsequent fire aerosol cloud radiative forcing changes. The global burned area and fire carbon emissions increased by 19% and 100%, respectively, with large amplification at boreal regions due to strong warming and enhanced fire spread rates. The fire aerosol emissions and fire induced land cover changes lead to contradictive feedback mechanisms in climate-fire-ecosystem interactions, manifesting a positive feedback induced by fire aerosol effects and a negative feedback related with fire induced land cover and fuel load changes. These two distinct feedback mechanisms competed with each other and increased the complexity of interactions among each component. We suggest more comprehensive examinations at regional scales to reveal these complex interactions for each fire-prone region. More evaluation metrics such as extreme values related with large wildfires should also be considered in the following studies to obtain a complete understanding of fire activities and their relationship with decadal climate change in future.

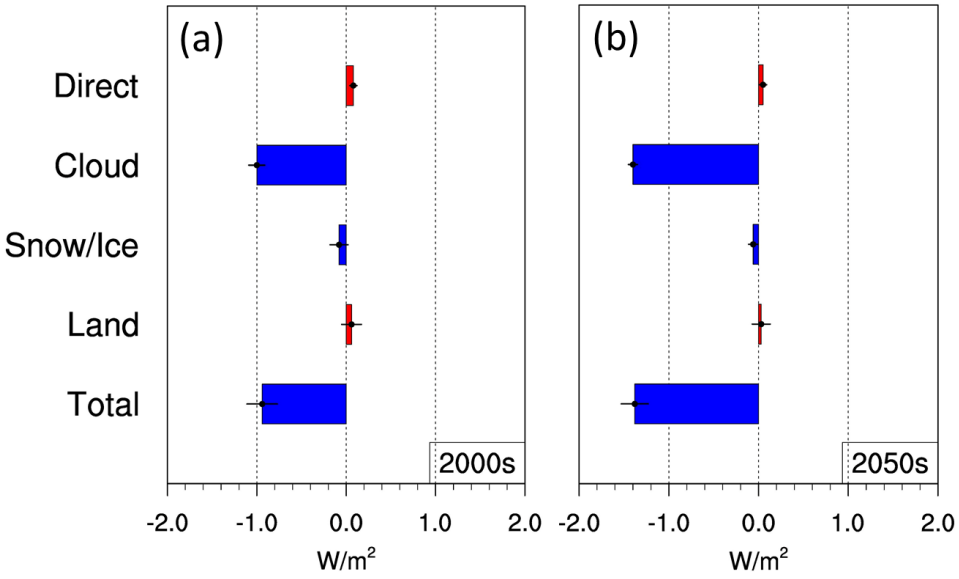

Figure 43 – Comparisons of fire related radiative forcing in (a) the present-day and (b) the RCP4.5 future simulations.

CHAPTER 6. CONCLUSIONS AND IMPLICATIONS

Here I summarized the major findings of all chapters and discussed the implications for relevant climate change and air pollution research. Some recommendations for future work are also listed in the end to encourage more follow-up studies.

6.1 Research Summaries

6.1.1 An Active Attempt to Understand the Impact of Climate Change on Regional Air Quality

The extraordinary severity of China's haze pollution in recent winters drew our close attention in the first place. I never saw such suffocating heavy smog in my several years' living experience in Beijing and other Chinese cities. It was believed that some kind of "tipping point" had been passed for both human society and climate systems. Preliminary results derived from pure meteorological variables corroborated these conjectures that the recent unfavorable weather conditions conducive to extreme haze were unprecedented in the past several decades. We tracked back much further than previous studies and tried to understand the role of climate change in these pollution extremes. Based on comprehensive statistical analysis and numerical modeling results, we concluded that the extreme haze pollution in recent winters was closely related with boreal cryosphere changes such as declining Arctic sea ice in preceding autumn and increasing Eurasia snow in early winter. These boreal cryosphere changes, especially the decreasing Arctic sea ice in autumn, modulated regional circulation to a large extent through perturbations on prominent teleconnection patterns in the Northern Hemisphere. Specifically, declining Arctic sea ice in autumn and early winter induced strong anomalous warming over the

Arctic and enhanced transient eddy forcing in the upper troposphere over the Atlantic Ocean during the following months. These changes tended to shift the East Atlantic teleconnection pattern to its positive phase, which further excited anomalous planetary wave propagation in downstream regions and altered near surface circulation with weakened east Asian winter monsoon activities. Suppressed monsoon winds finally attenuated atmosphere ventilation over eastern China and gave rise to severe haze pollution in concurrence with heave anthropogenic emissions of primary air pollutants and precursors in this region. Projections based on the 11 CMIP5 climate models also revealed exacerbating weather conditions with nearly tripled probability of extreme air stagnation by the end of the 21st century in the RCP8.5 future scenario. These findings have mixed implications for all stakeholders including the public, the Chinese government, and industry. They may serve as an easy excuse by the major polluters and environment regulators to absolve themselves from necessary responsibility for air pollution. They may also serve as a strong incentive for the Chinese government and the public to promote more stringent pollution reduction and more clean energy utilization. Since we have entered an era of rapid climate change, we are experiencing more and more influences of climate change on daily life, and we will witness people's choice of how to cope with those great challenges for the future.

6.1.2 A Productive Progress to Improve Fire Modelling Capability in the Earth System Model

The fire model development practice is another attempt to tackle the complex system problem with multiple components and intriguing interactions. This time we not only evaluated the impact of climate change on fire activities but also considered fire

feedback to the climate systems. This is a more integrated example of how climate change interacts with air pollution cases such as wildfires. We improved the modeling capability of fire occurrence, fire spread, and fire impacts in the RESFire model with satisfactory performance in different simulation modes. The RESFire model showed robust fire modelling performance driven by either offline reanalysis-observation combined atmosphere data or online CAM5 simulated atmosphere data, which laid the foundation of future prediction studies. The newly incorporated fire impact module also completed the feedback pathways between fire activities and the climate systems and enabled two-way interactive modelling studies. Based on the RESFire numerical prediction experiments in Chapter 5, we found 19% increases in global burned area and 100% increases in fire carbon emissions in the middle 21st century under the RCP4.5 moderate emission scenario. These changes lead to more than 40% enhancement of fire aerosol radiative forcing, which is dominated by fire aerosol cloud radiative forcing changes. We also analysed the sensitivity experiments and proposed two competitive feedback pathways of fire activities, a positive feedback related to fire aerosol suppressed precipitation and a negative feedback related to fire induced land use change and fuel supply reduction. All these results demonstrate the effectiveness of the RESFire model and the latest development in interactive climate-fire-ecosystem modelling studies, which are essential for a clear understanding of decadal climate variability.

6.2 Future Work

6.2.1 Climatic Extreme Event Attribution

The great complexity in the climate system and the air pollution problem themselves limits our insight into the connections from remote boreal cryosphere changes to regional haze pollution. Such connections transmit through too long chains to generate a clear and easy-to-understand signal. The answer to the problem also requires

interdisciplinary knowledge given its transdisciplinary characteristics. Here I list suggestions for follow-up studies to uncover more details in the teleconnection relationship:

(1) More sensitivity experiments should be designed and conducted to understand climate impacts of declining Arctic sea ice in different seasons at sub-regional scales. Previous studies have suggested high nonlinearity in atmosphere responses to Arctic sea ice forcing with quite different responses to regional sea ice losses from pan-Arctic sea ice loss [198]. More climate forcing factors such as SST changes in specific regions should also be examined carefully for a comprehensive understanding of climate change effects.

(2) Besides forcing factors, more connections with other potential responses can be built based on current observational datasets and numerical modeling results. Arctic warming has been linked to several observed vegetational changes in boreal regions such as Eurasian Arctic greening in recent decades [199-201]. These changing biomes may reshape local ecosystem productivity and biomass fuel conditions and further interplay with local fire activities. Fire emissions like GHGs and carbonaceous aerosols also show strong impacts on Arctic climate change. It is an interesting question that how would melting Arctic sea ice and increasing fire activities interact with each other in a warming world. We can integrate the two problems in this work together by answering the above question.

6.2.2 Fire Model Development and Application

Data availability was a major limiting factor in the fire model development to representing complex interaction processes. Despite the advances of fire modeling in global models made in this work, there are several areas that future fire model development should consider:

(1) Large uncertainties in fuel load and emission factors would undermine the accuracy of fire emission products. Figure 36 compares the CLM fuel load simulation against 176 *in-situ* measurements worldwide [202]. The comparison results reveal generally well modeled biomass fuel, though some discrepancies are still appreciable in regions such as western North America. Reducing fuel load biases and emission factor uncertainties would better complement the improved burned area simulation in the fire model;

(2) More detailed burning process parameterization is needed to simulate different fire combustion stages. It is known that flaming and smoldering are two burning stages that have very different emission characteristics. Such emission features will determine fire emission species, timing, and transportation and improve the model simulations of more complete fire gaseous and particulate emissions (such as brown carbon from biomass burning) and their effects on weather and climate.

(3) Fire impact parameterization for fire induced plant mortality and regrowth can be improved by including multiple plant properties such as tree species, stem size, and bark thickness. The detailed vegetation demographic information under the PFT-based modeling structure would further improve the modeling capability of regional differences in fire disturbance and ecosystem responses. Approaches such

as “cohorts” by aggregating plant individuals with similar size, type, and successional status [203] will further improve the fire model;

(4) More fire related observations for plant mortality and recovery are needed to improve fire impact simulations by considering variable recovery rates and interspecies competition. Integration of the fire model with DGVMs will be needed to fully reproduce fire-vegetation dynamics in the model.

APPENDIX A. AUXILURY MATERIALS

This appendix includes a summary of statistical metrics used in the ILAMBv2 benchmark system [155] for evaluation of the fire simulation performance in Chapter 4.

A.1 Metrics in the ILAMBv2 Benchmark System

A.1.1 Global Bias Metric

$$M_i = 1 - \left| \frac{AM_{mod,i} - AM_{obs,i}}{AM'_{obs,i}} \right| \tag{45}$$

$$M'_i = e^{M_i}/e \tag{46}$$

$$AM'_{obs,i} = AM_{obs,j} - \min(AM_{obs}) \times FC \tag{47}$$

$$M = \frac{\sum_{i=1}^{ncells} M'_i \times A_i \times M_{obs,i}}{\sum_{i=1}^{ncells} A_i \times M_{obs,i}} \tag{48}$$

ILAMBv2 uses Equations 45-48 to calculate global bias metric score M_i at ith grid cell and its global mean M with mass weighting, respectively. $AM_{mod,i}$and $AM_{obs,i}$ are annual mean of the model and the observation at ith grid cell, separately. FC is a factor coefficient to force $AM'_{obs,i}$ being positive everywhere. A_i is the area for ith grid cell. $M_{obs,i}$is adjusted mass ($AM'_{mod,i}$) for mass weighting to calculate global mean score M. *ncells* is the number of all land grid cells where observation data is available.

A.1.2 Root Mean Square Error (RMSE) Metric

$$M_i = 1 - \frac{RMSE_i}{\Phi_{obs,i}} \tag{49}$$

$$M_i' = e^{M_i}/e \tag{50}$$

$$AM_{obs,i}' = AM_{obs,j} - \min(AM_{obs}) \times FC \tag{51}$$

$$M = \frac{\sum_{i=1}^{ncells} M_i' \times A_i \times M_{obs,i}}{\sum_{i=1}^{ncells} A_i \times M_{obs,i}} \tag{52}$$

ILAMBv2 uses Equations 49-52 to calculate root mean square error metric score M_i at i[th] grid cell and its global mean M, respectively. Where $\Phi_{obs,i}$ is the root mean square for monthly mean annual cycle of the observation at i[th] grid cell, and $RMSE_i$ is the root mean square error between model and observation. $AM_{obs,i}$ is annual mean of the observation at i[th] grid cell. *FC* is a factor coefficient to force $AM_{obs,i}'$ being positive everywhere. $M_{obs,i}$is adjusted mass ($AM_{mod,i}'$) for mass weighting to calculate global mean score *M*. *ncells* is the number of all land grid cells where observation data is available. This metric is used to compare magnitude and phase difference of the monthly mean annual cycle between the model and the observation.

A.1.3 Spatial Distribution Metric

$$M = \frac{4(1+R)}{(\sigma_f + 1/\sigma_f)^2(1+R_0)} \tag{53}$$

ILAMBv2 uses Equation 53 to calculate spatial distribution metric score M. R is the spatial correlation coefficient of the annual mean between model and observation. R_0

is their ideal maximum correlation. Here, we set R_0 equal to 1 for all models. σ_f is ratio for standard deviation of model to that of observation (Taylor, 2001). This metric is used to compare magnitude and spatial pattern of annual mean of model with observation.

A.1.4 Seasonal Cycle Phase Metric (BA)

$$M_i = (1 + cos\vartheta_i)/2 \tag{54}$$

$$AM'_{obs,i} = AM_{obs,j} - \min(AM_{obs}) \times FC \tag{55}$$

$$M = \frac{\sum_{i=1}^{ncells} M'_i \times A_i \times M_{obs,i}}{\sum_{i=1}^{ncells} A_i \times M_{obs,i}} \tag{56}$$

ILAMBv2 uses Equations 54-56 to calculate seasonal cycle phase metric score M_i at ith grid cell and its global mean M, respectively. ϑ_i is the difference of the angle between the month of the maximum value for the model and that for the observation at ith grid cell. $AM_{obs,j}$ is annual mean of the observation at ith grid cell. FC is factor coefficient to force $AM'_{obs,i}$ being positive everywhere. . $M_{obs,i}$is adjusted mass ($AM'_{mod,i}$) for mass weighting to calculate global mean score *M*. *ncells* is the number of all land grid cells where observation data is available. This metric is used to compare phase difference of the monthly mean annual cycle between the model and the observation.

A.1.5 Interannual Variability Metric

$$M_i = 1 - \left| \frac{\sigma_{mod,i} - \sigma_{obs,i}}{\sigma_{obs,i}} \right| \tag{57}$$

$$M_i' = e^{M_i}/e \tag{58}$$

$$AM_{obs,i}' = AM_{obs,j} - \min(AM_{obs}) \times FC \tag{59}$$

$$M = \frac{\sum_{i=1}^{ncells} M_i' \times A_i \times M_{obs,i}}{\sum_{i=1}^{ncells} A_i \times M_{obs,i}} \tag{60}$$

ILAMBv2 uses Equations 57-60 to calculate interannual variability metric score M_i at i[th] grid cell and its global mean M, respectively. $\sigma_{mod,i}$ and $\sigma_{obs,i}$ are standard deviation at i[th] grid cell for model and observation. $AM_{obs,j}$ is annual mean of the observation at i[th] grid cell. FC is factor coefficient to force $AM_{obs,i}'$ being positive everywhere. $M_{obs,i}$is adjusted mass ($AM_{mod,i}'$) for mass weighting to calculate global mean score *M*. *ncells* is the number of all land grid cells where observation data is available. This metric is used to compare interannual variability of specific variables between the model and the observation.

A.1.6 Overall Score Metric

ILAMBv2 calculates a couple sets of overall scores in this diagnostic package, one for individual variable (G1), one for all variables mean (G2), one for all variable to variable relationships mean (G3), and the last one (G4) for the overall score combined both G2 and G3. ILAMBv2 uses unequally weighting functions to calculate G1 and G2, while it uses simply straight averaging to calculate G3 and G4. G4 is the final score for each model. Please refer to Table 2 of the support information in *Luo et al.* [155] for detailed information of the rule system for scoring system.

REFERENCES

1. Environment Protection Authority, N., *NSW State of the Environment 2000*, in *State of the Environment*. 2000, NSW Environment Protection Authority: Sydney, Australia.

2. Kan, H.D., R.J. Chen, and S.L. Tong, *Ambient air pollution, climate change, and population health in China.* Environment International, 2012. **42**: p. 10-19.

3. Nel, A., *Air pollution-related illness: Effects of particles.* Science, 2005. **308**(5723): p. 804-806.

4. Xie, Y., et al., *Economic Impacts from PM2.5 Pollution-Related Health Effects in China: A Provincial-Level Analysis.* Environmental Science & Technology, 2016. **50**(9): p. 4836-4843.

5. Li, B.G., et al., *The contribution of China's emissions to global climate forcing.* Nature, 2016. **531**(7594): p. 357-+.

6. Wang, Y.S., et al., *The Current Status, Opportunity, and Challenges of Air Pollution Control in Beijing.* Bulletin of Chinese Academy of Sciences, 2016. **31**(9): p. 6.

7. Jacob, D.J. and D.A. Winner, *Effect of climate change on air quality.* Atmospheric Environment, 2009. **43**(1): p. 51-63.

8. Zhang, Q., et al., *Transboundary health impacts of transported global air pollution and international trade.* Nature, 2017. **543**(7647): p. 705-+.

9. He, K., et al., *A Review of Air Pollution Control in Beijing: 1998-2013*. 2016, United Nations Environment Programme (UNEP): Nairobi, Kenya.

10. Sun, Y.L., et al., *Primary and secondary aerosols in Beijing in winter: sources, variations and processes.* Atmospheric Chemistry and Physics, 2016. **16**(13): p. 8309-8329.

11. Liu, J., et al., *Air pollutant emissions from Chinese households: A major and underappreciated ambient pollution source.* Proceedings of the National Academy of Sciences of the United States of America, 2016. **113**(28): p. 7756-7761.

12. Lin, J., et al., *Recent Changes in Particulate Air Pollution over China Observed from Space and the Ground: Effectiveness of Emission Control.* Environmental Science & Technology, 2010. **44**(20): p. 7771-7776.

13. Ma, Q.A., et al., *Impacts of coal burning on ambient PM2.5 pollution in China.* Atmospheric Chemistry and Physics, 2017. **17**(7): p. 4477-4491.

14. Huang, R.J., et al., *High secondary aerosol contribution to particulate pollution during haze events in China.* Nature, 2014. **514**(7521): p. 218-222.

15. Wang, G.H., et al., *Persistent sulfate formation from London Fog to Chinese haze.* Proceedings of the National Academy of Sciences of the United States of America, 2016. **113**(48): p. 13630-13635.

16. Niu, F., et al., *Increase of wintertime fog in China: Potential impacts of weakening of the Eastern Asian monsoon circulation and increasing aerosol loading.* Journal of Geophysical Research-Atmospheres, 2010. **115**.

17. Jia, B., et al., *A new indicator on the impact of large-scale circulation on wintertime particulate matter pollution over China.* Atmospheric Chemistry and Physics, 2015. **15**(20): p. 11919-11929.

18. Zou, Y.F., et al., *Arctic sea ice, Eurasia snow, and extreme winter haze in China.* Science Advances, 2017. **3**(3).

19. Cai, W.J., et al., *Weather conditions conducive to Beijing severe haze more frequent under climate change.* Nature Climate Change, 2017. **7**(4): p. 257-+.

20. Wang, H.J. and H.P. Chen, *Understanding the recent trend of haze pollution in eastern China: roles of climate change.* Atmospheric Chemistry and Physics, 2016. **16**(6): p. 4205-4211.

21. Wang, B., et al., *Another Look at Interannual-to-Interdecadal Variations of the East Asian Winter Monsoon: The Northern and Southern Temperature Modes.* Journal of Climate, 2010. **23**(6): p. 1495-1512.

22. Lin, C.G., et al., *Observed Coherent Trends of Surface and Upper-Air Wind Speed over China since 1960.* Journal of Climate, 2013. **26**(9): p. 2891-2903.

23. Taylor, K.E., R.J. Stouffer, and G.A. Meehl, *An Overview of Cmip5 and the Experiment Design.* Bulletin of the American Meteorological Society, 2012. **93**(4): p. 485-498.

24. Horton, D.E., et al., *Occurrence and persistence of future atmospheric stagnation events.* Nature Climate Change, 2014. **4**(8): p. 698-703.

25. Pithan, F. and T. Mauritsen, *Arctic amplification dominated by temperature feedbacks in contemporary climate models.* Nature Geoscience, 2014. **7**(3): p. 181-184.

26. Serreze, M.C. and R.G. Barry, *Processes and impacts of Arctic amplification: A research synthesis.* Global and Planetary Change, 2011. **77**(1-2): p. 85-96.

27. Cohen, J., et al., *Recent Arctic amplification and extreme mid-latitude weather.* Nature Geoscience, 2014. **7**(9): p. 627-637.

28. Bowman, D.M.J.S., et al., *Fire in the Earth System.* Science, 2009. **324**(5926): p. 481-484.

29. Flannigan, M.D., et al., *Implications of changing climate for global wildland fire.* International Journal of Wildland Fire, 2009. **18**(5): p. 483-507.

30. Veraverbeke, S., et al., *Lightning as a major driver of recent large fire years in North American boreal forests.* Nature Climate Change, 2017. **7**(7): p. 529-+.

31. Andela, N. and G.R. van der Werf, *Recent trends in African fires driven by cropland expansion and El Nino to La Nina transition.* Nature Climate Change, 2014. **4**(9): p. 791-795.

32. Field, R.D., et al., *Indonesian fire activity and smoke pollution in 2015 show persistent nonlinear sensitivity to El Nino-induced drought.* Proceedings of the National Academy of Sciences of the United States of America, 2016. **113**(33): p. 9204-9209.

33. Chen, Y., et al., *Forecasting Fire Season Severity in South America Using Sea Surface Temperature Anomalies.* Science, 2011. **334**(6057): p. 787-791.

34. Heilman, W.E., et al., *Wildland fire emissions, carbon, and climate: Plume transport, and chemistry processes.* Forest Ecology and Management, 2014. **317**: p. 70-79.

35. Liu, Y.Q., S. Goodrick, and W. Heilman, *Wildland fire emissions, carbon, and climate: Wildfire-climate interactions.* Forest Ecology and Management, 2014. **317**: p. 80-96.

36. Lu, Z. and I.N. Sokolik, *The effect of smoke emission amount on changes in cloud properties and precipitation: A case study of Canadian boreal wildfires of 2007.* Journal of Geophysical Research-Atmospheres, 2013. **118**(20): p. 11777-11793.

37. Keeley, J.E., *Fire intensity, fire severity and burn severity: a brief review and suggested usage.* International Journal of Wildland Fire, 2009. **18**(1): p. 116-126.

38. Brando, P.M., et al., *Abrupt increases in Amazonian tree mortality due to drought-fire interactions.* Proceedings of the National Academy of Sciences of the United States of America, 2014. **111**(17): p. 6347-6352.

39. Gatti, L.V., et al., *Drought sensitivity of Amazonian carbon balance revealed by atmospheric measurements.* Nature, 2014. **506**(7486): p. 76-+.

40. Knorr, W., et al., *Wildfire air pollution hazard during the 21st century.* Atmos. Chem. Phys., 2017. **17**(14): p. 9223-9236.

41. Johnston, F.H., et al., *Estimated Global Mortality Attributable to Smoke from Landscape Fires.* Environmental Health Perspectives, 2012. **120**(5): p. 695-701.

42. Marlier, M.E., et al., *El Nino and health risks from landscape fire emissions in southeast Asia.* Nature Climate Change, 2013. **3**(2): p. 131-136.

43. Marlon, J.R., et al., *Wildfire responses to abrupt climate change in North America.* Proceedings of the National Academy of Sciences of the United States of America, 2009. **106**(8): p. 2519-2524.

44. Pechony, O. and D.T. Shindell, *Driving forces of global wildfires over the past millennium and the forthcoming century.* Proceedings of the National Academy of Sciences of the United States of America, 2010. **107**(45): p. 19167-19170.

45. Westerling, A.L., et al., *Warming and earlier spring increase western US forest wildfire activity.* Science, 2006. **313**(5789): p. 940-943.

46. Yang, J., et al., *A growing importance of large fires in conterminous United States during 1984-2012.* Journal of Geophysical Research-Biogeosciences, 2015. **120**(12): p. 2625-2640.

47. Bowman, D.M.J.S., et al., *The human dimension of fire regimes on Earth.* Journal of Biogeography, 2011. **38**(12): p. 2223-2236.

48. Archibald, S., A.C. Staver, and S.A. Levin, *Evolution of human-driven fire regimes in Africa.* Proceedings of the National Academy of Sciences of the United States of America, 2012. **109**(3): p. 847-852.

49. Yang, J., et al., *Spatial and temporal patterns of global burned area in response to anthropogenic and environmental factors: Reconstructing global fire history for the 20th and early 21st centuries.* Journal of Geophysical Research-Biogeosciences, 2014. **119**(3): p. 249-263.

50. Andela, N., et al., *A human-driven decline in global burned area.* Science, 2017. **356**(6345): p. 1356-1361.

51. Ichoku, C. and L. Ellison, *Global top-down smoke-aerosol emissions estimation using satellite fire radiative power measurements.* Atmospheric Chemistry and Physics, 2014. **14**(13): p. 6643-6667.

52. Kaiser, J.W., et al., *Biomass burning emissions estimated with a global fire assimilation system based on observed fire radiative power.* Biogeosciences, 2012. **9**(1): p. 527-554.

53. Randerson, J.T., et al., *Global burned area and biomass burning emissions from small fires.* Journal of Geophysical Research-Biogeosciences, 2012. **117**.

54. van der Werf, G.R., et al., *Global fire emissions and the contribution of deforestation, savanna, forest, agricultural, and peat fires (1997–2009).* Atmos. Chem. Phys., 2010. **10**(23): p. 11707-11735.

55. van der Werf, G.R., et al., *Global fire emissions estimates during 1997–2015.* Earth Syst. Sci. Data Discuss., 2017. **2017**: p. 1-43.

56. Myhre, G., D. Shindell, F.-M. Bréon, W. Collins, J. Fuglestvedt, J. Huang, D. Koch, J.-F. Lamarque, D. Lee, B. Mendoza, T. Nakajima, A. Robock, G. Stephens, T. Takemura and H. Zhang, *Anthropogenic and Natural Radiative Forcing. In: Climate Change 2013: The Physical Science Basis*, in *Contribution of Working Group I to the Fifth Assessment Report of the Intergovernmental Panel on Climate Change* T.F. Stocker, D. Qin, G.-K. Plattner, M. Tignor, S.K. Allen, J. Boschung, A. Nauels, Y. Xia, V. Bex and P.M. Midgley, Editor. 2013: Cambridge, United Kingdom and New York, NY, USA.

57. Randerson, J.T., et al., *The impact of boreal forest fire on climate warming.* Science, 2006. **314**(5802): p. 1130-1132.

58. Yue, X., et al., *Ensemble projections of wildfire activity and carbonaceous aerosol concentrations over the western United States in the mid-21st century.* Atmospheric Environment, 2013. **77**: p. 767-780.

59. Hantson, S., et al., *The status and challenge of global fire modelling.* Biogeosciences, 2016. **13**(11): p. 3359-3375.

60. Running, S.W., *Climate change - Ecosystem disturbance, carbon, and climate.* Science, 2008. **321**(5889): p. 652-653.

61. Kelley, D.I., S.P. Harrison, and I.C. Prentice, *Improved simulation of fire-vegetation interactions in the Land surface Processes and eXchanges dynamic global vegetation model (LPX-Mv1).* Geoscientific Model Development, 2014. **7**(5): p. 2411-2433.

62. Rogers, B.M., et al., *Influence of tree species on continental differences in boreal fires and climate feedbacks.* Nature Geoscience, 2015. **8**(3): p. 228-234.

63. Ward, D.S., et al., *The changing radiative forcing of fires: global model estimates for past, present and future.* Atmospheric Chemistry and Physics, 2012. **12**(22): p. 10857-10886.

64. China, t.S.C.o.t.P.s.R.o. *Notice on the air pollution prevention and control action plan*. 2013 [cited 2017 07/23]; Available from: http://www.gov.cn/zwgk/2013-09/12/content_2486773.htm.

65. Centre, C.N.E.M., *Monthly Air Quality Report in 74 Chinese Cities in January 2013*. 2013: http://www.cnemc.cn/publish/totalWebSite/news/news_33891.html.

66. Gao, M., et al., *Health impacts and economic losses assessment of the 2013 severe haze event in Beijing area.* Science of the Total Environment, 2015. **511**: p. 553-561.

67. Zhao, C., Y.H. Wang, and T. Zeng, *East China Plains: A "Basin" of Ozone Pollution.* Environmental Science & Technology, 2009. **43**(6): p. 1911-1915.

68. Wilks, D.S., *Canonical Correlation Analysis*, in *Statistical Methods in the Atmospheric Sciences*. 2011, Academic Press: Oxford: Waltham, MA. p. 580-581.

69. Wilks, D.S., *Principal Component (EOF) Analysis*, in *Statistical Methods in the Atmospheric Sciences*. 2011, Academic Press: Oxford: Waltham, MA. p. 519-525.

70. Grinsted, A., J.C. Moore, and S. Jevrejeva, *Application of the cross wavelet transform and wavelet coherence to geophysical time series.* Nonlinear Processes in Geophysics, 2004. **11**(5-6): p. 561-566.

71. Wang, K.C., R.E. Dickinson, and S.L. Liang, *Clear Sky Visibility Has Decreased over Land Globally from 1973 to 2007.* Science, 2009. **323**(5920): p. 1468-1470.

72. Remer, L.A., et al., *The MODIS aerosol algorithm, products, and validation.* Journal of the Atmospheric Sciences, 2005. **62**(4): p. 947-973.

73. Qu, W.J., et al., *Spatial distribution and interannual variation of surface PM10 concentrations over eighty-six Chinese cities.* Atmospheric Chemistry and Physics, 2010. **10**(12): p. 5641-5662.

74. Kalnay, E., et al., *The NCEP/NCAR 40-year reanalysis project.* Bulletin of the American Meteorological Society, 1996. **77**(3): p. 437-471.

75. Dee, D.P., et al., *The ERA-Interim reanalysis: configuration and performance of the data assimilation system.* Quarterly Journal of the Royal Meteorological Society, 2011. **137**(656): p. 553-597.

76. Zhu, Y.F., *An Index of East Asian Winter Monsoon Applied to the Description of China's Mainland Winter Temperature Changes.* Acta Meteorologica Sinica, 2008. **22**(4): p. 522-529.

77. Jhun, J.G. and E.J. Lee, *A new East Asian winter monsoon index and associated characteristics of the winter monsoon.* Journal of Climate, 2004. **17**(4): p. 711-726.

78. Li, Y.Q. and S. Yang, *A Dynamical Index for the East Asian Winter Monsoon.* Journal of Climate, 2010. **23**(15): p. 4255-4262.

79. Thompson, D.W.J. and J.M. Wallace, *The Arctic Oscillation signature in the wintertime geopotential height and temperature fields.* Geophysical Research Letters, 1998. **25**(9): p. 1297-1300.

80. Wolter, K. and M.S. Timlin, *Measuring the strength of ENSO - how does 1997/98 rank?* Weather, 1998. **53**: p. 315-324.

81. Rayner, N.A., et al., *Global analyses of sea surface temperature, sea ice, and night marine air temperature since the late nineteenth century.* Journal of Geophysical Research-Atmospheres, 2003. **108**(D14).

82. Robinson, D.A., K.F. Dewey, and R.R. Heim, *Global Snow Cover Monitoring - an Update.* Bulletin of the American Meteorological Society, 1993. **74**(9): p. 1689-1696.

83. Wilks, D.S., *Statistical methods in the atmospheric sciences*. 3rd ed. International geophysics series. 2011, Waltham, MA: Academic Press, Oxford 676.

84. Porter, W.C., et al., *Investigating the observed sensitivities of air-quality extremes to meteorological drivers via quantile regression.* Atmospheric Chemistry and Physics, 2015. **15**(18): p. 10349-10366.

85. Kim, S.-J., et al., *L1 trend filtering.* SIMA review, 2007.

86. Dawson, J.P., P.J. Adams, and S.N. Pandis, *Sensitivity of PM2.5 to climate in the Eastern US: a modeling case study.* Atmospheric Chemistry and Physics, 2007. **7**(16): p. 4295-4309.

87. Fekedulegn, B.D., et al., *Coping with multicollinearity: An example on application of principal components regression in dendroecology*. 2002, U.S. Department of Agriculture, Forest Service, Northeastern Research Station: Newton Square, PA.

88. Barnston, A.G. and R.E. Livezey, *Classification, Seasonality and Persistence of Low-Frequency Atmospheric Circulation Patterns.* Monthly Weather Review, 1987. **115**(6): p. 1083-1126.

89. Hurrell, J.W., et al., *The Community Earth System Model A Framework for Collaborative Research.* Bulletin of the American Meteorological Society, 2013. **94**(9): p. 1339-1360.

90. Neale, R.B., et al., *Description of the NCAR Community Atmosphere Model (CAM 5.0),* in *Technical Note*. 2013, NCAR p. 289.

91. Marsh, D.R., et al., *Climate Change from 1850 to 2005 Simulated in CESM1(WACCM).* Journal of Climate, 2013. **26**(19): p. 7372-7391.

92. Peings, Y. and G. Magnusdottir, *Role of sea surface temperature, Arctic sea ice and Siberian snow in forcing the atmospheric circulation in winter of 2012-2013.* Climate Dynamics, 2015. **45**(5-6): p. 1181-1206.

93. Brown, R.D. and B. Brasnett, *Canadian Meteorological Centre (CMC) Daily Snow Depth Analysis Data*, in *updated annually*, C.M. Centre, Editor. 2014, NASA National Snow and Ice Data Center Distributed Active Archive Center: Boulder, Colorado USA.

94. Gong, G., et al., *Sensitivity of atmospheric response to modeled snow anomaly characteristics.* Journal of Geophysical Research-Atmospheres, 2004. **109**(D6).

95. Peings, Y., D. Saint-Martin, and H. Douville, *A Numerical Sensitivity Study of the Influence of Siberian Snow on the Northern Annular Mode.* Journal of Climate, 2012. **25**(2): p. 592-607.

96. Coles, S., *An Introduction to Statistical Modeling of Extreme Values*. Springer Series in Statistics. 2001, https://www.mathworks.com/help/stats/generalized-extreme-value-distribution.html: Springer.

97. Trenberth, K.E., *An Assessment of the Impact of Transient Eddies on the Zonal Flow during a Blocking Episode Using Localized Eliassen-Palm Flux Diagnostics.* Journal of the Atmospheric Sciences, 1986. **43**(19): p. 2070-2087.

98. Lau, N.C. and E.O. Holopainen, *Transient Eddy Forcing of the Time-Mean Flow as Identified by Geopotential Tendencies.* Journal of the Atmospheric Sciences, 1984. **41**(3): p. 313-328.

99. Takaya, K. and H. Nakamura, *A formulation of a phase-independent wave-activity flux for stationary and migratory quasigeostrophic eddies on a zonally varying basic flow.* Journal of the Atmospheric Sciences, 2001. **58**(6): p. 608-627.

100. Davis, C.A., *A Potential-Vorticity Diagnosis of the Importance of Initial Structure and Condensational Heating in Observed Extratropical Cyclogenesis.* Monthly Weather Review, 1992. **120**(11): p. 2409-2428.

101. Horton, D.E., et al., *Contribution of changes in atmospheric circulation patterns to extreme temperature trends.* Nature, 2015. **522**(7557): p. 465-+.

102. Honda, M., J. Inoue, and S. Yamane, *Influence of low Arctic sea-ice minima on anomalously cold Eurasian winters.* Geophysical Research Letters, 2009. **36**.

103. Peings, Y. and G. Magnusdottir, *Response of the Wintertime Northern Hemisphere Atmospheric Circulation to Current and Projected Arctic Sea Ice Decline: A Numerical Study with CAM5.* Journal of Climate, 2014. **27**(1): p. 244-264.

104. Mori, M., et al., *Robust Arctic sea-ice influence on the frequent Eurasian cold winters in past decades.* Nature Geoscience, 2014. **7**(12): p. 869-873.

105. Brown, R.D., *Northern hemisphere snow cover variability and change, 1915-97.* Journal of Climate, 2000. **13**(13): p. 2339-2355.

106. Liu, J.P., et al., *Impact of declining Arctic sea ice on winter snowfall.* Proceedings of the National Academy of Sciences of the United States of America, 2012. **109**(11): p. 4074-4079.

107. Cohen, J., et al., *Stratosphere–Troposphere Coupling and Links with Eurasian Land Surface Variability.* Journal of Climate, 2009. **20**(21): p. 5335-5343.

108. Deser, C., et al., *Does ocean coupling matter for the northern extratropical response to projected Arctic sea ice loss?* Geophysical Research Letters, 2016. **43**(5): p. 2149-2157.

109. Hoskins, B.J., I.N. James, and G.H. White, *The Shape, Propagation and Mean-Flow Interaction of Large-Scale Weather Systems.* Journal of the Atmospheric Sciences, 1983. **40**(7): p. 1595-1612.

110. Viovy, N., C. dataset, Editor. 2013: http://dods.extra.cea.fr/data/p529viov/cruncep/.

111. Oleson, K.W., et al., *Technical description of version 4.5 of the Community Land Model (CLM)*, in *Technical Note*. 2013, NCAR p. 434.

112. Li, F., X.D. Zeng, and S. Levis, *A process-based fire parameterization of intermediate complexity in a Dynamic Global Vegetation Model.* Biogeosciences, 2012. **9**(7): p. 2761-2780.

113. Prentice, S.A. and D. Mackerras, *The Ratio of Cloud to Cloud-Ground Lightning Flashes in Thunderstorms.* Journal of Applied Meteorology, 1977. **16**(5): p. 545-550.

114. Pechony, O. and D.T. Shindell, *Fire parameterization on a global scale.* Journal of Geophysical Research-Atmospheres, 2009. **114**.

115. Venevsky, S., et al., *Simulating fire regimes in human-dominated ecosystems: Iberian Peninsula case study.* Global Change Biology, 2002. **8**(10): p. 984-998.

116. Keyantash, J. and J.A. Dracup, *The quantification of drought: An evaluation of drought indices.* Bulletin of the American Meteorological Society, 2002. **83**(8): p. 1167-1180.

117. Giglio, L., I. Csiszar, and C.O. Justice, *Global distribution and seasonality of active fires as observed with the Terra and Aqua Moderate Resolution Imaging Spectroradiometer (MODIS) sensors.* Journal of Geophysical Research-Biogeosciences, 2006. **111**(G2).

118. Thonicke, K., et al., *The influence of vegetation, fire spread and fire behaviour on biomass burning and trace gas emissions: results from a process-based model.* Biogeosciences, 2010. **7**(6): p. 1991-2011.

119. Dormann, C.F., et al., *Collinearity: a review of methods to deal with it and a simulation study evaluating their performance.* Ecography, 2013. **36**(1): p. 27-46.

120. Zeng, T., et al., *Impacts of Prescribed Fires on Air Quality over the Southeastern United States in Spring Based on Modeling and Ground/Satellite Measurements.* Environmental Science & Technology, 2008. **42**(22): p. 8401-8406.

121. Magi, B.I., et al., *Separating agricultural and non-agricultural fire seasonality at regional scales.* Biogeosciences, 2012. **9**(8): p. 3003-3012.

122. Li, F., S. Levis, and D.S. Ward, *Quantifying the role of fire in the Earth system - Part 1: Improved global fire modeling in the Community Earth System Model (CESM1).* Biogeosciences, 2013. **10**(4): p. 2293-2314.

123. Pfeiffer, M., A. Spessa, and J.O. Kaplan, *A model for global biomass burning in preindustrial time: LPJ-LMfire (v1.0).* Geoscientific Model Development, 2013. **6**(3): p. 643-685.

124. Zhang, X.Y., et al., *Comparison of slope estimates from low resolution DEMs: Scaling issues and a fractal method for their solution.* Earth Surface Processes and Landforms, 1999. **24**(9): p. 763-779.

125. Amante, C. and B.W. Eakins, *ETOPO1 1 Arc-Minute Global Relief Model: Procedures, Data Sources and Analysis*. 2009, National Geophysical Data Center, NOAA.

126. Giglio, L., J.T. Randerson, and G.R. van der Werf, *Analysis of daily, monthly, and annual burned area using the fourth-generation global fire emissions database (GFED4).* Journal of Geophysical Research-Biogeosciences, 2013. **118**(1): p. 317-328.

127. Bradstock, R.A., A.M. Gill, and R.J. Williams, *Flammable Australia: fire regimes, biodiversity and ecosystems in a changing world*, ed. R.A. Bradstock, A.M. Gill, and R.J. Williams. 2012: CSIRO Publishing.

128. Li, F., B. Bond-Lamberty, and S. Levis, *Quantifying the role of fire in the Earth system - Part 2: Impact on the net carbon balance of global terrestrial ecosystems for the 20th century.* Biogeosciences, 2014. **11**(5): p. 1345-1360.

129. Akagi, S.K., et al., *Emission factors for open and domestic biomass burning for use in atmospheric models.* Atmospheric Chemistry and Physics, 2011. **11**(9): p. 4039-4072.

130. Jacobson, M.Z., *Effects of biomass burning on climate, accounting for heat and moisture fluxes, black and brown carbon, and cloud absorption effects.* Journal of Geophysical Research-Atmospheres, 2014. **119**(14): p. 8980-9002.

131. Brando, P.M., et al., *Fire-induced tree mortality in a neotropical forest: the roles of bark traits, tree size, wood density and fire behavior.* Global Change Biology, 2012. **18**(2): p. 630-641.

132. Cochrane, M.A., et al., *Positive feedbacks in the fire dynamic of closed canopy tropical forests.* Science, 1999. **284**(5421): p. 1832-1835.

133. Zimmermann, J., et al., *Grass mortality in semi-arid savanna: The role of fire, competition and self-shading.* Perspectives in Plant Ecology Evolution and Systematics, 2010. **12**(1): p. 1-8.

134. Balch, J.K., D.C. Nepstad, and L.M. Curran, *Pattern and process: Fire-initiated grass invasion at Amazon transitional forest edges*, in *Tropical Fire Ecology: Climate Change, Land Use, and Ecosystem Dynamics*. 2009, Springer Berlin Heidelberg: Berlin, Heidelberg. p. 481-502.

135. Bowman, D.M.J.S., et al., *A grass-fire cycle eliminates an obligate-seeding tree in a tropical savanna.* Ecology and Evolution, 2014. **4**(21): p. 4185-4194.

136. Vila, M., et al., *Positive fire-grass feedback in Mediterranean Basin woodlands.* Forest Ecology and Management, 2001. **147**(1): p. 3-14.

137. Epting, J. and D. Verbyla, *Landscape-level interactions of prefire vegetation, burn severity, and postfire vegetation over a 16-year period in interior Alaska.* Canadian Journal of Forest Research-Revue Canadienne De Recherche Forestiere, 2005. **35**(6): p. 1367-1377.

138. Medeiros, M. and H. Miranda, *Post-fire resprouting and mortality in cerrado woody plant species over a three-year period.* Edinburgh Journal of Botany, 2008. **65**(01): p. 53-68.

139. Richards, M.B. and B.B. Lamont, *Post-fire mortality and water relations of three congeneric shrub species under extreme water stress - A tradeoff with fecundity?* Oecologia, 1996. **107**(1): p. 53-60.

140. Barlow, J., et al., *Large tree mortality and the decline of forest biomass following Amazonian wildfires.* Ecology Letters, 2003. **6**(1): p. 6-8.

141. Wooster, M.J. and Y.H. Zhang, *Boreal forest fires burn less intensely in Russia than in North America.* Geophysical Research Letters, 2004. **31**(20).

142. Heward, H., et al., *Is burn severity related to fire intensity? Observations from landscape scale remote sensing.* International Journal of Wildland Fire, 2013. **22**(7): p. 910-918.

143. Jin, Y.F., et al., *The influence of burn severity on postfire vegetation recovery and albedo change during early succession in North American boreal forests.* Journal of Geophysical Research-Biogeosciences, 2012. **117**.

144. Rydgren, K., R.H. Okland, and G. Hestmark, *Disturbance severity and community resilience in a boreal forest.* Ecology, 2004. **85**(7): p. 1906-1915.

145. Chazdon, R.L., *Tropical forest recovery: legacies of human impact and natural disturbances.* Perspectives in Plant Ecology Evolution and Systematics, 2003. **6**(1-2): p. 51-71.

146. Finegan, B., *Pattern and process in neotropical secondary rain forests: The first 100 years of succession.* Trends in Ecology & Evolution, 1996. **11**(3): p. 119-124.

147. Guariguata, M.R. and R. Ostertag, *Neotropical secondary forest succession: changes in structural and functional characteristics.* Forest Ecology and Management, 2001. **148**(1-3): p. 185-206.

148. Beck, P.S.A. and S.J. Goetz, *Satellite observations of high northern latitude vegetation productivity changes between 1982 and 2008: ecological variability and regional differences.* Environmental Research Letters, 2011. **6**(4).

149. Goetz, S.J., G.J. Fiske, and A.G. Bunn, *Using satellite time-series data sets to analyze fire disturbance and forest recovery across Canada.* Remote Sensing of Environment, 2006. **101**(3): p. 352-365.

150. Ma, H.Y., et al., *Metrics and Diagnostics for Precipitation-Related Processes in Climate Model Short-Range Hindcasts.* Journal of Climate, 2013. **26**(5): p. 1516-1534.

151. Piani, C., et al., *Statistical bias correction of global simulated daily precipitation and temperature for the application of hydrological models.* Journal of Hydrology, 2010. **395**(3-4): p. 199-215.

152. Teutschbein, C. and J. Seibert, *Bias correction of regional climate model simulations for hydrological climate-change impact studies: Review and evaluation of different methods.* Journal of Hydrology, 2012. **456**: p. 12-29.

153. CIESIN, *Gridded population of the world version 3(GPWv3): Population density grids*. 2005, Socioeconomic Data and Applications Center (SEDAC): Columbia University, Palisades, New York, USA.

154. Hurtt, G.C., et al., *The underpinnings of land-use history: three centuries of global gridded land-use transitions, wood-harvest activity, and resulting secondary lands.* Global Change Biology, 2006. **12**(7): p. 1208-1229.

155. Luo, Y.Q., et al., *A framework for benchmarking land models.* Biogeosciences, 2012. **9**(10): p. 3857-3874.

156. Goulden, M.L., et al., *Patterns of NPP, GPP, respiration, and NEP during boreal forest succession.* Global Change Biology, 2011. **17**(2): p. 855-871.

157. Qian, T.T., et al., *Simulation of global land surface conditions from 1948 to 2004. Part I: Forcing data and evaluations.* Journal of Hydrometeorology, 2006. **7**(5): p. 953-975.

158. Giglio, L., et al., *Assessing variability and long-term trends in burned area by merging multiple satellite fire products.* Biogeosciences, 2010. **7**(3): p. 1171-1186.

159. Li, F. and D.M. Lawrence, *Role of Fire in the Global Land Water Budget during the Twentieth Century due to Changing Ecosystems.* Journal of Climate, 2017. **30**(6): p. 1893-1908.

160. Hicke, J.A., et al., *Postfire response of North American boreal forest net primary productivity analyzed with satellite observations.* Global Change Biology, 2003. **9**(8): p. 1145-1157.

161. Bond-Lamberty, B., C. Wang, and S.T. Gower, *Aboveground and belowground biomass and sapwood area allometric equations for six boreal tree species of northern Manitoba.* Canadian Journal of Forest Research-Revue Canadienne De Recherche Forestiere, 2002. **32**(8): p. 1441-1450.

162. Kloster, S., et al., *The impacts of climate, land use, and demography on fires during the 21st century simulated by CLM-CN.* Biogeosciences, 2012. **9**(1): p. 509-525.

163. Kloster, S., et al., *Fire dynamics during the 20th century simulated by the Community Land Model.* Biogeosciences, 2010. **7**(6): p. 1877-1902.

164. Yue, C., et al., *Modelling the role of fires in the terrestrial carbon balance by incorporating SPITFIRE into the global vegetation model ORCHIDEE - Part 2: Carbon emissions and the role of fires in the global carbon balance.* Geoscientific Model Development, 2015. **8**(5): p. 1321-1338.

165. Yue, C., et al., *How have past fire disturbances contributed to the current carbon balance of boreal ecosystems?* Biogeosciences, 2016. **13**(3): p. 675-690.

166. Bretherton, C.S. and S. Park, *A New Moist Turbulence Parameterization in the Community Atmosphere Model.* Journal of Climate, 2009. **22**(12): p. 3422-3448.

167. Park, S. and C.S. Bretherton, *The University of Washington Shallow Convection and Moist Turbulence Schemes and Their Impact on Climate Simulations with the Community Atmosphere Model.* Journal of Climate, 2009. **22**(12): p. 3449-3469.

168. Morrison, H. and A. Gettelman, *A new two-moment bulk stratiform cloud microphysics scheme in the community atmosphere model, version 3 (CAM3). Part I: Description and numerical tests.* Journal of Climate, 2008. **21**(15): p. 3642-3659.

169. Park, S., C.S. Bretherton, and P.J. Rasch, *Integrating Cloud Processes in the Community Atmosphere Model, Version 5.* Journal of Climate, 2014. **27**(18): p. 6821-6856.

170. Iacono, M.J., et al., *Radiative forcing by long-lived greenhouse gases: Calculations with the AER radiative transfer models.* Journal of Geophysical Research-Atmospheres, 2008. **113**(D13).

171. Mlawer, E.J., et al., *Radiative transfer for inhomogeneous atmospheres: RRTM, a validated correlated-k model for the longwave.* Journal of Geophysical Research-Atmospheres, 1997. **102**(D14): p. 16663-16682.

172. Liu, X., et al., *Toward a minimal representation of aerosols in climate models: description and evaluation in the Community Atmosphere Model CAM5.* Geosci. Model Dev., 2012. **5**(3): p. 709-739.

173. Bonan, G.B., et al., *Improving canopy processes in the Community Land Model version 4 (CLM4) using global flux fields empirically inferred from FLUXNET data.* Journal of Geophysical Research-Biogeosciences, 2011. **116**.

174. Sun, Y., L.H. Gu, and R.E. Dickinson, *A numerical issue in calculating the coupled carbon and water fluxes in a climate model.* Journal of Geophysical Research-Atmospheres, 2012. **117**.

175. Swenson, S.C., D.M. Lawrence, and H. Lee, *Improved simulation of the terrestrial hydrological cycle in permafrost regions by the Community Land Model.* Journal of Advances in Modeling Earth Systems, 2012. **4**.

176. Li, H.Y., et al., *Evaluating runoff simulations from the Community Land Model 4.0 using observations from flux towers and a mountainous watershed.* Journal of Geophysical Research-Atmospheres, 2011. **116**.

177. Swenson, S.C. and D.M. Lawrence, *A new fractional snow-covered area parameterization for the Community Land Model and its effect on the surface energy balance.* Journal of Geophysical Research-Atmospheres, 2012. **117**.

178. Subin, Z.M., W.J. Riley, and D. Mironov, *An improved lake model for climate simulations: Model structure, evaluation, and sensitivity analyses in CESM1.* Journal of Advances in Modeling Earth Systems, 2012. **4**.

179. Koven, C.D., et al., *The effect of vertically resolved soil biogeochemistry and alternate soil C and N models on C dynamics of CLM4.* Biogeosciences, 2013. **10**(11): p. 7109-7131.

180. Guenther, A.B., et al., *The Model of Emissions of Gases and Aerosols from Nature version 2.1 (MEGAN2.1): an extended and updated framework for modeling biogenic emissions.* Geoscientific Model Development, 2012. **5**(6): p. 1471-1492.

181. Riley, W.J., et al., *Barriers to predicting changes in global terrestrial methane fluxes: analyses using CLM4Me, a methane biogeochemistry model integrated in CESM.* Biogeosciences, 2011. **8**(7): p. 1925-1953.

182. Drewniak, B., et al., *Modeling agriculture in the Community Land Model.* Geoscientific Model Development, 2013. **6**(2): p. 495-515.

183. Sacks, W.J., et al., *Effects of global irrigation on the near-surface climate.* Climate Dynamics, 2009. **33**(2-3): p. 159-175.

184. Lamarque, J.F., et al., *Historical (1850-2000) gridded anthropogenic and biomass burning emissions of reactive gases and aerosols: methodology and application.* Atmospheric Chemistry and Physics, 2010. **10**(15): p. 7017-7039.

185. van der Werf, G.R., et al., *Interannual variability in global biomass burning emissions from 1997 to 2004.* Atmospheric Chemistry and Physics, 2006. **6**: p. 3423-3441.

186. Ghan, S.J., *Technical Note: Estimating aerosol effects on cloud radiative forcing.* Atmospheric Chemistry and Physics, 2013. **13**(19): p. 9971-9974.

187. Jiang, Y.Q., et al., *Impacts of global open-fire aerosols on direct radiative, cloud and surface-albedo effects simulated with CAM5.* Atmospheric Chemistry and Physics, 2016. **16**(22): p. 14805-14824.

188. Zhao, M. and S.W. Running, *Drought-induced reduction in global terrestrial net primary production from 2000 through 2009.* science, 2010. **329**(5994): p. 940-943.

189. Zhao, M., et al., *Improvements of the MODIS terrestrial gross and net primary production global data set.* Remote sensing of Environment, 2005. **95**(2): p. 164-176.

190. Prentice, I.C., et al., *Modeling fire and the terrestrial carbon balance.* Global Biogeochemical Cycles, 2011. **25**.

191. Piao, S.L., et al., *Evaluation of terrestrial carbon cycle models for their response to climate variability and to CO2 trends.* Global Change Biology, 2013. **19**(7): p. 2117-2132.

192. Randerson, J.T., et al., *Global Fire Emissions Database, Version 3.1*, O.R. ORNL DAAC, Editor. 2013: Tennessee, USA.

193. Dentener, F., et al., *Emissions of primary aerosol and precursor gases in the years 2000 and 1750 prescribed data-sets for AeroCom.* Atmospheric Chemistry and Physics, 2006. **6**: p. 4321-4344.

194. Ke, Z.M., et al., *The global fire plume-rise dataset and its climate model implementation*. 2017: J. Adv. Model Earth Sy.

195. Tosca, M.G., et al., *Dynamics of fire plumes and smoke clouds associated with peat and deforestation fires in Indonesia.* Journal of Geophysical Research: Atmospheres, 2011. **116**(D8): p. n/a-n/a.

196. Val Martin, M., et al., *Smoke injection heights from fires in North America: analysis of 5 years of satellite observations.* Atmos. Chem. Phys., 2010. **10**(4): p. 1491-1510.

197. Ciais, P., et al., *Carbon and Other Biogeochemical Cycles in Climate Change 2013: The Physical Science Basis*, in *Contribution of Working Group I to the Fifth Assessment Report of the Intergovernmental Panel on Climate Change*, T.F. Stocker, D. Qin, G.-K. Plattner, M. Tignor, S.K. Allen, J. Boschung, A. Nauels, Y. Xia, V. Bex and P.M. Midgley, Editor. 2013: Cambridge, United Kingdom and New York, NY, USA.

198. Screen, J.A., *Simulated Atmospheric Response to Regional and Pan-Arctic Sea Ice Loss.* Journal of Climate, 2017. **30**(11): p. 3945-3962.

199. Macias-Fauria, M., et al., *Eurasian Arctic greening reveals teleconnections and the potential for structurally novel ecosystems.* Nature Climate Change, 2012. **2**(8): p. 613-618.

200. Goetz, S.J., et al., *Satellite-observed photosynthetic trends across boreal North America associated with climate and fire disturbance.* Proceedings of the National Academy of Sciences of the United States of America, 2005. **102**(38): p. 13521-13525.

201. Elmendorf, S.C., et al., *Plot-scale evidence of tundra vegetation change and links to recent summer warming.* Nature Climate Change, 2012. **2**(6): p. 453-457.

202. van Leeuwen, T.T., et al., *Biomass burning fuel consumption rates: a field measurement database.* Biogeosciences, 2014. **11**(24): p. 7305-7329.

203. Fisher, R.A., et al., *Taking off the training wheels: the properties of a dynamic vegetation model without climate envelopes, CLM4.5(ED).* Geoscientific Model Development, 2015. **8**(11): p. 3593-3619.